Mathematical modelling of overwash on low freeboard bodies by water waves

David M. Skene

February 22, 2018

Thesis submitted for the degree of

Doctor of Philosophy

in

Applied Mathematics

at The University of Adelaide

Faculty of Engineering, Computer and Mathematical Sciences

School of Mathematical Sciences

THE UNIVERSITY
of ADELAIDE

Contents

List of Figures

Signed Statement

I certify that this work contains no material which has been accepted for the award of any other degree or diploma in my name, in any university or other tertiary institution and, to the best of my knowledge and belief, contains no material previously published or written by another person, except where due reference has been made in the text. In addition, I certify that no part of this work will, in the future, be used in a submission in my name, for any other degree or diploma in any university or other tertiary institution without the prior approval of the University of Adelaide and where applicable, any partner institution responsible for the joint-award of this degree.

I acknowledge that copyright of published works contained within this thesis resides with the copyright holder(s) of those works.

I also give permission for the digital version of my thesis to be made available on the web, via the Universitys digital research repository, the Library Search and also through web search engines, unless permission has been granted by the University to restrict access for a period of time.

I acknowledge the support I have received for my research through the provision of an Australian Government Research Training Program Scholarship.

Signed: . ..... Date: 22/2/2018 .....

Disclaimer

Chapter two contains excerpts and figures that have been published in the journal article:

Skene, D. M., Bennetts, L. G., Meylan, M. H. & Toffoli, A. 2015 Modelling water wave overwash of a thin floating plate. *J. Fluid Mech.* **777**, R3.

Chapter three contains excerpts and figures that have been published in the journal article:

Skene, D. M., Bennetts, L. G., Wright, M., Meylan, M. H. & Maki, K. J. 2018 Water wave overwash of a step. *J. Fluid Mech.* **839**, 293-312.

Chapter five recounts some work contained in

Nelli, F., Bennetts, L. G., Skene, D. M., Monty, J. P., Lee, J. H., Meylan M. H. & Toffoli, A. 2017 Reflection and transmission of regular water waves by a thin, floating plate. *Wave Motion* **70**, 209-221.

If referencing the work contained in these chapters please include an additional reference to these journal articles.

Acknowledgements

I would like to acknowledge my principle supervisor Dr Luke Bennetts and my co-supervisor Assoc. Prof. Mike Meylan. Dr Luke Bennetts has been a better supervisor than I could have dreamed for. I am sincerely grateful for the time and effort he has put into guiding me throughout this research. He has always been an ample role model and gone above and beyond what could be expected of a supervisor. I must also thank Assoc. Prof. Mike Meylan who, when called upon, has provided invaluable wisdom and insight.

I would like to acknowledge the experimental team of Assoc. Prof. Alessandro Toffoli, Dr Alberto Alberello, Dr Peter Arber, and Mr Claudio Cavaliere, who conducted experiments at the University of Plymouth's Coastal Ocean and Sediment Transport laboratory. I would also like to acknowledge the experimental team of Assoc. Prof. Alessandro Toffoli, Dr Alberto Alberello, and Mr Filippo Nelli, who conducted further experiments at the University of Melbourne's wave-tank facility. Further, I would like to acknowledge the excellent work of Prof. Kevin Maki and Mr Michael Wright who developed the CFD model of an overwashed step.

I must also acknowledge the Australian Federal Government for providing a PhD scholarship under the Australian Postgraduate Award fund, as well as the Australian Antarctic Science Program, who provided a top-up scholarship (Project 4123).

Finally, I would like to thank my family, particularly my parents Phil and Sally, my brother Peter, and my late grandparents Ann and Bill. Their support throughout these past few years of research, and with my education more broadly, has been invaluable.

Dedication

This thesis is dedicated to my family. I shall forever be grateful for your love and support.

Abstract

In this thesis a simplified mathematical model for the overwash of low freeboard bodies is developed. Overwash is the process where surface-gravity water waves wash water over the surface of an otherwise unsubmerged body. The investigation is motivated by wave-tank experiments on the interaction between waves and floating elastic plates — the canonical model for the interaction between waves and sea ice. These experiments have found that when overwash occurs it dissipates energy and perturbs the surrounding water waves. This is not accounted for in existing models of waves interacting with floating elastic plates because they do not include the overwash process.

The objective of this investigation is to develop a theoretical model of overwash that can predict the water on the body and surrounding waves accurately. Two overwash problems are considered: Overwash of a thin floating elastic plate, and overwash of a step (a vertical wall with flat upper surface). Both of these problems are modelled using two spatial dimensions (one length and one depth), and the overwash is created by monochromatic water waves. The overwashed floating plate problem is investigated because of its relevance to these experiments and the interaction of waves and sea ice. The overwashed step problem is investigated because its relative simplicity allows for a more direct investigation into the overwash phenomenon. In each problem the mathematical model uses the nonlinear shallow-water equations to model the overwashed water and linear potential flow theory to model the motion of the surrounding waves. The models force the overwash by assuming it has a negligible impact on the surrounding waves, and then correct the surrounding waves using an energy conservation method.

The model for the floating elastic plate is compared to experiments and good agreement is found in terms of the prediction of the overwash and surrounding waves. Similarly, the model for the step is compared to a computational fluid dynamics model and good agreement is found in terms of the prediction of the overwash and surrounding waves.

Chapter 1

Introduction

1.1 Background: Ocean waves and sea ice

The sub-zero temperatures around the Arctic and Antarctic poles freeze the upper surface of their oceans. This freeze results in the formation of thin and long sheets of sea ice, otherwise known as floes. Ocean waves can propagate tens to hundreds of kilometres into these ice covered seas in regions known as marginal ice zones (MIZs) (Wadhams, 1986; Kohout *et al.*, 2014). These zones are characterised by the complicated interaction between the waves and sea ice.

As the waves interact with the floes they significantly alter the ice cover. They push and pull the floes together resulting in more closely packed floes, and an overall reduction in the sea ice extent (Squire *et al.*, 1995). This pushing and pulling can also lead to collisions between floes, which can fracture the floes or fuse their edges together (McKenna & Crocker, 1991). The oscillatory motion of the waves flex and bend the ice, which can result in strains that fracture floes into smaller pieces (Langhorne *et al.*, 1998, 2001). The break-up of sea ice is particularly pronounced for storm-like waves (Kohout *et al.*, 2014), which are becoming increasingly frequent due to climate change (Young *et al.*, 2011). These smaller floes are more exposed to the surrounding winds, currents, and waves, which accelerates the seasonal melt (Massom & Stammerjohn, 2010). In addition, the waves perturb the surface water as it is freezes, altering the size, shape, and material properties of newly forming floes (Wadhams *et al.*, 1987; Lange *et al.*, 1989). If the waves

are of large amplitude, it can also result in water washing onto the floes, which further accelerates the melt (Massom & Stammerjohn, 2010).

As waves propagate into the MIZ their height and energy decays exponentially in a process known as wave attenuation (Wadhams, 1973*a*, 1986; Squire *et al.*, 1995). The wave attenuation created by the floes protects the ice farther into the polar oceans from wave endued fracturing. Hence, at the boundary between open and ice covered ocean, floes generally have lengths in the order of metres and floes deeper into the MIZ can have lengths up to kilometres long (Squire & Moore, 1980). Eventually, the floes cause the waves to die-out, allowing for the formation of thick, long, and continuous bulks of pack ice deeper into the ice covered oceans.

There is an increased demand for accurate seasonal and long-term sea ice forecasting models with global temperatures rising (Graham, 1995; Hansen *et al.*, 2010), Arctic ice coverage decreasing (Parkinson & DiGirolamo, 2016), a greater interest in polar maritime activities (Hall & Wouters, 1994; Tin *et al.*, 2013), and contemporary demands for climate modelling (Massom & Stammerjohn, 2010). The coupled interaction between waves and sea ice in the MIZ is yet to be incorporated into operational wave-sea ice forecasting models (Williams *et al.*, 2013*a*), although efforts are being undertaken (e.g. Dumont *et al.*, 2011; Doble & Bidlot, 2013; Williams *et al.*, 2013*a*,*b*). This can be attributed to a lack of in-field Antarctic/Arctic data and the complexity of the wave-sea ice interaction. It can also be attributed to the lack of understanding of some of the underlying wave attenuation mechanisms in the MIZ.

The pioneering in-situ Arctic experiments of Wadhams (1973*b*); Squire & Moore (1980); Wadhams *et al.* (1986, 1988), and others, established that attenuation is greatest for short length waves — implying that shorter waves decay more rapidly through the MIZ than their longer counterparts. This results in a gradual decline in the wave height, and skews the MIZ waves towards longer wavelengths. Since this pioneering work in the 1970/80s there has been a lack of dedicated Antarctic/Arctic MIZ wave measurements until the more modern experimental campaign outlined in Kohout *et al.* (2014) and Meylan *et al.* (2014). In Meylan *et al.* (2014) the waves propagating up to 130 km into the the Antarctic MIZ were measured and analysed across the frequency spectrum. Consistent with earlier observations, it was found that for long period waves, or low am-

plitude short period waves, the attenuation rate is independent of wave amplitude, and proportional to the reciprocal of the wave period squared. However, it was also found that for short period waves above some critical amplitude the attenuation rate would rapidly increase.

Multiple mechanisms contribute to wave attenuation in the MIZ (Squire, 2007). They are dependent on the ice cover, wave types, and the location within the MIZ. The predominant mechanism is the scattering of waves about the floes. Theoretical descriptions of this mechanisms typically model the floes as floating elastic plates, and the waves using linear potential water wave theory (summarised in the the reviews of Squire *et al.*, 1995; Squire, 2007). These models will be discussed in greater detail in section 1.3. The key attribute of these models is that they assume the motion of the plate and surrounding waves is linear with respect to incident wave amplitude, i.e. they are linear models. They predict that only a portion of the incident wave is transmitted beyond a floe because the floes constrain the vertical motion of the water beneath.

An interesting facet of these linear scattering models will be demonstrated in chapter 2 of this thesis. It shows that if the waves around the plate/floe are sufficiently steep (but still relatively mild compared to rough sea conditions), linear theory predicts that the free surface of the surrounding water can exceed the height of the upper surface of the plate/floe. This results in overwash — the process where water waves wash water over the surface of an otherwise unsubmerged body. Overwash is particularly likely to occur with floes because they have low freeboards given their density is similar to that of the surrounding ocean water (Timco & Weeks, 2010). Although these linear models can predict that overwash occurs, there has been no research on how linear models need to be adapted in order to incorporate overwash effects (prior to this thesis and related papers Skene *et al.*, 2015, 2018).

Linear based scattering appears to be the prevailing description of wave attenuation in the MIZ. However, other, less well understood, attenuation mechanisms are known to exist that are nonlinear with respect to wave amplitude. Consideration of these nonlinear mechanisms is necessary to model the amplitude dependence of wave attenuation found in the observations of Meylan *et al.* (2014). One such mechanism is the inelastic collision between floes (McKenna & Crocker, 1991), which occurs when the floes are closely spaced.

A further, often cited nonlinear attenuation mechanism, is viscous losses, which occur as waves break or in the boundary layer around the floes' surfaces (Shen & Squire, 1998). Another nonlinear attenuation mechanism, which has been illuminated by relatively recent wave-tank experiments, is overwash.

1.2 Model ice floe wave-tank experiments

To the author's best knowledge, the first major effort to validate linear wave-sea ice models (i.e. the aforementioned linear scattering models) in a laboratory setting was conducted by Montiel *et al.* (2013*a*,*b*). In these experiments one or two floating elastic disks were subjected to monochromatic water waves in a laboratory wave-tank, and the displacement of the plate's upper surface was measured. Although the investigation was directly related to sea ice, the disks in the experiments were made of polyvinyl chloride (PVC) because of the inherent technical difficulties in using sea ice in a laboratory wave-tank. The use of a floating non-sea ice plate is an ongoing theme in wave-tank experiments due to this technical difficulty. The disks themselves were constrained to bring them more in-line with the assumptions of linear models. This meant that vertical barriers were placed along the circumference of the disks to prevent overwash. It also meant that they were constrained such that they could move up and down freely, but were prevented from drifting along the basin. They were subjected to regular incident waves of steepnesses (wave amplitude multiplied by wavenumber) of 0.03 and 0.06, and wavelength to disk diameter ratios ranging from 0.63 to 3.14. It was found that, when these idealised constraints were imposed on the plates, the motions were similar to that described in linear models.

A second round of wave-tank experiments was conducted by Bennetts *et al.* (2015) and Meylan *et al.* (2015). Both studies used the same set of experiments. In Meylan *et al.* (2015) the vertical displacement of a floating elastic plate was investigated as it bent, heaved, and pitched in response to the waves. In Bennetts *et al.* (2015) the waves transmitted past the plate were investigating using depth probes upstream and downstream from the plate. Test were conducted where solitary 1 m by 1 m square PVC or polypropylene (PP) plates were subjected to regular monochromatic incident waves in a wave-tank that was 10 m wide and 15.5 m long. The incident waves had wavelengths 0.56-1.51 m and

steepnesses ranging from 0.04 to 0.15. Unlike in Montiel *et al.* (2013*a*,*b*), barriers were not installed around the edges of the plate, which allowed overwash to occur. Further, the plates were only loosely tethered to the basin, which allowed the plates to surge back and forth, but prevented them from drifting down the wave-tank. It was found that even if overwash occurred linear models predict the motion of the plate well (Meylan *et al.*, 2015). It was also found that the transmission was linear with respect to the incident wave amplitude for low steepness incident waves only (Bennetts *et al.*, 2015). For higher steepness incident waves it was found that (i) the transmission coefficient (the ratio of the transmitted wave amplitude to incident wave amplitude) would decrease, and (ii) that the transmitted waves would be more broadly distributed across the frequency spectrum (i.e. the transmitted waves would become more irregular). Neither of these results are predicted by linear scattering models, which predict that the transmission coefficient and wave regularity are independent of incident wave steepness. It was also found that for higher steepness incident waves overwash would occur, and that the overwashed water would become deeper and more energetic as the incident wave steepness increased. Bennetts *et al.* (2015) attributed the decrease in transmission coefficient to energy losses associated with overwash. They also attributed the increased irregularity of the transmitted waves to the nonlinear interaction between overwash and the surrounding water.

Nelli *et al.* (2017) extended the investigation of Bennetts *et al.* (2015). The experiments of Nelli *et al.* (2017) used solitary 1 m long and 1.9 m wide PVC and PP plates subjected to monochromatic waves similar to those in Bennetts *et al.* (2015). The basin itself was 2 m wide, and therefore the experiments were effectively two dimensional (one length and one depth). Experiments were conducted using loosely tethered PP and PVC plates with and without edge barriers. As in Montiel *et al.* (2013*b*,*a*), the edge barriers were constructed such that they prevented overwash from occurring, but without affecting the material properties of the plate. It was found that, for plates with and without edge barriers, the wave field upstream from the plate would remain regular, and that the reflection coefficient (the ratio between reflected wave amplitude and incident wave amplitude) would remain constant. It was therefore found that linear scattering theory could accurately predict the waves reflected by the plate when overwash was, and was not, allowed to occur. For the plates with edge barriers, it was found that the transmis-

sion coefficient remained relatively independent of incident wave steepness, and that the transmitted waves remained regular. However, for the plates without edge barriers, the transmission coefficient would decrease with incident wave steepness, and the transmitted waves would become increasingly irregular. The decrease in transmission coefficient was greatest for steeper waves, which corresponded to deeper and more energetic overwash. Energy losses were measured by comparing the energy of the transmitted and reflected waves to the energy of the incident wave. For plates with edge barriers energy would be conserved. However, for plates without edge barriers, energy was dissipated when overwash occurred, and this dissipation was greatest for the deepest and most energetic overwash. It was therefore concluded that if overwash occurred it would dissipate energy and produce the nonlinearity in the transmission coefficient.

The occurrence and prevalence of overwash is not just limited to investigations on the wave response of a solitary floating elastic plate. Bennetts & Williams (2015) investigated the waves transmitted past an array of circular wooden floating disks in an effort to validate the linear, multiple floe, scattering models of Meylan *et al.* (1997), Bennetts & Squire (2012), and others. Such models are the basis for the theory on how waves are scattered by a conglomerate of floes in the MIZ. It was found that linear scattering models predicted the wave transmission well for low steepness incident waves and low concentrations of disks. However, as incident wave steepness increased, the wave transmission was overpredicted by linear models. This wave regime was found to produce overwash on the disks and increased collisions between disks. Hence, the reduction in wave transmission was attributed to energy dissipation associated with overwash and the collisions between disks.

Yiew *et al.* (2016) compared the hydrodynamic responses of 200 mm diameter circular plastic disks subjected to monochromatic water waves of lengths 2 to 25 multiples of the disk's length, and amplitudes ranging from 2.5 to 50 mm. These experiments were conducted to validate models of how waves cause floes to surge and drift. Tests were conducted with and without edge barriers. They found that the response amplitude operator of the surge, heave, and pitch of the disk without edge barriers was less than expected when overwash occurred. Similarly, McGovern & Bai (2014) noted overwash of paraffin wax plates subjected to monochromatic water waves during laboratory experiments, which

were also conducted in order to verify the wave induced motion of sea ice floes. They also attributed smaller than expected drift velocities to the overwash. The experiments of McGovern & Bai (2014) have since been compared to an OpenFOAM computational fluid dynamics (CFD) model of the same interaction in Bai *et al.* (2017). As in the experiments, they found that for 200 mm square rectangular plates with thickness 20 mm, overwash would occur for incident wave steepnesses greater than 0.044 and wavelengths less than four times the diameter of the disks. They also found that the CFD model, which included the overwash, gave better predictions for the surge and heave of the plates when compared to linear models without overwash.

1.3 Linear models of waves and sea ice

The previously mentioned linear based models of the waves-sea ice interaction have been in development for a number of decades (see e.g. the reviews of Squire *et al.*, 1995; Squire, 2007). Research of this nature tends to be based on in-field Arctic observations, which were outlined in Wadhams (1973*a*). In these theoretical models the floes are modelled as floating elastic plates, and the surrounding water waves are modelled using linear potential flow theory. They assume that the water is irrotational, incompressible, and inviscid. They also assume that the waves are of low steepness such that in the domain around the plate the classic linearised (with respect to wave amplitude) free surface condition is employed. In addition, they assume that the plates deflections are sufficiently small such that its deflections are elastic. Hence, the motion of the floes are modelled using elastic beam/plate theory (e.g. Euler-Bernoulli, Timoshenko, Kirchhoff-Love). Solutions to these models are obtained by coupling the the water's linearised free surface pressure and velocity conditions to the pressure and velocity at the plate's lower surface. As was mentioned in section 1.1, these models to not account for overwash, even if they predict the surrounding waves exceed the plate's freeboard.

The linear formulation of these wave-floe interaction models leads to two very useful results in the context of developing mathematical solutions. Firstly, as the water's free surface condition around and beneath the plate is linearised, it allows the solution to be developed non-dimensionally with respect to the amplitude of the surrounding waves.

That is, the solution for the wave and plate motion is directly proportional to the incident wave amplitude. Secondly, it allows the solution to be decomposed into individual spectral frequencies. This allows the wave response at a given frequency to be calculated independent of the wave response at a different frequencies.

The first complete solution to this model in two-dimensions (one length and one depth) for a solitary floe was given in Meylan & Squire (1994), and for a continuous ice sheet in Fox & Squire (1994). In Meylan & Squire (1994) the solitary flow was assumed to have negligible draft and drift, and a solution was developed using a Green's function technique. In Fox & Squire (1994) the solution was obtained by using a technique known as 'eigenfunction matching', which matches the velocity potential of the water beneath the plate to the velocity potential of surrounding water. The eigenfunction matching method, in particular, has laid the foundations for more sophisticated models of wave-floe dynamics such as fully three dimensional plates, surging plates, complicated plate geometries, plate drafts, varying ocean bed topographies, etc. (as referenced in the review of Squire, 2007). The International Water Wave and Floating Body community (`www.iwwwfb.org`), in particular, has produced a wealth of literature on solution techniques and their results relevant to sea ice in, for example, Evans & Porter (2003); Meylan (2003); Evans (2004); Chung & Fox (2005); Williams (2006), and many others.

The general property of these models is that because the plate modifies the dispersion relation of the water beneath it (the relationship between wavelength and frequency), the plate transmits only a portion of the incident wave, and reflects the incident wave's remaining energy. Hence, under this formulation, energy is conserved, and the apparent attenuation of the waves occurs because only a portion of the incident energy wave is transmitted beyond the plate. They also find that shorter waves are attenuated much more than longer waves. Thus, the solution is similar to observations of the MIZ: That the floes attenuate the waves, and that shorter waves attenuate more rapidly. However, because these models are linear, they are unable to account for the reduced transmission coefficient when overwash occurs in the associated wave-tank experiments.

The solution for the wave response of a floating elastic plate has also allowed for the development of theoretical models of waves transmitted/reflected by a network of floating elastic plates in two dimensions (or scattered by a network of plates when the problem

is considered in three dimensions). Examples of these kinds of models can be found in Kohout & Meylan (2006); Bennetts & Squire (2009); Bennetts *et al.* (2010); Montiel *et al.* (2016), and others. Such descriptions typically take the scattering effects of a solitary floe and amalgamate it with other nearby floes. Therefore, broadly speaking, they model the attenuation in the MIZ via the superposition of the linear wave response of individual floes. Although each of these developments have unique results in their own right, they appear to give similar wave attenuation properties to those found in most MIZ observations. That is, they predict that the amplitude of waves decreases exponentially as they propagate through the MIZ, and that the attenuation is greatest for smaller wavelengths. These models, however, are underpinned by the assumption of linearity with respect to incident wave amplitude used in the solitary plate model. Hence, they cannot reproduce the results found by the in-field measurements of Meylan *et al.* (2014), where attenuation is dependent on wave amplitude for high amplitude short length waves above some critical wave height — the same kind of wave regime in which overwash occurs in wave-tank experiments.

1.4 Phenomena related to overwash: Submerged shelves and green water

Although overwash research is relatively recent in the context of wave-sea ice interactions, a larger literature exists on modelling the cognate phenomena of water washing over submerged shelves and of green water washing onto ships. The water washing over submerged shelves phenomenon is where waves wash over submerged bodies wherein the water rapidly transitions from deep to shallower flow (see e.g. Grue, 1992; Losada *et al.*, 1997; Orszaghova *et al.*, 2012). It is typically investigated in order to understand how waves wash over reefs, breakwaters, sandbanks, sunken rocks, underwater ridges, or other submerged marine structures. Theoretical models and experiments find that the transition from deep to more shallow flow results in strong nonlinear deformations of the surrounding waves, particularly if wave breaking occurs (Orszaghova *et al.*, 2012). This results in a net loss of energy and a transferral of energy into higher frequency waves (Grue, 1992).

Although similar to overwash, particularly in terms of how the transition to shallow flow perturbs the surrounding waves, the key difference between the two phenomena is that, for overwash, the upper surface of the body is wholly unsubmerged if not for the the presence of the surrounding waves. This is also why the theoretical models for the submerged shelf cannot readily be extended to overwash. To create a coupling condition between the flow into/out of the region above the submerged shelf and the surrounding deeper water, models such as those in Grue (1992) exploit the fact that the shelf's submergence is much larger than the amplitude of the incoming waves. This coupling condition is not readily applicable to overwash as the body is unsubmerged if not for the incoming waves.

Green water is the phenomenon where isolated extreme waves force water onto the surface of floating bodies with large freeboards, typically in the context of predicting dangerous hydrodynamic loads imposed on ship decks in severe wave conditions. Mizoguchi (1988) pioneered green water modelling, using laboratory experiments on scaled ship decks, and a two-dimensional numerical model. The numerical model used the nonlinear shallow-water equations to model the green water, and experimentally determined water depths around the ship deck as boundary conditions. Mizoguchi (1988) found the model predicts qualitatively, although not necessarily quantitatively, similar water depths along the deck to those founds in his experiments.

Buchner (2002)'s PhD thesis, and related series of conference papers Buchner (1995, 1996); Buchner & Cozijn (1997), as well as Greco *et al.* (2005, 2007), also used laboratory experiments to study green water forced by short duration wave packets, with peak amplitudes exceeding the freeboard by $> 0.1\,\mathrm{m}$ and incident wave height to freeboard ratios > 2. Buchner (2002) used a freely floating model ship (floating production storage and offloading, FPSO), including complex bow geometries, that was subjected to both regular and irregular waves. Greco *et al.* (2005, 2007) used a fixed, flat, model ship deck subjected to a small wave train of ~ 4 wave peaks generated by a flap-type wave maker (described in detail in the PhD thesis by Greco, 2001). In both sets of experiments, green water was found to be, in most cases, generated by plunging wave breaking motion over the edge of the deck, resulting in overturning, air entrainment, and three-dimensional turbulent effects. This green water would then develop into a shallow-water flow farther along the deck, with depths generally $> 100\,\mathrm{mm}$. Note that the Reynolds numbers in

the experiments can be inferred to be $> 10^4$ using the values of the water velocity and depth at the deck's edge. Similar turbulent breaking effects to those near the deck's edge were found as the green water collided with objects on the model ship deck. From these observations, Buchner (2002) and Greco *et al.* (2005, 2007) deduced that a shallow-water model, of the form proposed by Mizoguchi (1988), was not sufficient to model green water at the edge of the deck, or as it collided with on-deck structures.

Buchner (2002) discussed the applicability of a range of potential green water models, and adopted a two-dimensional CFD modelling approach forced by an experimentally determined constant initial water height at the deck edge. His model was based on the single-phase (water) incompressible Navier Stokes equations, thus capturing wave overturning at deck edge and shallow-water flow farther along the deck. His model was solved with the volume of fluid method and without a turbulence closure (i.e. the model assumed laminar conditions) or surface tension. Model predictions were shown to agree reasonably well with the experimental measurements in terms of free surface profiles and depth signals measured along the deck; including the locations close to the deck edge, where the free surface experienced the most pronounced overturning. Greco *et al.* (2007) developed a two-dimensional CFD model of the green water and surrounding basin based on a domain decomposition strategy. In this model fully nonlinear potential-flow theory was used to model the majority of the flow, and the incompressible Navier Stokes equations were used close to the deck edge during overturning events. Green water forcing wave packets were generated by a virtual wave maker. The model was shown to provide better agreement with measured free surface profiles at the deck edge and in the shallow-water flow along the deck than the model used by Buchner (2002). The better agreement was presumably due, at least in part, to the modelling of the surrounding waves and because the model ship deck was held stationary.

Subsequent green water studies have predominantly employed CFD modelling techniques, particularly the use of incompressible laminar Navier Stokes equations (as in Buchner, 2002). Nielsen & Mayer (2004) modelled the basin and green water (similar to Greco *et al.*, 2007) using the single-phase incompressible Navier Stokes equations. It was solved using the volume of fluid method (similar to Buchner, 2002), but with a significantly more refined mesh than Buchner (2002). They compared model predictions with experimen-

tal data presented by Buchner (2002) and Greco *et al.* (2005, 2007). They found strong agreement (comparable to Greco *et al.*, 2007) in terms of the free surface profile as waves overturn onto the deck, and in terms of the depth signals along the deck at times when air entrainment and turbulence were observed in the experiments.

Overwash shares a number of similarities with the green water phenomena, particularly because the waves abruptly wash onto an otherwise unsubmerged surface. However, overwash distinguishes itself from green water by (i) occurring for moderate incident wave amplitudes, (ii) being semi-continuously forced, as opposed to the 'single event' rouge wave nature of green water, (iii) being for objects with significantly lower freeboards, and (iv) the prime interested of overwash interactions is wave attenuation, rather than hydrodynamic loads.

1.5 Scope of thesis

In this thesis a simplified mathematical model of overwash of low freeboard bodies by monochromatic water waves is developed. It is the first effort, of any kind, to develop a theoretical model of overwash in the context of waves and sea ice or beyond. Two overwash problems are considered: Overwash of a floating elastic plate, and overwash of a step (a vertical wall with an upper surface that is collinear with the surrounding water's equilibrium free surface level). The former problem is investigated because of its relationship to wave-tank experiments of waves and sea ice. The latter problem is investigated because its relative simplicity allows for a more direct investigation of overwash. The models are developed as an extension of existing linear water wave/plate motion theory. They are developed along these lines, rather than using a CFD modelling approach commonplace with green water research, in order to be more readily deployable in the related work of wave attenuation by sea ice. The models use the nonlinear shallow-water equations to model the overwash and linear potential flow theory to model the surrounding water wave and floating body motion. In both instances the problem is considered in two dimensions (one length and one depth).

In the first phase of the investigation (chapters 2 and 3) is dedicated to predicting the overwash. The overwash is forced by assuming the perturbations it makes to the surroun-

ding wave are negligibly small when compared to the same problem without overwash. For the floating plate problem, the overwash predictions are analysed and validated using data obtained from the experiments of Meylan *et al.* (2015) and Bennetts *et al.* (2015). For the step problem, the overwash predictions are analysed and validated using a newly developed bespoke CFD model that is based on cognate green water CFD models.

The second phase of the investigation (chapters 4 and 5) is dedicated to predicting the wave transmission/reflection by the overwashed body. A prediction-correction technique is developed where the overwash is predicted via the models in the first phase of investigation, and then the surrounding waves are corrected using energy conservation principles. The wave transmission/reflection model is analysed and validated using the CFD model for the step problem and using the experiments of Nelli *et al.* (2017) for the floating elastic plate problem.

Chapter 2

Overwash of a Floating Elastic Plate

2.1 Introduction

Experiments of a floating elastic plate subjected to monochromatic water waves were conducted in the wave basin facility of the Coastal Ocean and Sediment Transport (COAST) Laboratory, Plymouth University, U.K. The experiments were conducted to measure wave scattering, plate deflection, and overwash of a floating elastic plate. The analysis for wave scattering has been presented in Bennetts *et al.* (2015), and the analysis of the plate motion presented in Meylan *et al.* (2015). In this chapter the overwash recordings are analysed.

A two dimensional simplified mathematical model for predicting the overwashed water is developed in conjunction. The model uses linear potential theory to model the motion of the plate and surrounding water, and the overwash is modelled using the nonlinear shallow-water equations. The key modelling assumption is that the overwash can be forced without considering its influence on the motion of the plate and surrounding waves.

The objectives of this chapter are to:

1. Describe the properties of the overwashed water in the wave-tank experiments.

2. Develop a simplified two dimensional mathematical model that can predict the overwash.

3. Compare the mathematical model to the experiments in order to access its validity.

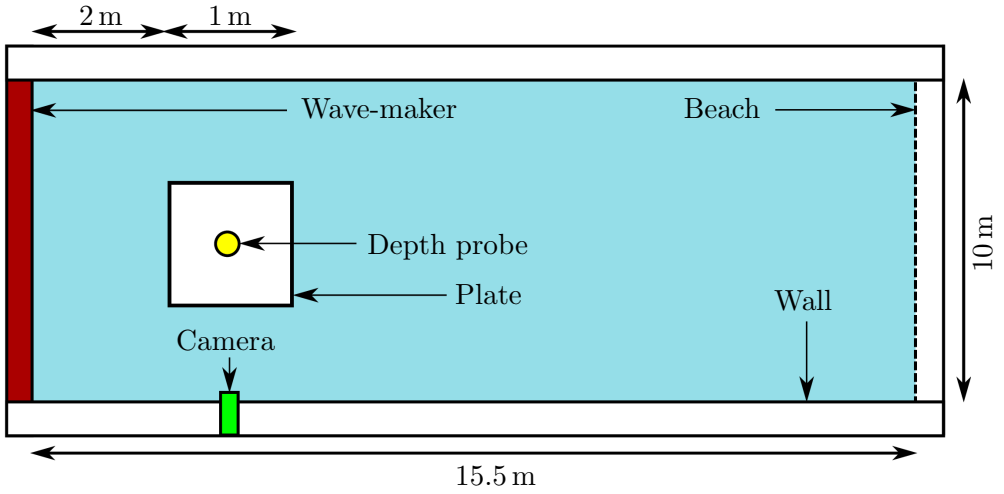

Figure 2.1: Plan view of Plymouth experimental set-up (not to scale).

2.2 Plymouth floating plate experiments

2.2.1 Experimental set-up

The experimental basin was 10 m wide and 15.5 m long. It was filled with fresh water of a density $\rho_w \approx 1000\,\mathrm{kg\,m^{-3}}$ to a depth of $H = 0.5\,\mathrm{m}$. At the left-hand end of the basin a piston controlled wave-maker was used to generate incident waves and absorb a proportion of the waves reflected back to it. A beach at the right-hand end of the basin was used to absorb the majority of the wave energy that reached it. A reflection analysis, without the floating plate inside the tank, found that for the prescribed waves reflection effects contributed less than 1% of the overall wave energy. Figure 2.1 shows a schematic of the basin.

For each test a solitary thin floating plastic plate was deployed 2 m downstream from the wave-maker. The plates were square with a side length, $2L = 1\,\mathrm{m}$. The plates were aligned such that their upstream and downstream edges were parallel to the wave-maker. Their corners were loosely tethered to the basin floor to prevent drift down the tank. The tether was tested and found to have a natural period greater than 20 s, which is over an order of magnitude greater than the period of the incident waves used. It therefore allowed the plates to bend and surge back and forth naturally, but restricted drift down the basin.

Polypropylene (PP) and polyvinyl chloride (PVC) plastic plates were tested. The PP had a manufacturer specified density of $\rho_p = 905\,\mathrm{kg\,m^{-3}}$, Young's modulus $E_p = 1600\,\mathrm{MPa}$, and an approximate Poisson's ratio of $\nu = 0.4$. The PVC had a density of $\rho_p = 500\,\mathrm{kg\,m^{-3}}$, Young's modulus $E_p = 500\,\mathrm{MPa}$, and an approximate Poisson's ratio of $\nu = 0.4$. Multiple thicknesses were tested for each plate material. The thicknesses were $d = 5\,\mathrm{mm}$, $10\,\mathrm{mm}$, $19\,\mathrm{mm}$ (PVC only), $20\,\mathrm{mm}$ (PP only), and $40\,\mathrm{mm}$ (PP only). In a review of the mechanical properties of sea ice, Timco & Weeks (2010) reported the typical density of sea ice to ranges from ~ 720 to $940\,\mathrm{kg\,m^{-3}}$. They also reported the Young's modulus of sea ice to range from $\sim 1\,\mathrm{GPa}$ to $10\,\mathrm{GPa}$. The PP plates are therefore representative of the sea ice density at the experimental scale but not the Young's modulus. Similarly, the Young's modulus of the PVC are representative of sea ice up to a geometric scaling factor of between 2 and 20 (i.e. floes of $2\,\mathrm{m}$ to $20\,\mathrm{m}$) but not the sea ice density.

The wave-maker was used to generate regular monochromatic water waves. They were prescribed at the periods $T = 0.6\,\mathrm{s}$, $0.8\,\mathrm{s}$, and $1.0\,\mathrm{s}$, which have corresponding wavelengths $\lambda = 0.56\,\mathrm{m}$, $1.00\,\mathrm{m}$, and $1.51\,\mathrm{m}$. The wavelengths were chosen to give representative of waves with wavelengths less than, approximately equal to, and greater than the floating plate. They forced an elastic response in the plates (particularly the PVC) because of their similar length scale (Meylan & Squire, 1994). Wave amplitudes were chosen to provide steepnesses ka=0.04, 0.08, 0.1, and 0.15, where a is the incident wave amplitude and k is the wavenumber $k = 2\pi/\lambda$, which given by the positive real root to the dispersion relation $k\tanh(kH) = \omega^2 g^{-1}$, where $\omega = 2\pi/T$ is the angular frequency of the waves, and $g = 9.81\,\mathrm{m\,s^{-2}}$ is the acceleration due to gravity. The lower steepnesses were representative of gently sloping ocean waves and the higher steepnesses representative of more storm-like conditions. In all instances the steepnesses were well below the breaking limit (Babanin *et al.*, 2007).

For the experiments analysed in this chapter a small wave probe and high-definition video camera were used to record the overwash. The camera recorded visuals in black and white at a frequency of 60 frames per second, and lights were placed around the wave-tank to better highlight the overwash. The depth probe was positioned at the geometric centre of the plate's upper surface. It had a resolution of less than $0.05\,\mathrm{mm}$ and recorded

the overwash depth at a frequency of 120 Hz for 300 s following the activation of the wave-maker. The wave-maker was run for over 300 s in all tests.

2.2.2 Qualitative experiment analysis

Figure 2.2 shows four snapshots for overwash on a 40 mm thick PP plate with incident waves of $\lambda = 0.56$ m and steepness $ka = 0.10$. In these snapshots incident waves are propagating from left to right. The initial time, $t = 0$, correlates to a point in time over 40 s after the wave-maker started and snapshots are taken at 0.15 s intervals. Solid red arrows follow the motion of water that washes onto the plate. Dashed green arrows follow the motion of water already on the plate. The snapshots are representative of all tests for incident waves with a low steepness or short wavelength.

At $t = 0$ the water waves at the upstream edge exceed the freeboard of the plate, which forces water onto the plate's upper surface. The solid red arrows at $t = 0$ and $t = 0.15$ show the formation of overwash as the upstream edge dips into the surrounding water. As this occurs the water breaks over the edge and creates turbulent effects, which is made evident in the roughness of the water's surface. This motion is distinctly different to the water above and below the upper and lower edges of the plate, which still appears to be in deep water wavelike motion. The red arrows in the snapshots at $t = 0.30$ and 0.55 s follow the motion of the water once it has washed onto the plate. The motion of this water is characterised by an abrupt jump in depth that travels much faster than than the water it is incident upon. In the context of modelling shallow-water these fast flowing abrupt jumps in depth are known as bores. They characterise water undergoing a hydraulic jump (Tan, 1992). The dashed green arrow shows the motion of a bore that is already on the plate at $t = 0$. As it washes along the plate its velocity remains relatively constant (as indicated in the constant changes in position between varying t intervals), and its depth gradually decreases. As the bore develops along the plate the turbulence behind the bore-front (the location of the abrupt change in depth) gradually decreases. The distance between the red and green bore-fronts is in the order of hundreds of millimetres, whereas the depth of the bores is in the order of millimetres. This indicates that the characteristic length of the bores is much greater than their characteristic depth; another

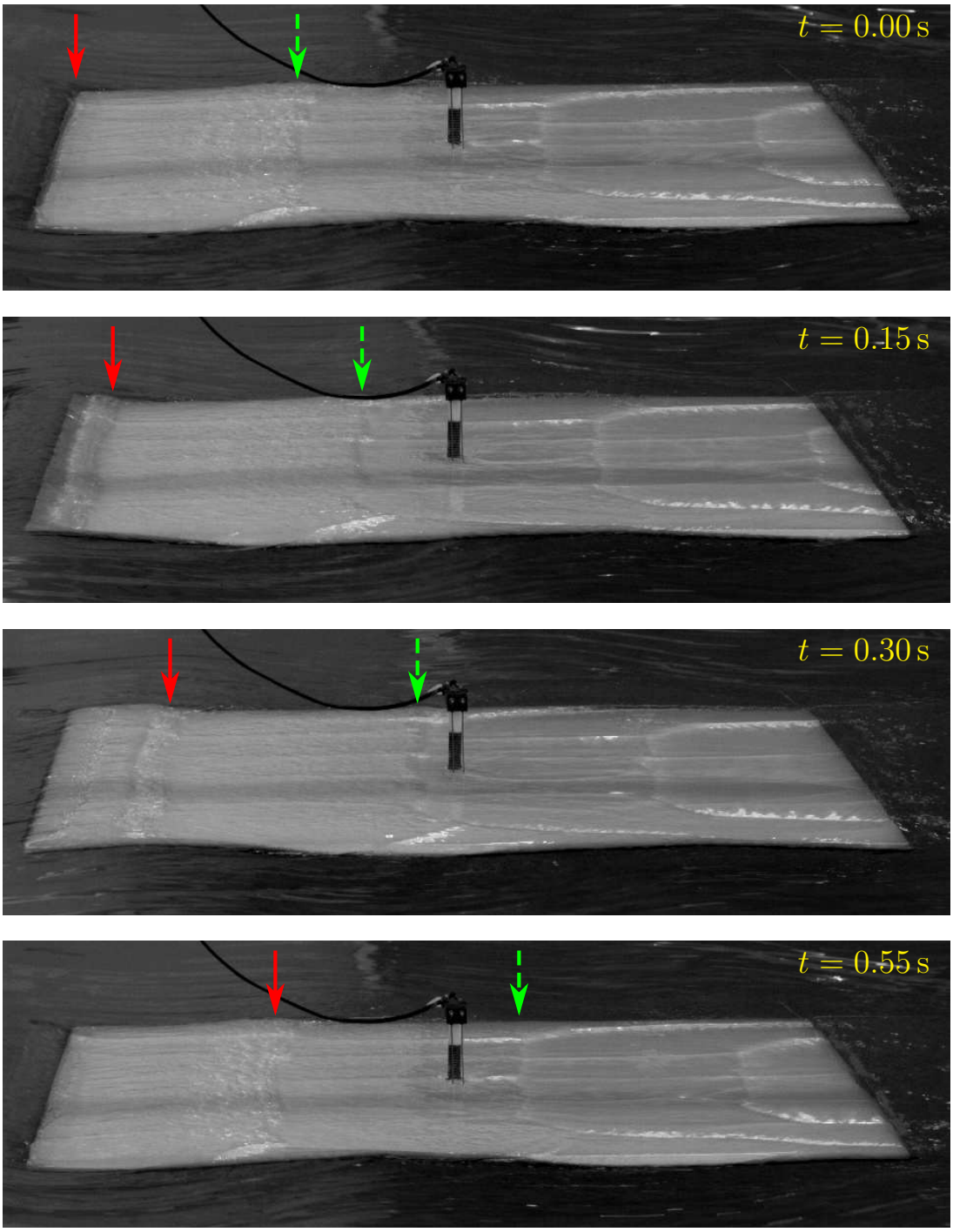

Figure 2.2: Snapshots of overwash of a 40 mm thick PP plate subjected to incident waves of steepness 0.10 and wavelength 0.56 m. Images are separated at intervals of 0.15 s and $t = 0.00\,\mathrm{s}$ corresponds to an arbitrary times more than 40 s after the wave-maker was activated. Solid red arrows indicate the water as it washes over the edge of the plate. Dashed green arrows indicate the motion of water already on the plate at $t = 0.00\,\mathrm{s}$.

distinct property of shallow-water flows (Vreugdenhil, 1994). At $t = 0.30$ and $0.55\,\mathrm{s}$ the bore marked by the dashed green arrow interacts with the bores encroaching from the upper and lower edges of the plate. However, their interference is not prevalent along the plate's centreline, indicating that three dimensional effects are of minor consequence for the overwash along the plate's centreline. For all plates and waves tested the overwash was found to be characterised by the formation of bores as water breaks over the plate's edges. Therefore, the motion of the overwash is characterised by shallow-water properties, which are significantly different to the deep water wave properties of the water around the plate's edges.

The snapshots at $t = 0$ and $t = 0.55\,\mathrm{s}$ are similar in terms of the location of bore-fronts on the plate. The similarity in pictures at $t = 0$ and $t = 0.55\,\mathrm{s}$ indicates that the motion of the overwashed water is periodic at the incident wave's period (which is $T = 0.6\,\mathrm{s}$ for $\lambda = 0.56\,\mathrm{m}$); excluding minor, random, turbulent and breaking effects. The visual taken at exactly $t = 0.60\,\mathrm{s}$ appears almost identical to that at $t = 0.00\,\mathrm{s}$, and hence is not shown as it is a repetition of the $t = 0.00\,\mathrm{s}$ panel. For all plates and waves tested the motion of the overwash was found to become periodic at the incident wave's period. This periodic motion would always occur after ~ 5 incident wave peaks interacted with the upstream edge of the plate.

Figure 2.3 shows three snapshots of overwash of a 40 mm thick PP plate with incident waves of $\lambda = 1.51\,\mathrm{m}$ and $ka = 0.15$. In these snapshots the incident waves propagate from left to right. The snapshots are spaced at $0.217\,\mathrm{s}$ time intervals and $t = 0$ corresponds to an arbitrary point in time once the motion of the ovewash has become periodic. The vertical arrows show the position of bores on the plate. The dot-dashed cyan arrows at $t = 0$ show the direction of propagation. The snapshots are representative of overwash by incident waves of large steepnesses or lengths.

The distinct difference between figures 2.3 and 2.2 is that the waves around the plate are sufficiently large such that they produce bores at the downstream edge of the plate. The reason bores form at the trailing edge for this higher amplitude incident wave cases, as opposed to those in figures 2.2, is because the transmitted wave amplitude is substantially less than the incident wave amplitude due to the constrained motion of the water beneath the plate. The bore at the downstream edge of the plate is highlighted by the rightmost

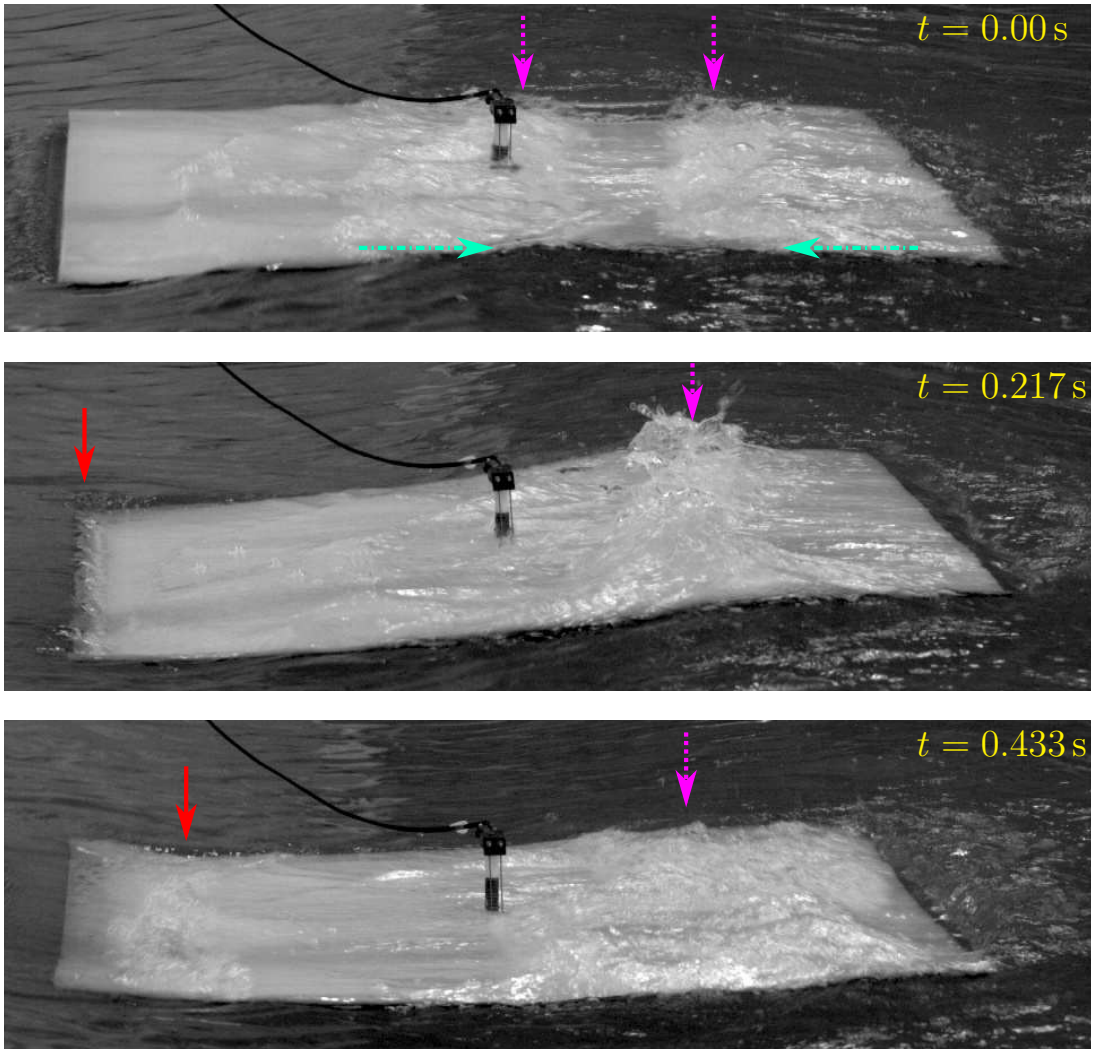

Figure 2.3: Snapshots of overwash of a 40 mm thick PP plate subjected to incident waves of steepness 0.15 and wavelength 1.51 m. Images are separated at intervals of 0.217 s and $t = 0.00\,\mathrm{s}$ corresponds to an arbitrary times more than 40 s after the wave-maker was activated. Solid red arrows indicate the water as it washes over the edge of the plate. Dotted purple arrows indicate the interaction between two bore travelling in opposite directions. Dot-dashed cyan arrows indicate the direction of the soon to collide bores.

dotted purple arrow at $t = 0$. As it has been produced at the downstream edge, it propagates in the opposite direction of the bore produced at the upstream edge, which is highlighted by the leftmost dotted purple arrow. As these bores are propagating in different directions it leads to a bore collision event shown by the dotted purple arrow at $t = 0.217\,\text{s}$. The collision is violent and is characterised by an upwards jet of water, spray, and choppy water. The aftermath of the collision is shown by the dotted purple arrow at $t = 0.433\,\text{s}$. It is characterised by choppy white water and the location of the bore-fronts can no longer be identified. This choppy water is relatively stagnant when compared to the velocity of the bores produced at the upstream and downstream edges. It is also the reason the bores-fronts at $t = 0$ in figure 2.3 are much rougher than the bore-fronts in figure 2.2. The solid red arrow at $t = 0.217$ and $0.433\,\text{s}$ shows the formation of overwash as the upstream edge dips into the water. The formation is characterised by water breaking over the plate's edge which develops into a bore. Qualitatively, the formation is like that in figure 2.2, however, the bore it produces is rougher and more turbulent around the bore-front. It is rougher and more turbulent because it is deeper and propagates faster when compared to the bores in figure 2.2, and because it is interacting with rougher water already on the plate (from the aftermath of a bore collision). Figure 2.3 therefore shows that when the surrounding waves are sufficiently large bores are produced at the upstream and downstream edge of the plate. The formation of these bores is similar to in figure 2.2. However, as they propagate in different directions, it leads to a bore collision event. This significantly complicates the overwash as it produces rough turbulent water, and the near annihilation of bore-fronts.

The depth probe at the plate's centre found that overwash occurred in 67 of the 72 tests conducted. For the 67 tests where overwash did occur the maximum depth reading at the plates centre was $9.98\,\text{mm}$ and the mean overwash depth across all cases (once periodic motion occurred) was $1.77\,\text{mm}$. Therefore, the overwash depth was always found to be an order of magnitude or less than the amplitude of the incident wave. As expected, the overwash was found to become deeper, faster, and more likely to occur for the denser plate, lower plate thickness, as the incident waves became steeper, or as the wavelength of the incident waves increased (note that the latter condition corresponds to an increased amplitude for an equivalent steepness). When shallower and slower overwash occurred,

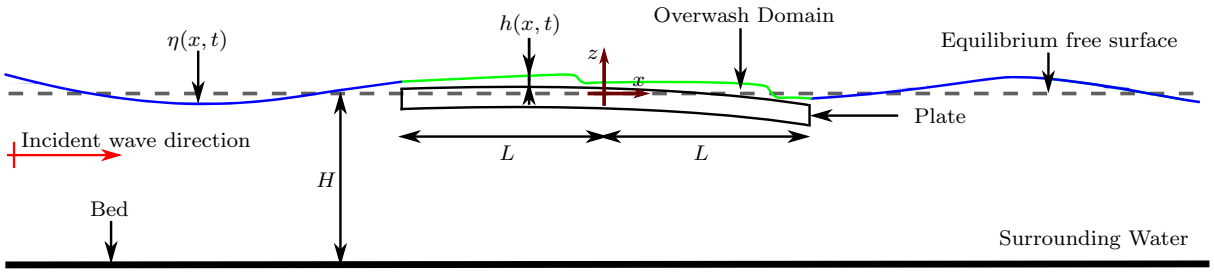

Figure 2.4: Schematic of mathematical model (not to scale).

it was correlated to when bores were only produced at the upstream edge only. When deeper, faster, and more energetic overwash occurred, it was correlated to bores being produced at the upstream and downstream edges. As shown by the contrast of figures 2.2 and 2.3, when bores were produced at both plate edges the qualitative properties of the overwash would distinctly differ; emphasising the nonlinear behaviour of overwash.

The Reynolds number of the overwash was approximated using the time averaged depth at the plate's centre, D, and videos to approximate its horizontal velocity, u. It is given as $Re = uD/\upsilon$, where and $\upsilon = 1.00 \times 10^{-6}\,\mathrm{m^2\,s^{-1}}$ is the kinematic viscosity of water at atmospheric pressure and $20\,\mathrm{C}^\circ$ (Mills, 1999). When overwash did occur, and for the time intervals where it was periodic, the Reynolds number ranged from $Re \sim 200$ to $Re \sim 3000$. The most similar flow that has been studied experimentally to compare this Re to is uniform steady flow in open channels. For uniform steady flow in open channels, the transition region between turbulent and laminar flow is generally quoted as 'ill-defined' but typically $500 < Re < 2000$ (Chow, 1959), or $500 < Re < 12500$ (Akan, 2011). This implies the overwashed water is laminar with turbulent instabilities. This diagnosis is evident in figures 2.2 and 2.3 where the bore-fronts are rough and contain turbulence whereas the rest of the overwash appears relatively laminar.

2.3 Mathematical model

Figure 2.4 shows a schematic of the wave basin used for the mathematical model. The wave basin is described using the (x, z) Cartesian coordinate system where incident waves travel in the positive x-direction and gravity acts in the negative z direction. The motion of waves, overwash, and the plate are assumed to be constant in the direction perpendicular

to z and x, which prevents the need for a further y coordinate. This two dimensional assumption is made (i) for simplicity, (ii) because the investigation into plate motion found three dimensional effects to be negligible (Meylan *et al.*, 2015), and (iii) because the snapshots of the experiments found the effect of bores washing over the side of the plate to be small compared to the bores travelling in the incident wave's direction. The line $z = 0$ is aligned with the water's equilibrium free surface height and the origin of the coordinate system is located at the geometric centre of the plate. The surge and drift of the plate are assumed to be negligible and therefore the plate covers the water's surface between $x = -L$ and $x = L$. The basin's bed is flat and the distance between the water's equilibrium free surface level and basin bed is H. Waves reflected by the basin's boundaries are assumed to be negligible and therefore the x-direction extends to positive and negative infinity. The model does not include the transient build-up of the overwash because the experiments found the overwash would become periodic after ~ 5 wave peaks hit the plate's upstream edge, i.e. it would become periodic over a short time interval. Hence, the initial time, $t = 0$, corresponds to an arbitrary point in time once the plate, wave, and overwash motion has become cyclical.

The water in the model is assumed to be incompressible, irrotational and inviscid. Although the overwash interaction does contain turbulence, the inviscid assumption is made because green water models were able to model water waves washing onto ship without including turbulence (e.g. Buchner, 2002; Nielsen & Mayer, 2004; Greco *et al.*, 2007); for which the Reynolds number is at least an order of magnitude larger than found in the experiments of section 2.2. Using a similar justification it is also assumed that surface tension is negligible. The motion of the plate is assumed to follow the predictions linear potential theory as this was found to be valid in these experiment in Meylan *et al.* (2015). Similarly, it assumed that the effect the overwash has on the surrounding waves is sufficiently small such that the overwash can be forced without consideration of how it perturbs the surrounding waves. Although it has been established that overwash does affect the surrounding waves in Bennetts *et al.* (2015), this assumption is made to circumvent the need for complicated coupling conditions between overwash and surrounding waves. The model, therefore, uses linear potential theory to model wave and plate motion, and uses the outputs of linear potential theory provide boundary conditions

for the overwash.

2.3.1 Wave and plate motion

The preceding derivation follows the standard procedure for modelling the plate and wave motion using linear potential theory (Mei *et al.*, 1989; Squire *et al.*, 1995). Following the incompressible, irrotational and inviscid assumption, the water's motion is described using the complex valued velocity potential $\phi(x, z, t)$. It describes the velocity of the water in the x-direction, $u(x, z, t)$, and the velocity of the water in the z-direction, $w(x, z, t)$, via

$$(u, w) = \mathrm{Re}\,(\nabla\phi)\,, \tag{2.1}$$

where the operation $\nabla(\bullet) = (\partial_x\bullet, \partial_z\bullet)$, and the operation $\mathrm{Re}\,(\bullet)$ takes the real part of $\bullet$. The motion of the water is assumed to be time harmonic at the incident wave's angular frequency (ω) because the model does not include overwash build-up, the wave-maker generates regular monochromatic incident waves, and the overwash was found to cycle at this frequency. Hence, the velocity potential is given as $\phi = \widetilde{\phi}(x, z)\mathrm{e}^{\mathrm{i}\omega t}$, where $\widetilde{\phi}(x, z)$ is the time independent (i.e. frequency domain) component of the velocity potential. Note that overhead tildes are used throughout this derivation when the variable needs to be considered in the time and frequency domain. The free surface displacements are assumed to be of low steepness and small relative to the water depth. Thus, the free surface condition of the water to the left and right of the plate's edges is linearised about the equilibrium depth. The basin bed is modelled as impenetrable. The equations of motion of the water are therefore given by

$$\nabla^2\widetilde{\phi} = 0 \qquad \text{for} \quad -H < z < 0 \quad \text{and all } x, \tag{2.2a}$$

$$\partial_z\widetilde{\phi} = 0 \qquad \text{on} \quad z = -H, \text{ and} \tag{2.2b}$$

$$\partial_z\widetilde{\phi} - \alpha\widetilde{\phi} = 0 \qquad \text{on} \quad z = 0 \quad \text{for } |x| > L \tag{2.2c}$$

where $\alpha = \omega^2 g^{-1}$. Equation 2.2a is given because the water is irrotational and incompressible, equation 2.2b is the no-penetration condition along the basin's bed, and equation 2.2c is the linearised free surface condition. As the linearised free surface condition is used,

the free surface of the water, $\eta(x,t)$, is given by

$$\eta = \mathrm{Re}\left(-\frac{1}{g}\partial_t\phi\right) = \mathrm{Re}\left(-\frac{\mathrm{i}\omega}{g}\widetilde{\phi}\mathrm{e}^{\mathrm{i}\omega t}\right) \quad \text{for } |x| > L. \tag{2.3}$$

As the incident wave is harmonic with angular frequency ω its (frequency domain) complex potential is given as

$$\phi_I = A\mathrm{e}^{-\mathrm{i}k_0 x}\psi_0(z), \quad \text{where} \quad \psi_n(z) = \cosh\left(k_n\left(z+H\right)\right)\mathrm{sech}\left(k_n H\right), \tag{2.4}$$

$A = \mathrm{i}ag\omega^{-1}$, and k_0 is the positive real root to the dispersion relation

$$k\tanh(kH) = \alpha, \tag{2.5}$$

and k_n, for n the set of integers ≥ 1, are the negative imaginary solutions to the dispersion relation (2.5) in ascending order with respect to their magnitude.

For $x < -L$ the potential is decomposed into $\widetilde{\phi} = \phi_R + \phi_I$, where ϕ_R is the reflected potential. For $x > L$ the potential is decomposed into $\widetilde{\phi} = \phi_T$, where ϕ_T is the transmitted potential. Physically, ϕ_R and ϕ_T correspond to the waves reflected and transmitted by the plate, respectively. Wave energy is allowed to propagate freely out towards positive and negative infinity. The velocity potential therefore satisfies the Sommerfeld radiation condition

$$\partial_{|x|}(\bullet) + \mathrm{i}k_0(\bullet) \to 0 \tag{2.6}$$

for $\bullet = \phi_T$ as $x \to \infty$ and $\bullet = \phi_R - \phi_I$ as $x \to -\infty$.

Solved as a boundary value problem using separation of variables, equations 2.2 to 2.6 give

$$\widetilde{\phi} = A\mathrm{e}^{-\mathrm{i}k_0 x}\psi_0 + \sum_{n=0}^{\infty} R_n \mathrm{e}^{\mathrm{i}k_n x}\psi_n \qquad \text{for } x < -L, \text{ and} \tag{2.7}$$

$$\widetilde{\phi} = \sum_{n=0}^{\infty} T_n \mathrm{e}^{-\mathrm{i}k_n x}\psi_n \qquad \text{for } x > L, \tag{2.8}$$

where R_n and T_n are the as yet unknown complex reflection and transmission coefficients, respectively, with corresponding wavenumbers k_n. In this description, R_0 and T_0 correspond to the waves that propagate out infinitely far from $x = -L$ and $x = L$ (i.e. the plate's edges), respectively, and R_n and T_n for $n \geq 1$ correspond to the exponentially decaying (evanescent) waves that propagate out from $x = -L$ and $x = L$, respectively.

The plate is assumed to be thin, long, undergo small elastic deflections (as indicated by the linearisation of the free surface), have uniform properties in all spacial directions, and oscillate at the angular frequency of the incident wave. Its deflection about its static equilibrium, $\xi(x,t) = \widetilde{\xi}(x)\mathrm{e}^{\mathrm{i}\omega t}$, can therefore be modelled using various beam theories such as Euler-Bernoulli beam theory or Timoshenko beam theory. In this model Euler-Bernoulli beam theory is used because it was found to be valid for the plate motion given in these experiments (Meylan *et al.*, 2015), and because it the simpler description. The deflection of the plate is therefore governed by

$$D\partial_x^4\widetilde{\xi} - \omega^2\gamma\widetilde{\xi} = q, \tag{2.9}$$

where $D = d^3E_p\left(12\left(1-\nu\right)\right)^{-1}$ is the flexural rigidity of the plate, $\gamma = h\rho_p$ is the mass per unit length of the plate, and $\widetilde{q}(x,t) = q(x)\mathrm{e}^{\mathrm{i}\omega t}$ is the pressure applied to the plate along its upper and lower surfaces.

As the plate is freely floating its boundary conditions are the zero bending moment and zero sheer stress conditions at the plate's edges. These are

$$\partial_x^3\widetilde{\xi} = 0 \quad \text{and} \quad \partial_x^4\widetilde{\xi} = 0 \tag{2.10}$$

on $z = 0$ at $x = \pm L$, respectively (Timoshenko & Woinowsky-Krieger, 1959).

Equation 2.9 implies the natural modes of vibration of the plate are given by the eigenfunctions, ξ, that satisfy

$$\partial_x^4\widetilde{\xi} = \mu^4\widetilde{\xi} \tag{2.11}$$

with corresponding eigenvalues, μ. Solved as a differential equation with boundary conditions 2.10, this gives the first two modes of vibration as

$$\xi_0 = \frac{1}{\sqrt{2L}} \quad \text{and} \quad \xi_1 = x\sqrt{\frac{3}{2L^3}}, \tag{2.12}$$

which correspond to heave and pitch respectively. The higher order modes of vibration are given by

$$\xi_{2n} = \frac{1}{\sqrt{2L}}\left(\frac{\cos(\mu_{2n}x)}{\cos(\mu_{2n}L)} + \frac{\cosh(\mu_{2n}x)}{\cosh(\mu_{2n}L)}\right) \qquad \text{and} \tag{2.13a}$$

$$\xi_{2n+1} = \frac{1}{\sqrt{2L}}\left(\frac{\sin(\mu_{2n+1}x)}{\sin(\mu_{2n+1}L)} + \frac{\sinh(\mu_{2n+1}x)}{\sinh(\mu_{2n+1}L)}\right), \tag{2.13b}$$

for $n = 1, 2, \ldots$, which correspond to the symmetric and asymmetric bending modes, respectively. The eigenvalues in 2.13 are given as the real roots (in ascending order) to the equations

$$\tan(\mu_{2n}) + \tanh(\mu_{2n}) = 0 \quad \text{and} \quad \tan(\mu_{2n+1}) - \tanh(\mu_{2n+1}) = 0 \quad \text{for} \quad n = 1, 2, \ldots. \tag{2.14}$$

The deflection of the plate in the frequency domain is therefore given by

$$\widetilde{\xi} = \sum_{n=0}^{\infty} \zeta_n \xi_n \tag{2.15}$$

where ζ_n are the, as yet unknown, complex modal coefficients.

The plate's lower surface is assumed to remain in contact with the water for all t, and the atmospheric pressure is normalised to zero. Hence, the pressure applied to the plate is given by

$$q = p_w \quad \text{on } z = \widetilde{\xi} \quad \text{for } |x| < L, \tag{2.16}$$

where p_w is the pressure of the water beneath the plate. As the water is irrotational, incompressible, and deflections of the plate are assumed to of low steepness, the pressure of the water beneath the plate is given by the linearised unsteady Bernoulli equation. Hence,

$$p_w = -\rho_w \partial_t \phi - \rho_w g \xi \quad \text{on } z = 0. \tag{2.17}$$

Equations 2.9, 2.16, and 2.17 therefore give

$$D\partial_x^4 \widetilde{\xi} - \omega^2 \gamma \widetilde{\xi} + \mathrm{i}\rho_w \omega \widetilde{\phi} + g\rho_w \widetilde{\xi} = 0 \quad \text{on } z = 0 \quad \text{for } |x| < L. \tag{2.18}$$

This is the dynamic coupling condition between water and plate motion. Equations 2.11 and 2.15 give this condition with respect to the eigenfunctions of the plate as

$$D \sum_{n=0}^{\infty} \left(\mu_n^4 \zeta_n \xi_n\right) - \left(\omega^2 \gamma - g\rho_w\right) \sum_{n=0}^{\infty} \left(\zeta_n \xi_n\right) + \mathrm{i}\omega\rho_w \widetilde{\phi} = 0 \tag{2.19}$$

for $|x| < L$ and $z = 0$.

As the water and lower surface of the plate are assumed to remain in contact for all t, the velocity of the plate must match the velocity of the water along $z = \xi$. This implies

$$\partial_t \xi = \mathrm{i}\omega \widetilde{\xi} = \partial_z \widetilde{\phi} \quad \text{on } z = 0 \quad \text{for } |x| < L. \tag{2.20}$$

This is the kinematic coupling condition between the plate and water beneath.

Using this dynamic and kinematic coupling condition the values of ζ_n, R_n and T_n can be solved using a Green's function method (e.g. Meylan & Squire, 1994; Newman, 1994) or an eigenfuction matching method (Fox & Squire, 1994; Linton & McIver, 2001). The Green's function method uses a Green's function corresponding to a unit impulse at the free surface. The eigenfunction matching method uses the orthogonality of the eigenfunctions to match velocity potential beneath the plate to the velocity potential of the surrounding waves. The eigenfunction matching method requires direct calculation of the velocity potential beneath the plate whereas the Green's function method does not. As this model does not require the knowledge of the water's motion beneath the plate the Green's function method is used.

The Green's function method is presented in Appendix A. It directly follows Newman (1994), which is a similar technique to that found in Meylan & Squire (1994), but slightly simpler to apply in this problem. It is used to calculate ζ_n, R_n, and T_n. These variables give the solution for the plates motion via equation 2.15. They also give the solution for velocity potential to the left and right of the plate (equations 2.7 and 2.8). This allows the free surface to the left and right of the plate to be calculated via equation 2.3, and the velocity of the water to be calculated using equation 2.1. In this model n is truncated to 100, for which numerical testing found for the parameters of u, w, η, and ξ converged to well within 1%.

2.3.2 Overwash

Aside from the breaking of water over the plate's edges and bore collisions, the overwash is characterised by long and shallow bores. Therefore, it is assumed that in the overwashed water the characteristic horizontal length scale, C_x, is much greater than the characteristic vertical length scale, C_z — the standard assumption for shallow-water theory (Tan, 1992; Vreugdenhil, 1994). Under this assumption $w \ll u$, implying that the vertical velocity of the overwash is negligible with respect to the horizontal velocity. Furthermore, by decomposing

$$u(x, z, t) = \hat{u}(x, t) + u'(x, z, t), \tag{2.21}$$

where $\hat{u}$ is the depth averaged horizontal velocity and u' the variations of u from $\hat{u}$ about z, it also implies that $u' \ll \hat{u}$ (because $C_z \ll C_x$). This means that the changes in u about z are negligible.

If the water's bed is stationary these conditions imply the overwash can be described using the nonlinear shallow-water equations (see e.g. Vreugdenhil, 1994). However, in this circumstance, the water is moving along a non-stationary bed (i.e. $\mathrm{Re}\,(\partial_t \xi) \neq 0$). Even so, post-processing of the wave-plate model found that (i) $\mathrm{Re}\,(\partial_t^2 \xi) \ll g$, implying the pressure induced by the upper surface of the plate is negligible with respect to gravity, (ii) that $\mathrm{Re}\,(\partial_x \xi) \ll 0.1$, implying the slope of the plate is negligible, and (iii) $\mathrm{Re}\,(\partial_t \xi) \ll V_b$, (where V_b is the characteristic velocity of the bores found in the experiments), implying the vertical velocity of the plate is negligible. This implies that the motion of the plate is negligible with respect to the motion of the overwash (Tan, 1992). Therefore, the motion of the overwash is modelled by the nonlinear shallow-water equations, which are

$$\partial_t (h) + \partial_x (h\hat{u}) = 0 \qquad \text{and} \tag{2.22a}$$

$$\partial_t (h\hat{u}) + \partial_x \left(\frac{1}{2} g h^2 + h\hat{u}^2 \right) = 0 \tag{2.22b}$$

for $-L < x < L$ and $z > z_b$. In this description $h(x,t)$ is the water's depth, which is given by

$$h = \eta - z_b, \tag{2.23}$$

$\eta(x,t)$ is the water's free surface, and $z_b(x,t)$ is the upper surface of the plate.

Equations 2.22 are a system of nonlinear hyperbolic partial differential equations, where equation 2.22a represents the conservation of mass, and equation 2.22b represents the conservation of momentum. As they are nonlinear are distinctly different to the equations that govern of motion of the surrounding water — one of the main reasons a dynamic 'two-way' coupling condition between the overwash and surrounding water is not pursued. Further, unlike the equations that describe the motion of the surrounding domain, they do not elicit a general solution; although, analytic solutions do exist for certain initial and boundary conditions, such as the famed 'dam-break problem' (Billingham & King, 2000).

An important property of these equations is that when the water transitions from sub-critical to super-critical, which is when the Froude number,

$$Fr = \hat{u}/\sqrt{gh}, \tag{2.24}$$

passes positive or negative unity, a shock is produced. Physically, these shocks manifest as fast-travelling instantaneous changes in h and $\hat{u}$, i.e. the shocks create bores (Vreugdenhil, 1994). The value of Fr also around the domain's edges also influences the necessary number of boundary conditions for a well-posed shallow-water problem. For a boundary to the left of the domain, if $Fr < -1$ the equations require no boundary conditions at the edge, for $-1 < Fr < 1$ the equations require one boundary condition at the edge, and for $Fr > 1$ the equations require two boundary conditions at the edge. The same can be said of a rightmost boundary to the domain, but with the negative value of Fr. It is, however, sufficient to specify two boundary conditions (i.e. over-prescribe the boundary conditions) at the edges for all t, but such forcing results in a discontinuity (in physical terms, a hydraulic jump) at the boundary (Tan, 1992). One of the main reasons the shallow-water equations, as opposed to other shallow-water descriptions, are used to model the overwash is that they allow this over-prescription of boundary conditions. In particular, it is why the overwash is not modelled using a more sophisticated shallow-water description such as the Bossonesq equations used in the submerged shelf problem of Grue (1992).

The overwash boundary conditions are set such that the shallow-water depth matches the depth predicted by linear potential theory when linear potential theory predicts the waves exceed the height of the plate's edges, or be zero otherwise. Likewise, the depth averaged horizontal velocity is set to match the horizontal velocity predicted by linear potential theory at the free surface when linear potential theory predicts the waves exceed the height of the plate's edges, or be zero otherwise. This kind of 'one-way' forcing us used because the model assumes the overwash can be forced without consideration of how it affects the surrounding wave and plate motion. Therefore the conditions

$$h(\pm L^{\pm}, t) = \max\left(\eta(\pm L^{\pm}, t) - z_b(\pm L, t), 0\right), \tag{2.25a}$$

are used to match the depth of the overwash with the amount the water wave's free surface exceed the height of the plate's respective edges. Likewise, the conditions

$$\hat{u}(\pm L^{\pm}, t) = \begin{cases} \mathrm{Re}\left(\partial_x \phi(\pm L^{\pm}, 0, t)\right) & \text{if } \eta(\pm L^{\pm}, t) \geq z_b(\pm L, t), \\ 0 & \text{otherwise,} \end{cases} \tag{2.25b}$$

are used to match the velocity of the water waves to the overwash if the water waves exceeds the height of plate's respective edges, or be zero otherwise. In these conditions the location of the plate's upper surface (z_b) is approximated by the sum of the static freeboard (given by Archimedes' principle) plus the dynamic response (from the wave-plate motion model). Therefore, it is given as

$$z_b = \mathrm{Re}\,(\xi) + d(1 - \rho_p \,/\, \rho_w) \tag{2.26}$$

where ξ is as calculated in section 2.3.1 and the final term is the static freeboard given by Archemedies' principle. Note that this submergence was not used in the derivation of the plate motion because it comprises a small portion of the overall domain. The boundary conditions 2.25 are defined using parameters above and below the edges, where L^+ denotes the value taken as $x \to L$ from above and L^- denotes $x \to L$ from below. They are defined in this manner because forcing two boundary conditions for all t does not guaranteed η and u are continuous or smooth over the boundary.

The qualitative properties of the boundary conditions are illustrated when considering the characteristic plate. In the characteristic plate, boundary conditions 2.25 produce the characteristics $X_+(x,t)$ and $X_-(x,t)$ that emanate from the boundaries (i.e. at $x = \pm L$) for $t > 0$. The associated slopes of the $X_\pm(x,t)$ characteristics are $\mathrm{d}X_\pm / \,\mathrm{d}t = \hat{u} \pm \sqrt{gh}$, respectively, which have corresponding Riemann invariant, $R_\pm = \hat{u} \pm 2\sqrt{gh}$ (Tan, 1992). Hence, if $\eta < z_b$, the boundary conditions do not force characteristics into the domain. This implies the overwash is not affected by the surrounding waves, which also allows water to wash off the plate if $\eta < z_b$ above and below the edges. When characteristics do enter the domain, although they are functions of $\hat{u}$ and h, neither of these characteristics directly specify $\hat{u}$ and h. Additionally, the characteristics entering/exiting the domain through boundary conditions 2.25 at some arbitrary $t = t_0$ are not influenced by the characteristics entering/exiting at some future time $t = t_0 + \Delta t$. Therefore, over the edges, neither h or $\hat{u}$ are guaranteed to be smooth or continuous, which results in the aforementioned discontinuities at $x = \pm L$.

A shock-capturing numerical scheme is used to solve the shallow water problem 2.22–2.25, rather than pursuing an analytic solution. The scheme consists of Kurganov & Tadmor (2000)'s finite volume method in space and the total diminishing second-order

Runge-Kutta method in time (Gottlieb & Shu, 1998). The scheme is used because it is second order accurate and has been shown to capture chocks exceptionally well in similar problems (Kurganov & Tadmor, 2000). Therefore, it is capable of modelling the bores and discontinuities at the plate's edges. The method is presented in Appendix B. The method solves $\hat{u}$ and h at M equally spaced volumes between $x = -L$ and L. In this model the width of the volumes is set to $\Delta x = 0.25\,\text{mm} \ll a$ to maximise the accuracy around bore-fronts. Larger volume widths could potentially be used and give similar accuracy and improved run-times, although this was not investigated as part of this research.

Boundary conditions 2.25 are prescribed at the ghost volumes centred at $x = -L - 0.5\Delta x$ and $x = L + 0.5\Delta x$, and are implemented using two different solutions for the velocity potential. The first solution does not include the evanescent waves around the plate, i.e. it uses the solution for T_0, R_0 and sets $T_n = R_n = 0$ for $n > 0$. The second solution includes the evanescent waves around the plate, i.e. it uses the solution all R_n and T_n. The former condition is tested because it is simpler and because the overwash is known to affect the waves around the plate, i.e. the locations where evanescent modes (waves) are present. The latter solution is tested because it is the full solution for the potential. The evanescent wave model uses the simplification of the velocity condition boundary (equation 2.25b) to $\partial_x\phi(\pm L^{\pm}, 0, t) = 0$ for all t. The simplification is made because (i) the velocity becomes singular at $x = \pm L$ and $z = 0$ when evanescent waves are included (as indicated by Williams & Porter, 2009, although that investigation was for a plate with draft), and (ii) because in practice the velocity just below z_b must be zero as the water cannot penetrate the plate's edges. The ability for water to wash onto the plate despite prescribing $\partial_x\phi(\pm L^{\pm}, 0, t) = 0$ will be described in greater detail in chapter 3 when an overwashed step is investigated, and is a result of the characteristics not directly prescribing $\hat{u}$.

Initially, the overwash domain is set such that the water is stationary and with a uniform depth of $h = 0.01\,\text{mm}$. Long term effects were found to be invariant of the initial depth, and it is prescribed purely as an artificial mechanism to speed-up initial time steps in the model. For a prescribed incident wave, the shallow-water equations are run to a quasi-steady state, i.e. until the overwash depth signals became periodic for all x. This was found to occur for $t < 40T$, and results are therefore presented for $t > 40T$.

2.4 Experiment and model comparisons

Using the same plate and wave conditions as in the experiments of section 2.2, the mathematical model, for both sets of boundary conditions, accurately predict that of overwash occurs in all 67 cases where the overwash occurred in experiments. They also predict overwash occurs in 4 of the 15 cases where overwash did not occur in experiments. In all cases where overwash would not occur in experiments, but is predicted by the models, the models predict average depths of less than 0.5 mm at the centre of the plate, and generally less than 0.2 mm. Therefore, the models with and without evanescent waves are apt at predicting when overwash occurs. In turn, this implies that linear potential theory validly predicts when overwash will occur.

Visually, when overwash occurs in the mathematical model, it develops into thin and long bores like those found in the experiments. Figures 2.5(a) and (c) shows snapshots of the experiments (top) aligned with visualisations of the mathematical model (bottom). In (a) the plate is 20 mm thick PP subject to incident waves of steepness $ka = 0.08$ and wavelength $\lambda = 0.56$ m. In (c) the plate is 10 mm thick PVC with incident waves of $ka = 0.10$ and $\lambda = 1.00$ m. The visualisation of the mathematical model is for the no-evanescent wave boundary conditions, which was found to look exactly the same as for the evanescent wave boundary conditions. In the model visualisation the vertical length scale has been magnified to better highlight the bores. Videos of the visual comparison between experiments and theoretical models (but with incident waves travelling from right to left) for these two overwash cases (and others) can be found in the freely available electronic submission material of the related paper Skene *et al.* (2015)[1]

The red arrows in panels (a) and (c) show the relative positions of each bore on the plate. They show that the model predicts the same number of bores found in experiments, and with bore-fronts of similar shapes. They also show that the bore-fonts are in roughly the same position. Therefore, the distances between bore-fronts are also similar, which indicates the bores travel at similar speeds. The primary difference between the model

[1]URL: https://www.cambridge.org/core/journals/journal-of-fluid-mechanics/article/modelling-water-wave-overwash-of-a-thin-floating-plate/5B942B1781D5579860FD0FD261223F92#fndtn-supplementary-materials

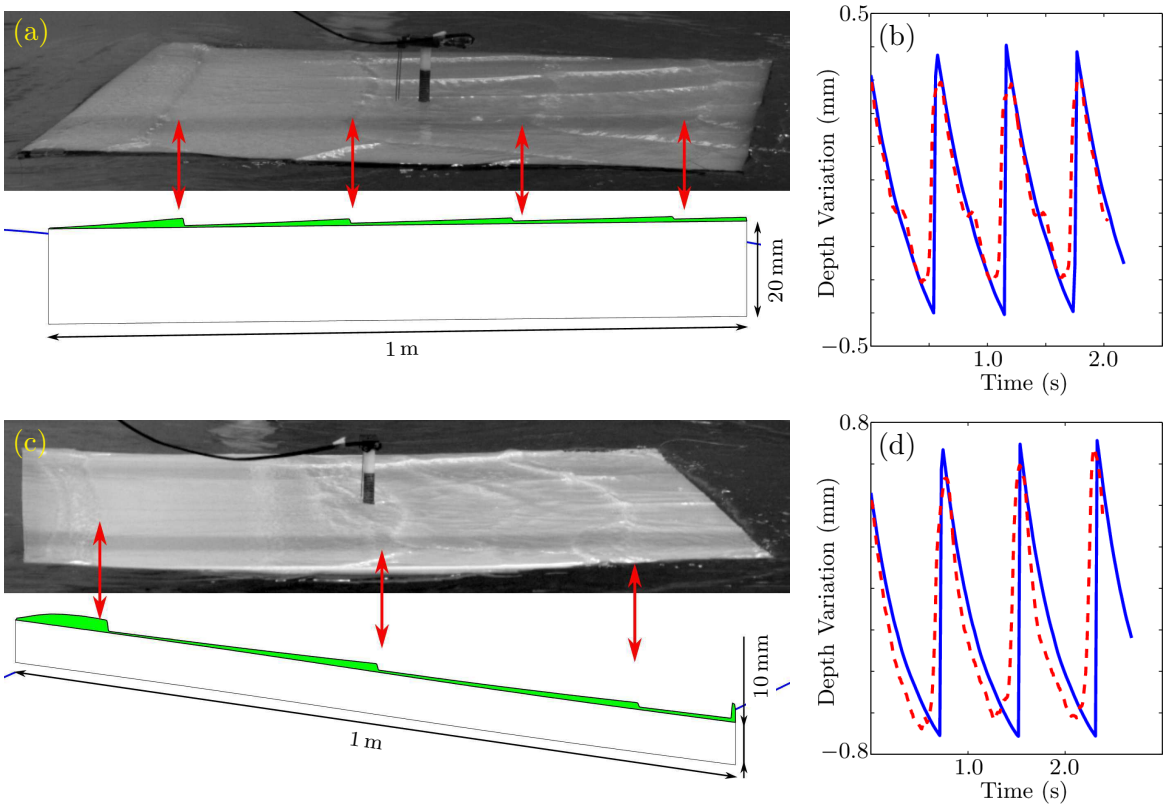

Figure 2.5: Comparisons of visualisations of experiments to mathematical model (a and b) with red arrows illustrating the relative location of bores. Comparisons of depth signal at the centre of the plate (b and d), with experiments in dashed red, and mathematical model in solid blue. Panels (a) and (b) are for 20 mm thick PP and incident waves of $ka = 0.08$ and $\lambda = 0.56$ m. Panels (c) and (d) are for 10 mm thick PVC and incident waves of $ka = 0.10$ and $\lambda = 1.00$ m.

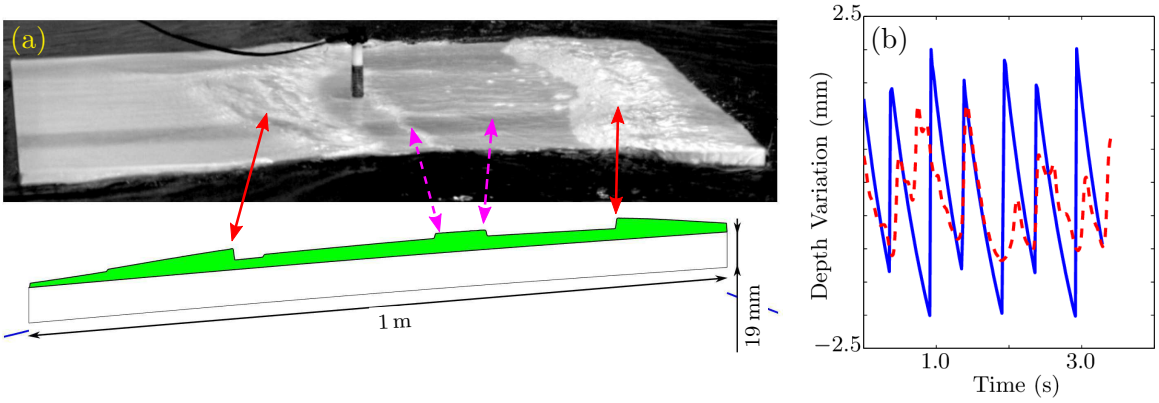

Figure 2.6: As in figure 2.5(a) and (b) but for a 19 mm thick PVC plate subjected to incident waves of $\lambda = 1.56$ m and $ka = 0.15$. Dashed purple arrows in panel (a) show the aftermath of a bore collision for experiment and mathematical model.

and experiment is that the model does not contain the bores created at the side edges, although this appears to have minimal impact on the overwash along the centreline of the plate. Both (a) and (c) are representative of when overwash was not created at the plate's downstream edge. Therefore, they show that the model predicts bores of a similar nature, similar velocity, and similarly distributed along the plate when overwash is created at only the upstream edges of the plate.

Figures 2.5(b) and (d) show the variation of the water's depth about it's mean value for the depth probe at the geometric centre of the plate. Panel (b) uses the same wave and plate conditions as in (a), and panel (d) uses the same wave and plate conditions as in (c). Results are presented for the mathematical model using the no-evanescent wave boundary conditions (solid blue), and experiments (dashed red). The mathematical model using the evanescent wave boundary conditions is not shown because it was near identical to the model without evanescent waves. The time $t = 0$ is offset such that their peaks occur at the same time. The peaks of these signals correspond to when the bore-fronts are at the centre of the plate.

The period of all signals are equal to the period of the incident wave, which is because the overwash is cyclical at the same period of the incident wave. In (b) the peak to trough difference of the model is approximately 0.78 mm, which compares favourably to the peak to trough variation of 0.66 mm seen in the experiments. In (c) the peak to

trough difference of the model is approximately 1.5 mm, which again compares favourably to the peak to trough variation of 1.4 mm seen in the experiments. The major difference between signals is that the experiments have flattening around their extrema, which is due to the breaking effects around the bore-fronts. The signal in (b) also contains a small shoulder at -0.1 mm, which is created by the bores washing from the side edges of the plate. The shoulder, however, is small relative to the peak created by the bores travelling from upstream to downstream. This again indicates the effects of the bores washing from the side of the plate are small. These signals are representative of all cases where overwash would not form at the downstream edge of the plate. The mathematical model therefore predicts the amplitude, frequency, and general shape of the depth signals well when overwash is not formed at the downstream edge of the plate. In conjunction with the results for panels (a) and (c), these results imply that, if bores do not form at the downstream edge of the plate, the mathematical model predicts qualitatively similar overwash to that found in experiments.

Figures 2.6(a) and (b) are as in 2.5(a) and (b) but for 19 mm thick PVC subjected to incident waves of steepness $ka = 0.15$ and wavelength $\lambda = 1.56$ m. Note that a video comparing experiments and theoretical models for this overwash case can be found in the freely available electronic submission material of the related paper Skene *et al.* (2015). In contrast to the cases in figure 2.5, figure 2.6 is representative of when overwash would also form at the trailing edge of the plate.

In figure 2.6(a) the leftmost solid red arrow show a bore created at the upstream edge (travelling from left to right) and the rightmost solid red arrows shows a bore created at the downstream edge (travelling from right to left). Compared to figure 2.5 the bores are no longer in similar positions because the bores in the experiments have travelled a greater distance along the plate. Further, the shape of the bore-fronts are distinctly different because the experiments contain a considerable amount of choppy water. As discussed in section 2.2.2, this is because of the by turbulence and breaking effects created by prior bore collisions. The dashed purple arrows show the aftermath of the collision of the bores. In the mathematical model the leftmost arrow points to a bore travelling from right to left, and the rightmost arrows points to a bore travelling from left to right. The bore collision in the mathematical model therefore results in two bores passing through each

other. In contrast, the leftmost arrow of the experiments show a bore-front travelling from left to right but there is no discernible bore-front for the rightmost arrow to point to. Hence, in the experiments, the collision has resulted in a single bore, rather than the two bores passing through each other seen in the mathematical model. Therefore, the mathematical model is not accurately capturing the collision between bores, nor is it capturing the how these collisions produce the choppy water that alters the properties of the bores washing onto the plate.

Figure 2.6(b) exemplifies this point. The signal of the mathematical model shows two distinct peaks and troughs per wave period, where one peak corresponds to a bore travelling from left to right, and the other corresponds to a bore travelling from right to left. The experiment's signal is not at all similar. The signal is neither strongly periodic, nor does it contain discernible peaks that can be attributed to bores. Instead, it consists of highly random depth variations created by the choppy water produced from the bore collisions. As in figure 2.6(a), this indicates that the mathematical model does not show favourable qualitative agreement with the experiments when bore collisions occur.

Figure 2.7 shows the mean depth of the overwash at the centre of the PP plate for all incident waves tested. Results are presented for the experiments (dashed red with circles), mathematical model with no-evansecent waves boundary conditions (solid blue with squares), and mathematical model with evanescent waves (dotted black with triangles). Results are sorted such that, when a bore created at the downstream edge would propagate more than $\sim 100\,\mathrm{mm}$ upstream, the marker of changes to a cross. The crosses are therefore indicative of when the respective models or experiments would predict a bore collision on the plate.

For both the models and experiments individual plots show the mean depth increases as ka increases. Additionally, for the models and experiments, individual rows show for equivalent d and ka, the mean depth increases as λ increases. Further, for models and experiments, the contrast between rows show that for an equivalent ka and λ, the mean depth increases as d decreases. The trends in the data are therefore similar for the models and experiment.

Figure 2.7 also shows that the no-evanescent waves boundary condition predicts no bore collisions in 28 of the 46 tests, the evanescent waves boundary condition predicts no

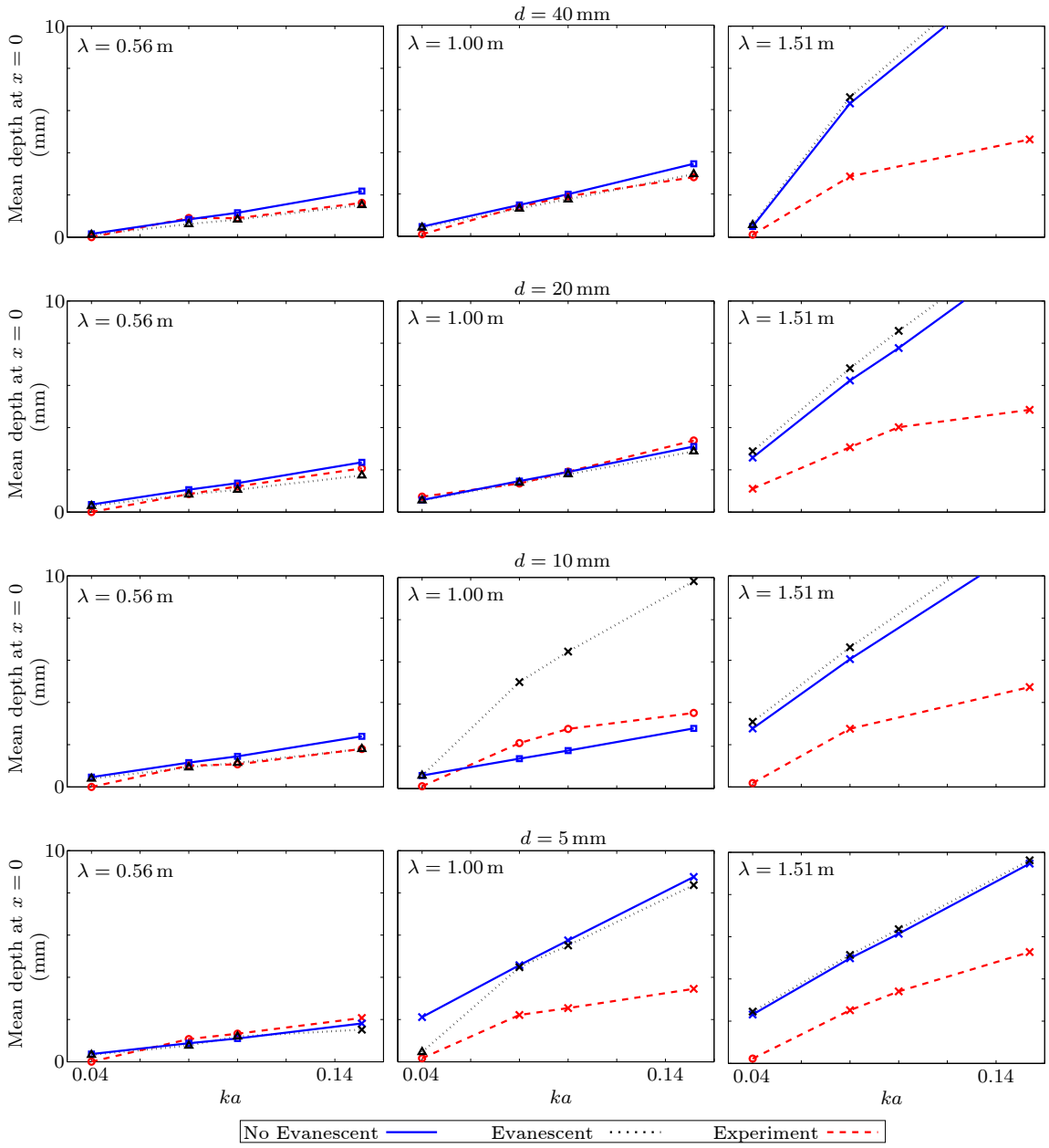

Figure 2.7: Plots of mean overwash depth at the centre of the PP plates subjected to all incident waves. From top to bottom plots vary in terms of decreasing plate thickness. From left to right plots vary in terms of increasing incident wave wavelength. Individual sub-plots show mean overwash depth at the plate's centre as a function of incident wave steepness. Experimental results are shown in dashed red, the no evanescent wave model in solid blue, and the evanescent wave model in dotted black. Where the respective model or experiment predict bore collisions the point marker on the curves is changed to a cross. Where markers in the mathematical models exceed the upper limit of the y axis, the large difference between model and experiment implies the point's location need not be shown.

bore collisions occur in 26 of the 46 tests, and the experiments have no bore collisions in 31 of the 46 tests. Whenever the respective model predicts no bore collisions the experiments do not have bore collisions either. Therefore, the models predict the occurrence of no bore collisions well, and the no-evanescent wave boundary conditions give slightly better predictions of these occurrences. The principle reason the no-evanescent wave boundary conditions predict fewer bore collisions (as is particularly evident in the $d = 10\,\text{mm}$ and $\lambda = 1.00\,\text{m}$ panel) is because the evanescent wave boundary conditions generally make the water deeper and propagate faster in the negative x-direction at the plate's downstream edge.

Across all the cases where the no-evanescent wave model does not predict bore collisions the mean depth is 1.38 mm for the model and 1.30 mm for the experiments. In these cases, the average absolute difference between model and experiment is 0.34 mm, the minimum difference is $< 0.03\,\text{mm}$, and the maximum difference is 1.0 mm. For 25% of these cases the absolute difference is $< 0.16\,\text{mm}$, for 50% of these cases the difference is $< 0.26\,\text{mm}$, for 75% of these cases the difference is $< 0.47\,\text{mm}$, and for 90% of these cases the difference is $< 0.66\,\text{mm}$. Therefore, if the no-evanescent wave model predicts no bore collisions, it compares favourably with experiments. For the cases where the evanescent wave model does not predict bore collisions, the average mean depth is 1.07 mm of for the model and 1.08 mm for the experiments. In these cases, the average absolute difference between model and experiment is 0.21 mm, the minimum difference is $< 0.03\,\text{mm}$, and the maximum difference is 0.51 mm. For 25% of these cases the absolute difference is $< 0.10\,\text{mm}$, for 50% of these cases the difference is $< 0.17\,\text{mm}$, for 75% of these cases the difference is $< 0.33\,\text{mm}$, and for 90% of these cases the difference is $< 0.44\,\text{mm}$. Hence, if the evanescent wave model predicts no bore collisions, it also compares favourably with experiments, and the agreement is generally better than for the no-evanescent wave model.

When the models predict bore collisions the mean depth at the plate's centre is markedly different. For the cases when the no-evanescent wave model predicts bore collisions, its the average depth at the plate's centre is 6.67 mm, whereas the experiments average depth at the plate's centre is 2.78 mm. For 95% of these cases the absolute difference is $> 7.6\,\text{mm}$, and for 50% of these cases the error is $> 3.2\,\text{mm}$. Only a single case shows favourable agreement, which is when $d = 5\,\text{mm}$, $\lambda = 0.56\,\text{m}$, and $ka = 0.15$, for which the

difference is 0.26 mm. Hence, although the no-evanescent wave boundary conditions model predicts the occurrence of bore collisions well, it produces considerably more water on the plate when they occur. For the cases when the evanescent wave model predicts bore collisions, the average depth at the plate's centre is 6.95 mm for the model and 2.92 mm for the experiments. For 95% of these cases the absolute difference is > 8.3 mm and for 50% of these cases the absolute difference is > 3.7 mm. Similar to the other model, the only case with favourable agreement is $d = 5$ mm, $\lambda = 0.56$ m, and $ka = 0.15$, for which the difference is 0.56 mm. Thus, as with the no-evanescent wave boundary conditions, when bore collisions occur the evanescent wave model predicts markedly more water on the plate.

The plots also show that bore collisions are more likely to occur as λ or ka increases, or as d decreases. Thus, in general, the agreement between models and experiment is favourable for all $\lambda = 0.56$ m, favourable for half the cases with $\lambda = 1.00$ m, and unfavourable for $\lambda = 1.51$ m. This trend is evident when considering the row of plots for $d = 20$ mm. In this row, for $\lambda = 0.56$ and 1.00 m the difference between models and experiment is always within 0.3 mm, and on average the difference is ~ 0.18 mm. In contrast, for $d = 20$ mm and $\lambda = 1.51$ m, the difference is always greater than 1.5 mm, and the difference between models and experiment is ~ 3.8 mm on average. This implies that the model is good for predicting the overwash for lower incident wave steepnesses and wavelengths, and generally better for the thicker plates.

Results as in figure 2.7, but for the PVC plate, are shown in Appendix C. They are similar to the results of the PP plate in all aspects, however, the overwash is shallower for an equivalent λ, ka, or d, and bore collisions are less likely occur. Both of these differences between PP and PVC occur because the PVC plate is less dense, and therefore the waves must be larger to exceed the freeboard of the plates' edges. Ultimately, the figure in Appendix C again demonstrates that agreement between model and experiments is favourable when bore collisions do not occur, weak when they do, and agreement is better for lower λ or ka, or larger d.

These results imply that the primary issue with the overwash model is its inability to model a bore collisions. To elaborate on why this happens, figure 2.8 shows a representative schematic of a bore collision event as predicted by the shallow-water equations.

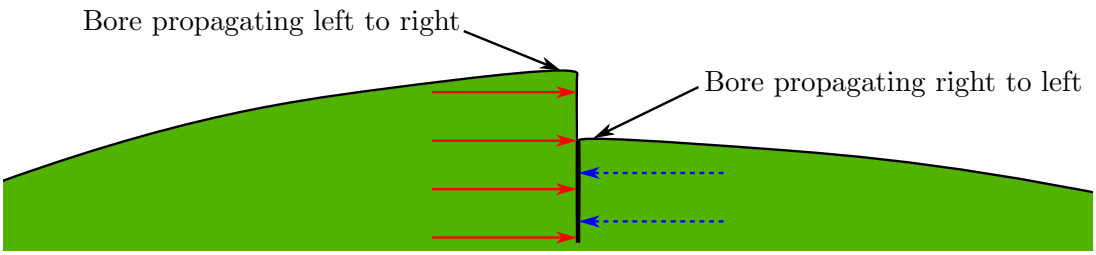

Figure 2.8: Representative schematic of shallow-water bore collision.

The solid red arrows in this figure represent that the leftmost bore is travelling from left to right and and the dashed blue arrows represent that the rightmost bore is travelling from right to left. As these bores intersect, the portion of the leftmost bore that exceeds the height of the rightmost bore has a much greater velocity than the velocity of the bore it collides with. Therefore, the horizontal velocity changes significantly about its depth. This is in direct violation of the shallow-water assumption — that the changes in horizontal velocity about the water's depth is negligible (as in equation 2.21). Hence, the breakdown of the model when bore collisions occur can be attributed to the invalidity of the shallow-water assumption in a bore collision event.

Significant disagreements between model and experiments could also be present at the edges of the plate where the water transitions from deep water waves to shallow-water flow. The visuals of the experiments show that the water there is characterised by strong breaking effects, which is not captured in full by the shallow-water equations. This source of error cannot be discussed more directly in this chapter due to the lack of experimental data around the plate's edges. It will, however, be investigated further when the problem of an overwashed step is considered in chapter 3.

2.5 Summary

Overwash experiments were conducted wherein thin and long PP and PVC plates were subjected to monochromatic water waves of a range of steepnesses and wavelengths. As expected, the overwash was found to be more likely to occur, deeper, faster, and more energetic as the length of the incident waves increased, as the steepness of the incident wave's increased, or as the plate's thickness decreased. As overwash was formed it was

characterised by waves breaking over the edges of the plate, which would then produce shallow-water bores. For incident waves of relatively short lengths or low steepnesses, the overwash would form at the upstream edge only. For steeper or longer waves bores would also be generated from the downstream edge and would collide with bores produced at the upstream edge. This collision was characterised by turbulence, breaking, and the production of choppy water.

A theoretical model of overwash of a thin floating plate by regular monochromatic incident waves was presented to model this interaction. The model uses linear potential theory to model the motion the plate and surrounding water waves, and uses the nonlinear shallow-water equations to model overwash. Its principle assumption is that the overwash can be forced without consideration of how it perturbs the wave/plate motion predicted by linear potential theory. Two sets of boundary conditions were considered for this model. The first included the evanescent waves around the plate, and the second excluded the evanescent waves around the plate. Neither set of boundary conditions were found to give superior overwash predictions.

When compared to the experiments the model was shown to predict qualitative and quantitative overwash properties accurately when bores formed at the upstream edge of the plate. This generally occurs for incident waves with relatively short lengths or low steepnesses. It implies that, in this regime, the linear potential flow/thin-plate model accurately predicts overwash forcing, and the nonlinear shallow water equations accurately model the overwash. The model was also shown to overpredict the overwash depth when the incident wave becomes longer or steeper, or plate thickness decreases. This was shown to coincide with the experimental regime in which large turbulent bores are generated the plates' upstream and downstream ends, which produce turbulence, breaking, and choppy water when they collide. The breakdown of the mathematical models when bore collisions occur can be attributed to bore collisions being incompatible with the underlying assumptions of the shallow-water equations. This chapter therefore demonstrates that unless the overwash contains bore collisions the overwash can be modelled using the nonlinear shallow-water equations without considering how it perturbs the surrounding waves. However, if bore collisions do occur, a more sophisticated model of the water on the plate is required.

Chapter 3

Overwash of a step

3.1 Introduction

To provide better insights into the overwash phenomena and the applicability of the model presented in chapter 2 a much simpler case of overwash is investigated — overwash of a step. This case of overwash is where waves approach a step with a sheer vertical wall and a horizontal upper surface aligned with the equilibrium free surface of the water.

Investigating overwash of a step provides multiple benefits when compared to the floating plate case. Firstly, the removal of floating plate dynamics allow a number of modelling approximations to be removed from the mathematical model, which therefore allows more direct investigation of how overwash develops. Secondly, the removal of the floating plate dynamics allows a CFD model to be built more easily. In turn, a CFD model can provide more data than can be obtained experimentally, such as mass and energy fluxes in the overwash. Thirdly, without having to consider bore collisions and plate dynamics, it is easier to develop a model of how the overwash affects the surrounding wave field.

In this chapter a two dimensional CFD model of overwash of a step is presented. The CFD model uses the two phase Navier Stokes equations to describe the air and water in a virtual wave tank. The equations are solved using the open-source CFD software OpenFOAM using the volume of fluid method (Hirt & Nichols, 1981; Weller *et al.*, 1998). The CFD model is two dimensional and does not include turbulence or surface tension.

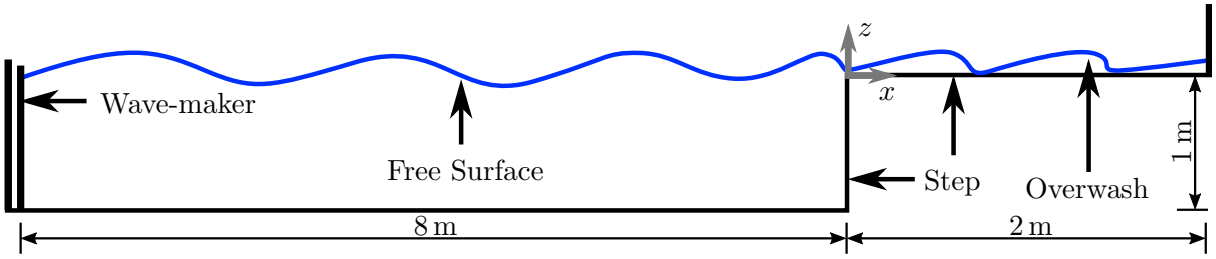

Figure 3.1: Schematic of problem (not to scale).

Turbulence is not included in this model because the green water CFD models of Greco *et al.* (2005), Greco *et al.* (2007), Nielsen & Mayer (2004), and Buchner (2002) where able to accurately model the cognate phenomena of green water (for which the Reynolds number is approximately 1 or 2 orders of magnitude greater than found in overwash in this investigation) without using turbulence modelling. Surface tension is assumed to be negligible for similar reasons.

Using the same principles as in chapter 2, a mathematical model of overwash of a step is developed. The model uses the nonlinear shallow-water equations to model the overwash and linear potential flow theory to model the waves to the side of the step. The model is once again built on the key modelling assumption that the overwash can be forced without considering how it perturbs the surrounding water.

The objectives of this chapter are to:

1. Present and analyse the CFD model of overwash of a step.
2. Develop a simplified mathematical model of overwash of a step using similar modelling principles as in chapter 2.
3. Analyse the merits of the mathematical model with respect to the data obtained from the CFD model.

3.2 CFD Model

3.2.1 CFD model description

Consider a two-dimensional rectangular wave basin with depth $H = 1\,\mathrm{m}$ and length $8\,\mathrm{m}$. A wave-maker bounds the left-hand end of the basin and the vertical, front, surface of

a rectangular step bounds its right hand end. The step's upper surface has length 2 m and at its rightmost end it meets a vertical wall extending upwards 2 m. A schematic of the basin is presented in figure 3.1. Locations are defined using the Cartesian coordinate system (x,z) where the origin is placed at the upper vertex of the step. The horizontal coordinate, x, points along the upper surface of the step, and the vertical coordinate, z, points upwards.

The basin is filled with water such that its undisturbed free surface is collinear with the upper surface of the step (i.e. along the line $z = 0$). Air occupies the space not filled with water. At the time $t = 0$, a virtual wave-maker begins generating a regular fifth-order Stokes incident wave, with specified amplitude, a, and angular frequency, ω, using the OpenFOAM library wave2Foam presented in Jacobsen *et al.* (2012). The incident waves force water to overwash the step, which travels for 2 m along the step until it is meets the vertical wall.

The wave, overwash, and surrounding air motions are modelled using the two-phase incompressible Navier Stokes equations. These are

$$\nabla \cdot \mathbf{u} = 0, \tag{3.1a}$$

$$\partial_t(\gamma) + \nabla \cdot (\mathbf{u}\gamma) = 0, \tag{3.1b}$$

$$\text{and} \quad \partial_t(\rho_c \mathbf{u}) + \nabla \cdot (\rho_c \mathbf{u})\mathbf{u}^T = -\nabla p + \nabla \cdot \mathbf{T} + \rho_c \mathbf{f}_b, \tag{3.1c}$$

where ρ_c is the density of the combined phases, and $\gamma(x, z, t) \in [0.1]$ is the phase fraction at the location and time, with $\gamma = 1$ denoting pure water, $\gamma = 0$ denoting pure air, and $0 < \gamma < 1$ denoting a linearly weighted mixture of water and air. The velocity field (for the air and water) is $\mathbf{u} = (u(x, z, t), w(x, z, t))^T$, $\mathbf{T}(x, z, t)$ is the viscous stress tensor, and $\mathbf{f_b} = (0, -g)$ is the external forcing due to gravity. As in chapter 2, u is the horizontal velocity of the fluid, w is the vertical velocity of the fluid, and $g = 9.81\,\mathrm{m\,s^{-2}}$ is the acceleration due to gravity.

In this description equation 3.1a represents conservation of mass of the combined phases (air and water), equation 3.1b represents conversation of mass of the individual phases, and equation 3.1b represents the conversation of momentum. Equation 3.1c models vorticity via the deviatoric viscous stress tensor for an incompressible Newtonian

fluid

$$\mathbf{T} = \mu_c \left[\nabla \mathbf{u} + (\nabla \mathbf{u})^T \right], \tag{3.2}$$

where μ_c is the dynamics viscosity of the combined phases. It is this term that causes mechanical energy to be dissipated into heat due to internal viscous forces (Batchelor, 2000).

The water and air are modelled as incompressible. This implies that the CFD simulation does not model the collapse of air cavities into bubbles in full; a challenging task for numerical solvers (Greco *et al.*, 2007). This simplification is made because Nielsen & Mayer (2004) and Buchner (2002) were able to model green water using a similar method without including compressible air dynamics. The density and viscosity of a fluid volume are therefore modelled as the weighted arithmetic average of the air and water components. Thus, the density and viscosity are given by $\rho_c = \rho_w \gamma + \rho_a(1-\gamma)$, and $\mu_c = \mu_w \gamma + \mu_a(1-\gamma)$, respectively, where subscripts denote (c) the combined phase mixture, (w) the water, and (a) the air. The material constants are set to their respective values at atmospheric pressure and 20° C: $\rho_w = 1000\,\mathrm{kg\,m^{-3}}$, $\rho_a = 1.225\,\mathrm{kg\,m^{-3}}$, $\mu_w = 1.002 \times 10^{-3}\,\mathrm{N\,s\,m^{-2}}$ and $\mu_a = 18.37 \times 10^{-6}\,\mathrm{N\,s\,m^{-2}}$ (Mills, 1999).

The CFD model is solved using a customized version of the interFoam solver from the OpenFOAM open source CFD library (Berberović *et al.*, 2009; Paulsen *et al.*, 2014), which is based on the volume of fluid method (Hirt & Nichols, 1981). The solver is applied on an unstructured mesh, using rectangular volumes of varying dimensions. Data analysis of the mesh was performed to optimise the run-time and produce convergence for the overwash between $0 < x < 0.5\,\mathrm{m}$ (this analysis was lengthy and therefore is not shown). In and around the initial overwash region, $-0.1\,\mathrm{m} \leq x \leq 0.55\,\mathrm{m}$ and $-0.04\,\mathrm{m} \leq z \leq 0.04\,\mathrm{m}$, relatively small mesh volumes with lengths and widths of 0.2 mm were used. These relatively small mesh sizes were needed in order to capture breaking effects without introducing artificial noise and energy dissipation from the numerical solver. For $x > 0.55\,\mathrm{m}$ the horizontal length of the mesh volumes linearly decrease to 100 mm at $x = 2\,\mathrm{m}$ (the location of the vertical wall), in order to dissipate overwash energy numerically, which was tested and implemented to dissipate all reflection effects from the vertical wall at $x = 2\,\mathrm{m}$. For $x < -0.1\,\mathrm{m}$ the mesh sizes linearly decrease towards the wave-maker, where volumes are ~ 1000 times larger than in the high resolution region.

The mesh provides convergence with respect to the mean overwash depth, depth averaged velocity, mass flux, and energy flux over a wave period in the interval $0 < x < 0.5\,\mathrm{m}$ (the region that will be analysed in this chapter). Moreover, the mesh to the left of the step is such that it dissipates less than 2% of the incident wave energy when they propagates 8 m.

Simulations were run up to $t = 30\,\mathrm{s}$, allowing the overwash to reach and maintain periodic motion. Each simulation took $\sim 120\,\mathrm{h}$ to run on a 96 core cluster. Three angular frequencies were tested, with corresponding wave periods $T = 0.6$, 0.8, and 1.0 s, where $T = 2\pi\omega^{-1}$. For each frequency wave amplitudes were tested in the steepness range $0.03 \leq ka \leq 0.13$ (well below the breaking limit, Babanin *et al.*, 2007) where k is the positive root to the dispersion relation $k\tanh(kh) = \omega^2 g^{-1}$. The steepnesses and periods were chosen to be similar to those used in the floating plate experiments in chapter 2.

Two different boundary conditions were tested on the horizontal and vertical faces of the step: (i) the no-slip condition $\mathbf{u} = \mathbf{0}$, and (ii) the no-shear condition $\mathbf{u} \cdot \mathbf{n} = 0$ and $\partial_{\mathbf{n}}\mathbf{u}_t = 0$, where the vector $\mathbf{n}$ is a unit vector normal to the surface, and $\mathbf{u}_t$ is the tangential velocity at the boundary. The no-shear condition was used as it is consistent with the shallow-water equations. The no-slip condition was used to investigate the effects of a boundary layer in the overwash. No-slip conditions were applied to the remaining boundaries of the basin.

3.2.2 CFD model qualitative analysis

The overwash becomes deeper, faster, and breaking effects become more prominent as the incident wave amplitude increases. In comparison, these properties were found to be relatively insensitive with respect to incident wave period for the tested periods of $T = 0.6$, 0.8, and 1.0 s for an equivalent steepness. The only major impact varying incident wave period had was changing the periodicity of the overwash, which was found to cycle with the same period as the incident wave, and the time taken for the overwash to become periodic, which generally took place after ~ 5 incident wave peaks hit the edge of the step. Results, therefore, are presented for the incident $T = 0.8\,\mathrm{s}$ only, with corresponding incident amplitudes $a = 5$, 10, 15 and 20 mm. They are sampled in the intervals where

the overwash was periodic, and are representative of all tests.

Figure 3.2 shows snapshots of the phase fraction, γ, for the test with the largest incident wave amplitude, $a = 20\,\text{mm}$, i.e. the deepest overwash, and using the no-shear boundary condition (similar behaviours occur for no-slip conditions). Figure 3.2(a) shows an instant during a simulation when the incident wave forces overwash, with the box highlighting the interfacial region where a mass of water flows onto the step. As the incident wave hits the step the water above the step travels forwards, and the water just below the top of the step is pushed upwards, such that the top of the wave collapses onto the step. This creates wave overturning, similar to plunging breaker, just onto the step (as in Greco *et al.*, 2005), and the overturning creates water separation. Presumably, the separation is exaggerated by the neglect of surface tension, although the separated water is indistinguishable from the water bulk at a 1:1 axes scale (not shown). The roughness of the free surface in the interfacial region indicates prevalent wave breaking effects. These findings are qualitatively similar to those of Greco (2001) and Greco *et al.* (2005, 2007) from an experimental model of green water washing onto a ship deck, as described in section 1.4.

Figure 3.2(b) shows a snapshot $T/2 = 0.4\,\text{s}$ later, when the overwashed water packet has travelled $\sim 0.30\,\text{m}$ along the step. The box highlights breaking around the bore-front formed in the overwash (as per chapter 2, the bore-front is the location of the sharp change in depth). The water at the bore-front is approximately 4 times deeper and 3.5 times faster than the water just ahead of it. The sharp increase in steepness at the bore-front causes the water near the upper surface to continually overturn the water below, creating the breaking, entrained air pockets, water separation, and ripples seen around the bore. Breaking effects are largely confined to $0.2\,\text{m}$ behind the bore-front, and, although entrained air pockets are still present outside this region, they are not as numerous or large as those near the bore-front. The snapshot also shows water running off the step at $x = 0$. Its depth there is small relative to the overwash depth farther along the step and the depth of the water being forced onto the step $0.4\,\text{s}$ earlier (figure 3.2a). This indicates that the run-off volume is minor with respect to the volume of water washing onto the step.

Figure 3.3 shows signals of the overwash depth and depth averaged velocity produced

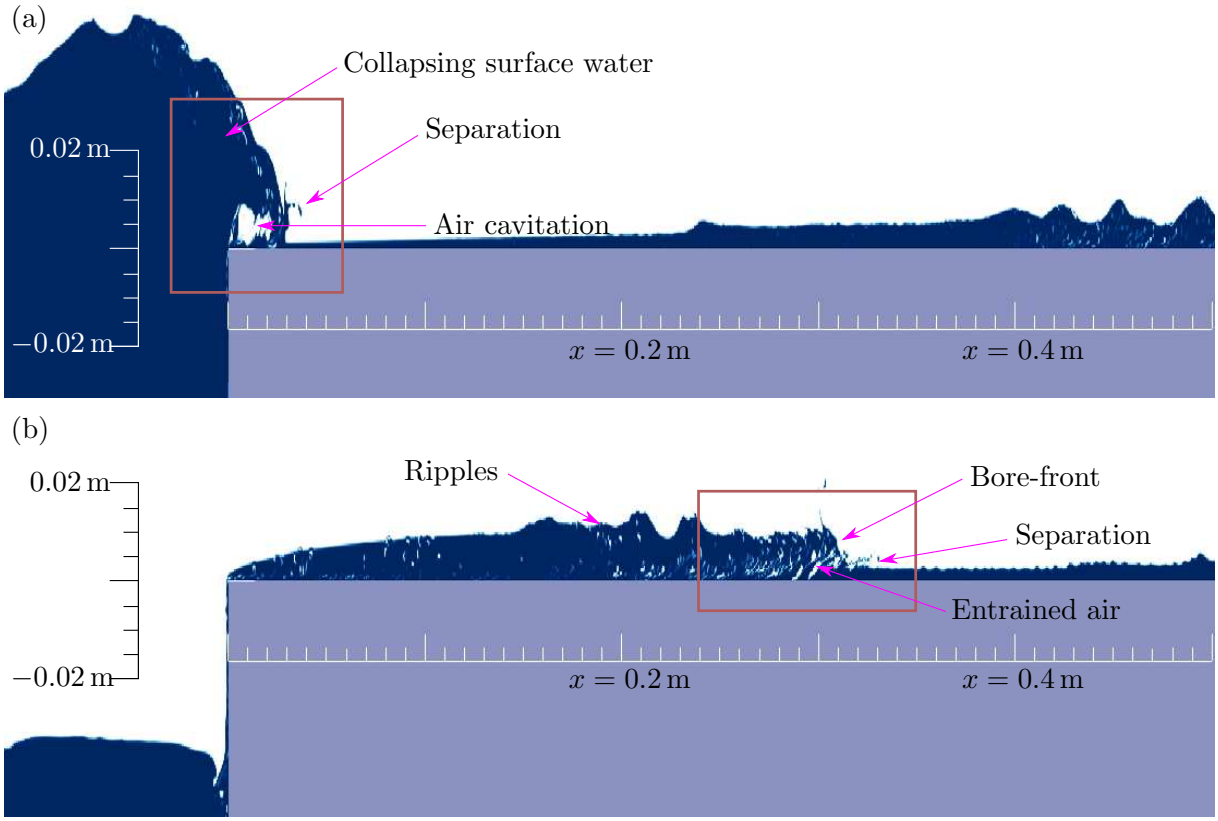

Figure 3.2: Snapshots of phase fraction produced by the CFD model with no-shear boundary conditions, produced by incident amplitude $a = 20\,\text{mm}$, for: (a) an instant at which an incident wave forces a packet of water onto the step; and (b) an instant 0.4 s later, when a bore has formed in the overwash. Pure water ($\gamma = 1$) is solid blue, pure air ($\gamma = 0$) is solid white, and the step is grey. The scale of the z-axis is larger than the x-axis scale by a factor 4 to emphasise overwash effects, and red boxes highlight regions of greatest interest at the corresponding instants.

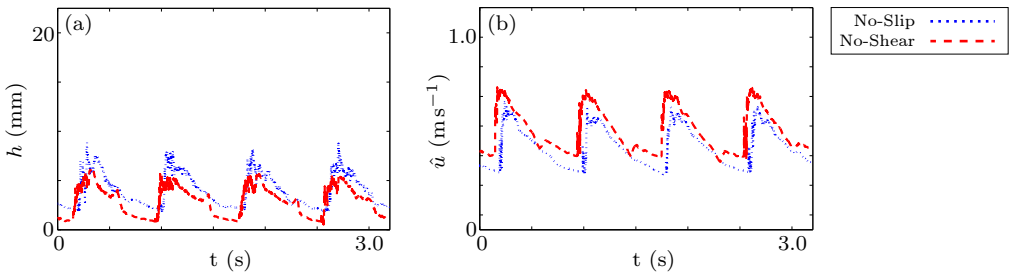

Figure 3.3: CFD model predictions of overwash (a) depth and (b) depth averaged horizontal velocity, as functions of time, at $x = 0.2\,\text{m}$ for incident wave amplitude $a = 15\,\text{mm}$, produced by no-shear (red dashed line) and no-slip (blue dotted) boundary conditions.

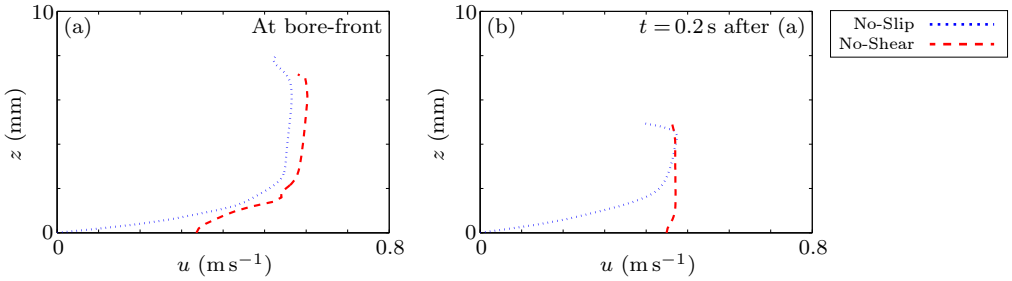

Figure 3.4: CFD model predictions of horizontal velocity, u, as a function of height, z, across the overwash depth at $x = 0.2\,\mathrm{m}$, for instants at which (a) a bore-front is at the location, and (b) bore-fronts are away from the location. As in figure 3.3, results are for incident wave amplitude $a = 15\,\mathrm{mm}$, and produced by no-shear (red dashed line) and no-slip (blue dotted) boundary conditions.

by the no-shear and no-slip models for the simulation with incident wave amplitude $a = 15\,\mathrm{mm}$. In the CFD model the depth and depth averaged velocity are defined as

$$h = \int_0^\infty \gamma \,\mathrm{d}z \quad \text{and} \quad \hat{u} = \frac{1}{h}\int_0^\infty \gamma u \,\mathrm{d}z, \quad \text{respectively.} \tag{3.3}$$

The signals are sampled at $x = 0.2\,\mathrm{m}$, by which point the breaking over the edge as seen in figure 3.2(a) has developed into bores like those seen in figure 3.2(b). The plots show the presence of bores-fronts at the sharp peaks seen in the signals. The signals themselves are similar to those found in the experiments of chapter 2 for the depth at the centre of the plate, although with more roughness, presumably due to the non-invasive probing or the neglect of surface tension. They are also similar to those found in the green water study of Buchner (2002) and Greco *et al.* (2007). The plots also show that the no-slip and no-shear boundary conditions produce similar signals shapes, however, the no-slip model consistently predicts deeper and slower overwash than the no-shear model. Further, the no-shear model peaks occur slightly before the peaks of the no-slip model, which is because the no-shear bores are propagating faster. The systematic difference in depth and velocity, despite the vertical offsets, are indicative of a boundary layer.

Figure 3.4 shows the vertical velocity profiles of the no-slip and no-shear models at $x = 0.2\,\mathrm{m}$ for the same incident wave as in figure 3.3. Figure 3.4(a) shows an instant when the bore-front is present at $x = 0.2\,\mathrm{m}$, and figure 3.4(b) is taken $0.2\,\mathrm{s}$ later, when the water is approximately at its mean (time averaged over a wave period) depth level.

At the bore-front, both models predict the water is faster at the surface than at the bed, symbolic of the overturning that occurs around the bore-fronts. Nonetheless, the no-shear model's velocity profile is much more uniform than the no-slip model, which rapidly tapers to $u = 0$ for $0 < z < 2\,\text{mm}$. Away from the bore-front, the no-shear model predicts the velocity is near uniform, whereas the no-slip model predicts it is uniform for $z > 2\,\text{mm}$ and rapidly tapers to zero for $z < 2\,\text{mm}$. This implies the no-slip boundary condition produces a boundary layer that is approximately 2 mm deep (Schlichting & Gersten, 2016). A boundary layer like that shown in figure 3.4 was found to occur for all waves tested and always be approximately 2 mm deep for $x > 0.1\,\text{m}$ (once bores had formed). Hence, it is more pronounced for smaller amplitude incident waves, and at locations farther along the step.

3.3 Mathematical model

The mathematical model's geometry is as in section 3.2.1 but instead of having the vertical wall 2 m downstream from the step's edge and wave-maker at $x = -8\,\text{m}$, the domain stretches outwards indefinitely as x approaches positive and negative infinity. Similar to the model in section 2.3, the water domain is split into two subdomains:

(i) the wave basin domain containing relatively deep water ($x < 0$); and

(ii) the overwash domain containing shallow-water ($x > 0$).

As in section 3.2.1, the water in each subdomain is assumed to be irrotational, incompressible, and inviscid.

The water in domain i is modelled using the assumptions in section 2.3.1 but without the plate and with no penetration condition at the wall. Its velocity potential, $\phi(x, z, t)$, therefore satisfies Laplace's equation, no penetration conditions as the basin edge/step

wall, and the linearised free surface condition. These are

$$\nabla^2\phi = 0 \qquad \text{for} \quad -H < z < 0 \quad \text{and } x < 0, \tag{3.4a}$$

$$\partial_z\phi = 0 \qquad \text{on} \quad z = -H \quad \text{and } x < 0, \tag{3.4b}$$

$$\partial_x\phi = 0 \qquad \text{on} \quad x = 0 \quad \text{and } -H < z < 0, \quad \text{and} \tag{3.4c}$$

$$\partial_z\phi + g^{-1}\partial_t^2\phi = 0 \qquad \text{on} \quad z = 0 \quad \text{for } x < 0, \tag{3.4d}$$

respectively (Mei *et al.*, 1989), where the velocity of the water is given by $(u, w) = (\partial_x\phi, \partial_z\phi)$.

As in chapter 2, the incident waves propagates in the positive x-direction and are harmonic at the frequency ω. Thus, the incident wave potential is given as

$$\phi_I = -\frac{ag}{\omega}\sin(\omega t - kx)\frac{\cosh(k(z+H))}{\cosh(kH)} \tag{3.5}$$

where k is the positive real root to the dispersion relation

$$k\tanh(kH) = \omega^2 g^{-1}. \tag{3.6}$$

As waves radiate freely out towards $x \to -\infty$ the potential also satisfies the Sommerfeld radiation condition

$$\partial_x(\phi - \phi_I) - \mathrm{i}k(\phi - \phi_I) \to 0 \quad \text{as } x \to -\infty. \tag{3.7}$$

Solved as a boundary value problem equations 3.4-3.7 give

$$\phi = \phi_I(x, z, t) + \phi_I(-x, z, t) = -\frac{2ag}{\omega}\sin(\omega t)\cos(kx). \tag{3.8}$$

This implies that the waves to the left of the step create a standing wave field because of the no penetration condition on $-H < z < 0$ for $x = 0$, which itself implies that the wall reflects all of the wave energy incident upon it. Linear potential flow theory gives the free surface of this standing wave field for $x < 0$ as

$$\eta(x, t) = -\frac{1}{g}\partial_t\phi(x, 0, t) = 2a\cos(\omega t)\cos(kx), \tag{3.9}$$

and the x-directional velocity along $z = 0$ as

$$u(x, z = 0, t) = \partial_x\phi(x, z = 0, t) = 2agk\omega^{-1}\sin(\omega t)\sin(kx). \tag{3.10}$$

The water in domain ii is modelled under the assumptions as in section 2.3.2 but with the upper surface of the plate replaced with the fixed upper surface of the step. Hence, it is assumed that for $x > 0$ the water's flow properties along the horizontal characteristic length scale, C_x, are much greater than their properties in the characteristic vertical length scale, C_z. As discussed section 2.3.2, this implies that the vertical velocity is negligible when compared to the horizontal length scale and that the horizontal velocity is approximately constant along the water's depth. Therefore, for $x > 0$, the water it is modelled using the nonlinear shallow-water equations

$$\partial_t (h) + \partial_x (h\hat{u}) = 0 \qquad \text{and} \tag{3.11a}$$

$$\partial_t (h\hat{u}) + \partial_x \left(\frac{1}{2} g h^2 + h\hat{u}^2 \right) = 0, \tag{3.11b}$$

where $h(x,t) = \eta$ is the depth of the water above the step, $\eta(x,t)$ is the water's free surface height, and $\hat{u}(x,t)$ is the depth averaged horizontal velocity (Tan, 1992).

As in chapter 2 it is assumed that the overwash can be accurately forced without considering how it affects the waves to the left of the step. Hence, at the interface with domain i (i.e. at $x = z = 0$), if the wave's free surface is above the step, the depth and velocity of the overwash are set to match the depth and velocity of the waves, or be zero otherwise. Thus,

$$h(x = 0^-, t) = \max\left(\eta(x = 0^-, t), 0\right) = \max\left(2a\sin(\omega t), 0\right), \quad \text{and} \tag{3.12a}$$

$$\hat{u}(x = 0^-, t) = u(x = 0^-, z = 0, t) = 0, \tag{3.12b}$$

as $u(x = 0^-, z = 0, t) = 0$ for all t.

In the characteristic plane, boundary conditions 3.12 produce characteristics $X_+(x,t)$ that emanate from $x = 0$ for $t > 0$ and enter domain ii. The associated slope of these characteristics are $\mathrm{d}X_+/\,\mathrm{d}t = \hat{u} + \sqrt{gh}$ with Riemann invariant $R_+ = \hat{u} + 2\sqrt{gh}$. For times when $\eta(0^-, t) = 0$, the slope of these characteristics are zero and therefore the boundary conditions do not force characteristics into the domain. Hence, for these time intervals the water's motion at $x = 0^+$ is not influenced by the water to the left of the step and can run-off freely. For times when $\eta(0^-, t) > 0$ the slope of the characteristic is positive, implying the X_+ characteristic enters the domain with Riemann invariant $R_+ = \hat{u} + 2\sqrt{gh}$. This allows water to form onto the step even though $\hat{u}(x = 0^-, t) = 0$

is specified. Furthermore, as was discussed in section 2.3.2, because the characteristics entering the domain do not depend on the values of $h(0^+,t)$ and $\hat{u}(0^+,t)$, they force a discontinuity in $\hat{u}$ and h over $x=0$ (Tan, 1992).

During the overwash generation phase with $\eta(0^-,t)$ increasing, these characteristics force the Froude number $Fr=\hat{u}/\sqrt{gh}$ immediately onto the step to pass through unity. This means the flow transitions from sub-critical to super-critical once per overwash generation phase. In the context of the shallow-water equations, this generates a travelling shock (Tan, 1992; Vreugdenhil, 1994), which creates a bore. The shocks themselves dissipate energy as they travel along the step (Billingham & King, 2000), which implies that energy is dissipated in the shallow-water model as the water flows along the step. Note that the same energy dissipation mechanism exists for the floating plate model of chapter 2.

As in section 2.3.2 the shallow-water problem 3.11-3.12 is solved numerically using the scheme shock-capturing method of Kurganov & Tadmor (2000) to discretise the spacial derivatives and the total variation diminishing second order Runge-Kutta method to discretise the time derivatives (Gottlieb & Shu, 1998). This method is presented in Appendix B. For this method, the values of h and $\hat{u}$ are spaced into M equally sized volumes of width Δx from $x=0$ to $x=R>0$. The boundary conditions 3.12 are prescribed at the ghost volume centred at $x=-\Delta x-0.5\Delta x$. As the shallow-water equations produce a discontinuity at $x=0$, the results for $x=0^+$ (i.e. immediately onto the step) are taken at the volume centred at $x=\Delta x+0.5\Delta x$ rather than at the volume centred at $x=0$. This is because, even though the method prescribes a value of $\hat{u}$ and h there, it is unphysical because of the discontinuity that occurs inside this volume. Numerical radiation conditions at the far end of the domain were prescribed such that $\hat{u}(R,t)=h(R,t)=0$ where $R=2\,\mathrm{m}$ (approximately 4 times the characteristic length of the bores). These were found to be sufficiently far from the analysed region ($0<x<0.5\,\mathrm{m}$), such that solutions were exactly equal when using the equivalent radiation conditions but with $R=10\,\mathrm{m}$. Convergence with respect to Δx was analysed. It was found that for $0.0001<a<0.1\,\mathrm{m}$, and for $\Delta x\approx 0.0033\sqrt{a}$, results for h and $\hat{u}$ converged to within 0.8% of their values when a more refined mesh of $0.01\Delta x$ was used. Therefore, results are presented for $\Delta x=0.25\,\mathrm{mm}\ll 0.0033\sqrt{a}$ for all a tested.

Simulations were run up to $t = 15\,\mathrm{s}$ (noting that the mathematical model does not require a time interval for waves to build-up and reach the step) using the same incident wave amplitude and period combinations as in the CFD model. As was found for the CFD simulations, periodic overwash motions were obtained after ~ 5 periods of the wave forcing. Each simulation required only $\sim 0.2\,\mathrm{h}$ to complete on a single core, which represents a $\sim$ 600-fold speed up in comparison to the CFD models (which were run on a 96 core cluster).

3.4 Mathematical model and CFD overwash comparisons

3.4.1 Overwash depth and depth averaged velocity comparisons

Figure 3.5 shows snapshots of the phase fraction produced by the no-shear CFD model as in figure 3.2 but for the mid-range amplitude $a = 15\,\mathrm{mm}$ and with corresponding mathematical model predictions of the free surface overlaid (dashed green). Time offsets are applied such that the maximum wave elevation at $x = 0^-$ is aligned between the models. The comparisons shown are typical of all incident wave conditions tested.

As in figure 3.2(a), figure 3.5(a) shows a snapshot for an instant at which an incident wave forces a water mass onto the step. The mathematical model prediction of the free surface in the interfacial region is markedly different from the CFD model. It initially underpredicts the free surface in the interval where an air cavity is present in the CFD model, and subsequently overpredicts the free surface in the interval where the overturning free surface passes onto the step in the CFD model. Beyond this interfacial region, the mathematical model predicts a near identical free surface profile to the CFD model.

Figure 3.5(b) shows a snapshot 0.5 s later, at which point the water mass has propagated farther along the step. Both models predict a bore develops, and the locations of the bore-fronts are $< 15\,\mathrm{mm}$ apart after washing 350 mm downstream (noting that the exact location of the bore front is ill-defined in the CFD simulation because the jump in depth is not instantaneous as in the shallow-water model). Moreover, the bore heights, and more generally, the overwash depth profiles, display pleasing agreement (notwithstanding

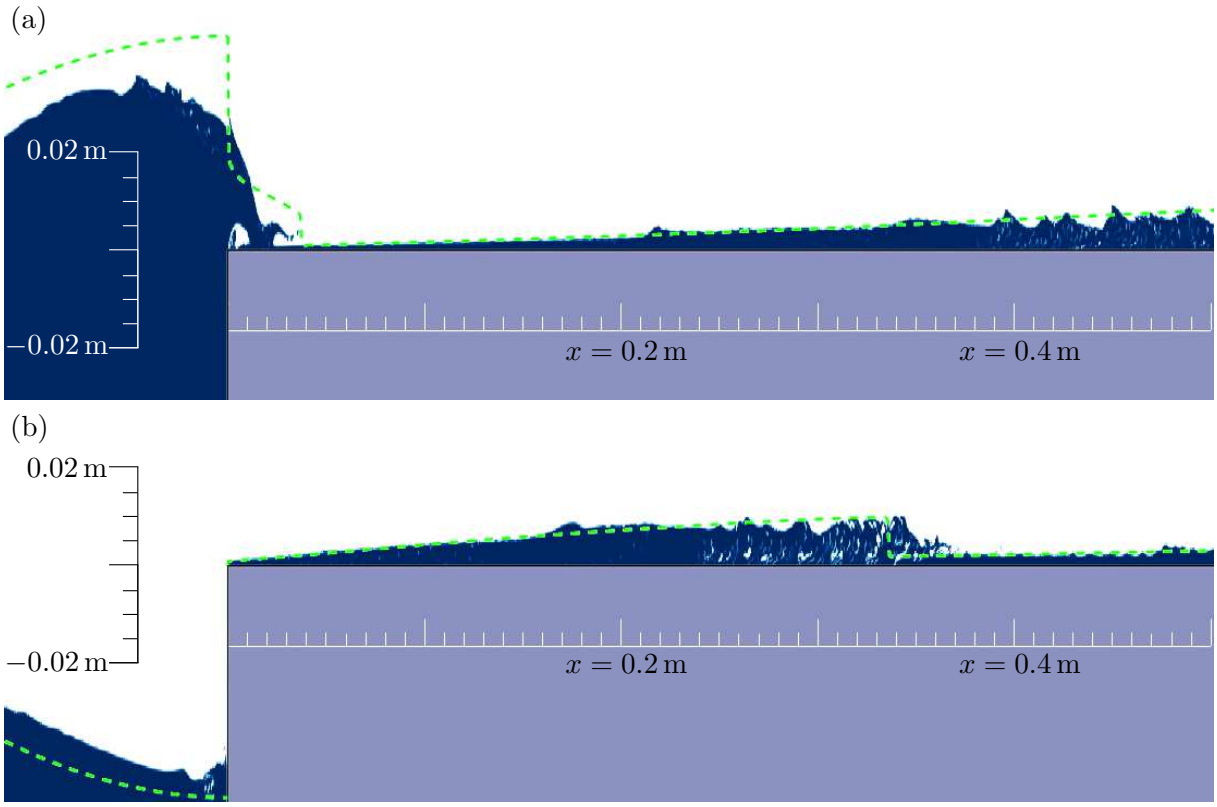

Figure 3.5: As in figure 3.2 but for $a = 15\,\mathrm{mm}$, with the mathematical model free surface overlaid (dashed Green), and the bottom visualisation is taken 0.5 s after the top visualisation.

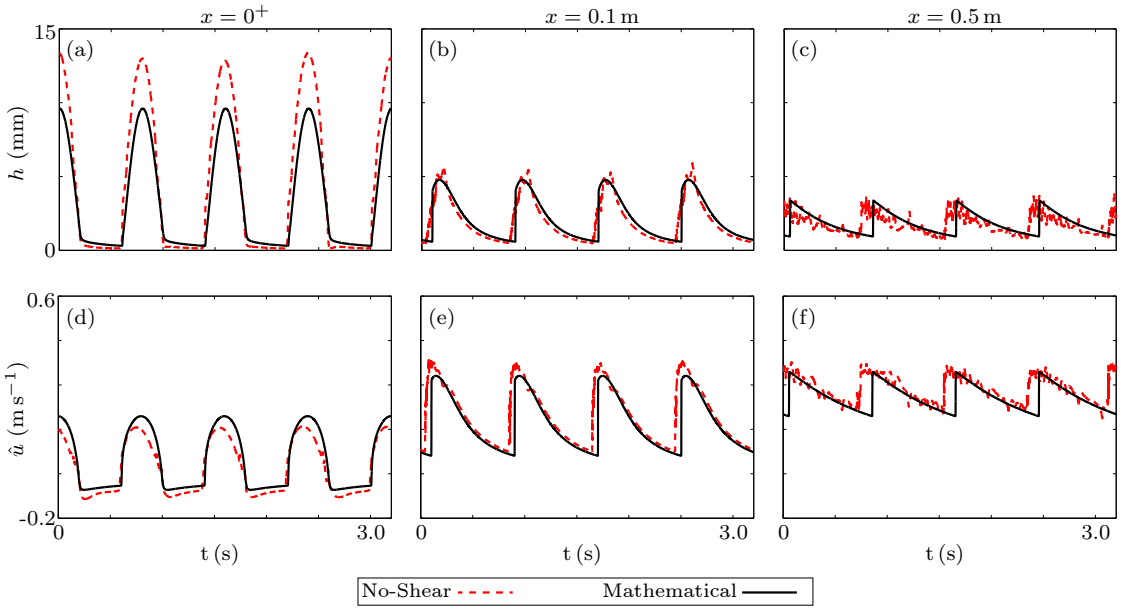

Figure 3.6: Depth versus time (top panels) and depth averaged velocity versus time (bottom) predictions given by mathematical model (solid black curves) and no-shear CFD model (broken red), for incident wave amplitude $a = 10\,\mathrm{mm}$, and sampled at $x = 0^+$ (left panels), 0.1 m (centre), and 0.5 m (right) along the step.

the breaking effects present around the bore in the CFD simulation), indicating the mathematical model accurately predicts the overwash beyond the interfacial region, despite neglecting air cavitations and wave breaking effects.

Figure 3.6 shows depth and depth averaged horizontal velocity signals, given by the mathematical model (solid black) and no-shear CFD model (dashed red), sampled at $x = 0^+$, 0.1 and 0.5 m. Results are provided for the incident wave amplitude $a = 10\,\mathrm{mm}$, which is representative of all incident waves tested. The first location, $x = 0^+$, compares the models at the interface between the basin and overwash. Note that in both models the $x = 0^+$ location is sampled at the first volume locations centred at $x > 0$. The depth signals (figure 3.6a) are composed of approximately symmetric peaks which correspond to the wave surface in the basin rising above the step. For half the wave period inbetween these peaks the signals show a depth of approximately zero, which is when the waves to the right of the step dip below the step. As indicated in figure 3.5(a), the mathematical model predicts smaller depth peaks than the no-shear CFD model, with $\sim 3\,\mathrm{mm}$ differences at

the peaks, (note that the depth integration in equation 3.3 eliminates the air cavity in the CFD model). The models predict similar velocity signals at the interface (figure 3.6b), although the mathematical model predicts slightly larger peaks and shallower troughs, and the CFD model predicts positively skewed peaks. The run-off phase (negative velocity) occurs for approximately half of the duration of the overwash cycle. During this phase, the mathematical models predicts similar depths and velocities, with the no-shear CFD model, which indicates that the models predict a similar amount of run-off.

The second location, $x = 0.1\,\mathrm{m}$, is where bores have just formed. As discussed with respect to figure 3.3, the bores manifest in the signals as sharp increases in depth and velocity. The models agree closely in terms of overall shape, phase, frequency, peaks, and troughs for the depth and velocity signals. For the depth signals, the most notable difference is due to coarseness around the bore peaks predicted by the CFD model. For the velocities, the signals given by the models have small phase differences of $\sim 0.05\,\mathrm{s}$, which is 6% of the wave period only, and the velocity predicted by the CFD model is consistently $0.04\,\mathrm{m\,s^{-1}}$ greater than predicted by the mathematical model.

The final location, $x = 0.5\,\mathrm{m}$, is a point at which the CFD model predicts air entrainment and breaking effects are prevalent in the bores (as indicated in figure 3.5b). The shapes of the depth and velocity signals are similar to the corresponding signals at $x = 0.1\,\mathrm{m}$, with bores still pronounced, but with reduced peaks for the depth and velocity signals. The ongoing breaking effects in the CFD simulations create a high degree of roughness in the corresponding signals. Overall agreement between the models remains strong, although the phase shift in the depth and velocity signals increases to 0.1 s. This phase difference is a symptom of the mathematical model predicting slightly slower bores than the CFD model.

Figure 3.7 shows mean values of overwash depth (top panels) and depth averaged velocity (bottom panels) over four wave periods, as a function of incident wave amplitude, and for the three locations used in figure 3.6 (i.e. $x = 0^+$, 0.1, and 0.5 m). Results are given for the mathematical model (solid black lines and circles), the CFD model with the no-shear boundary condition (dashed red lines and triangles), and the CFD model with the no-slip boundary condition (dotted blue lines and squares).

In all cases, the mean depth increases as the incident wave amplitude increases (as

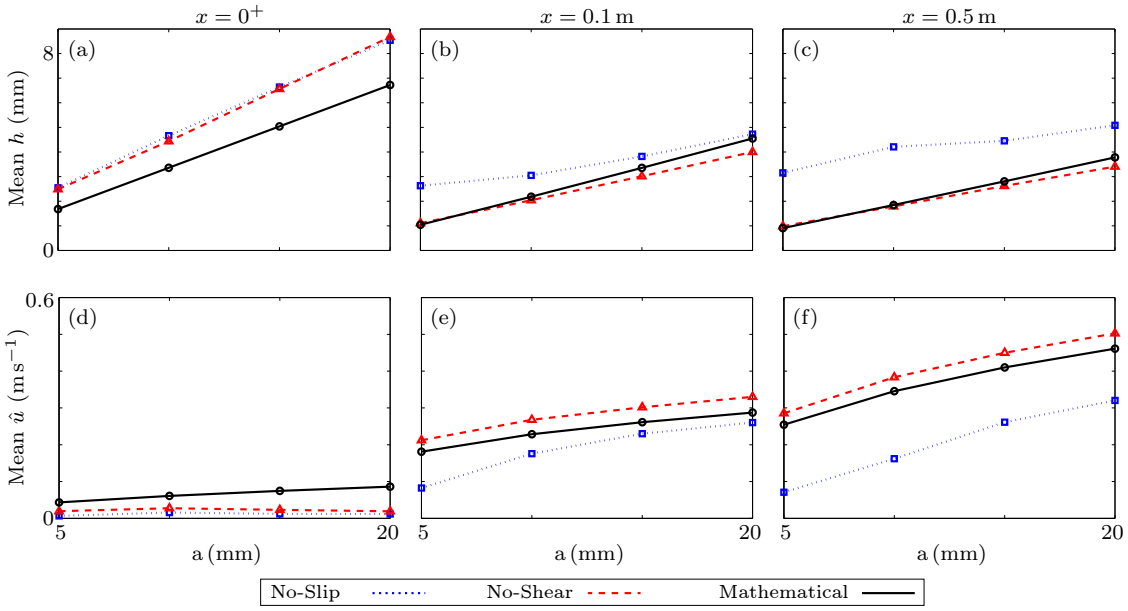

Figure 3.7: Mean depth versus amplitude (top panels) and mean depth averaged horizontal velocity versus amplitude (bottom), predicted by mathematical model (solid black curves and circles), no-shear CFD model (dashed red and triangles) and no-slip CFD model (dotted blue and squares), sampled at $x = 0^+$ (left panels), 0.1 m (centre), and 0.5 m (right) along the step.

expected) and generally decreases with distance along the step. The CFD models agree almost exactly at the basin–overwash interface ($x = 0^+$, figure 3.7a), indicating the boundary layer in the no-slip CFD model does not affect the overwash forcing. As shown in figures 3.5–3.6, at the interface the mathematical model is shallower than the CFD models, with the difference in depth increasing as wave amplitude increases. Despite their differences, both CFD and mathematical model find that the mean depth is proportional to the incident wave amplitude.

At the two points farther along the step, $x = 0.1\,\mathrm{m}$ and $x = 0.5\,\mathrm{m}$ (figures 3.7b–c), the mathematical model and no-shear CFD model predict similar depths, with both predicting the depths increase in proportion to the incident amplitude. The mathematical model predicts slightly greater depths, with the difference decreasing farther along the step and increasing as incident amplitude increases. For example, at $x = 0.1\,\mathrm{m}$ the models differ by $< 0.4\,\mathrm{mm}$ (11%) for $a \leq 15\,\mathrm{mm}$, and by $1.5\,\mathrm{mm}$ (14%) for $a = 20\,\mathrm{mm}$. The no-slip CFD model predicts notably deeper overwash at these locations due to the boundary layer discussed in section 3.2.2, and does not predict that the depth increases in direct proportion to the incident amplitude.

The mean depth averaged horizontal velocity of the overwash tends to increase as the incident wave amplitude increases and with distance along the step. Similar to the mean depths, at the interface, $x = 0^+$ (figure 3.7d), the velocities predicted by the CFD models agree (differences $< 0.01\,\mathrm{m\,s^{-1}}$). At the interface, the CFD models predict positive mean velocities but only very small values, whereas the mathematical model predicts positive values up to a factor of eight greater than the CFD models. Again, this is indicative of the mathematical model's inability to model the wave breaking seen in figure 3.5(a).

The mathematical and the no-shear CFD models agree farther along the step (figures 3.7e–f) with respect to depth averaged velocity, although the no-shear CFD model systematically predicts $\sim 0.04\,\mathrm{m\,s^{-1}}$ greater velocities for all amplitudes and locations. This corresponds to a relative difference between 11–15% at $x = 0.1$ and 8–10% at $x = 0.5\,\mathrm{m}$. Farther along the step, the no-slip CFD model predicts slower overwash than the other models, again, due to the presence of a boundary layer.

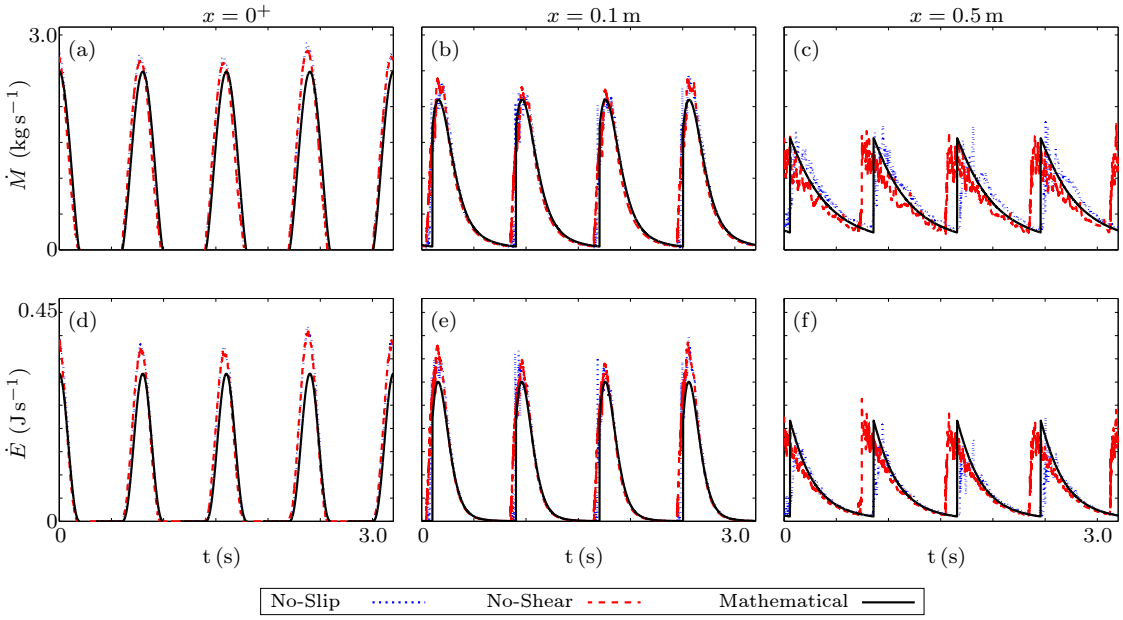

Figure 3.8: Horizontal mass flux versus time (top panels) and horizontal energy flux versus time (bottom panels) predictions given by mathematical model (solid black), no-shear CFD model (broken red), and no-slip CFD model (dotted blue). Plots are for incident wave amplitude $a = 10\,\mathrm{mm}$, and sampled at $x = 0^+$ (left panels), 0.1 m (centre), and 0.5 m (right) along the step.

3.4.2 Overwash mass and energy flux comparisons

Figure 3.8 is like that of 3.6 but for horizontal mass flux and energy flux signals of the overwash through a vertical cross section, and contains the no-slip CFD model in dotted blue. The mass flux (through a vertical cross section), $\dot{M}$, is given by

$$\dot{M} = \rho_w \hat{u} h \quad \text{and} \quad \dot{M} = \int_0^\infty \rho_w u \gamma \, \mathrm{d}z \tag{3.13}$$

for the mathematical and CFD models, respectively. The energy flux (through a vertical cross section), $\dot{E}$, is given as the flux of gravitational and kinetic energy plus the work done by pressure over the cross section. It is

$$\dot{E} = \frac{1}{2}\rho_w \hat{u}^3 h + \rho_w g \hat{u} h^2 \quad \text{and} \quad \dot{E} = \int_0^\infty \rho_w \left(\frac{1}{2}\mathbf{u}\cdot\mathbf{u} u\gamma + gzu\gamma \right) + pu\gamma \, \mathrm{d}z, \tag{3.14}$$

for the mathematical and CFD models, respectively, where the atmospheric pressure in the surrounding air is normalised to $p_{\mathrm{atm}} = 0$. Note that the second equation in 3.14 reduces

to the first equation under the shallow-water assumption, which models the pressure as hydrostatic (Vreugdenhil, 1994).

Unlike the depth signals in figure 3.6, the mass fluxes of all models agree strongly at the $x = 0^+$ location in terms of signal peaks, phase, frequency, and shapes. At the next location downstream, $x = 0.1\,\mathrm{m}$ the agreement between all three models remains strong, with the only significant difference between mathematical and CFD models being a small amount of noise around the signal peaks. At the farthest downstream position, $x = 0.5\,\mathrm{m}$, the CFD signals develop a high level of noise and a small phase shift as (seen in figure 3.6). However, other than these differences, the models again show strong agreement in terms of shape and size.

For the energy fluxes at $x = 0^+$ the CFD models compare favourably to the mathematical model, where the only major difference is peaks in the mathematical model being $\sim$ 9% less than in the CFD models. At this location all three models predict the peak energy flux is ~ 4.3 times greater than the mean energy flux (which was time averaged over 4 wave periods throughout this investigation). At the $x = 0.1\,\mathrm{m}$ position the CFD signals are in almost exact agreement, although there is slightly more noise in the no-slip model's signal at its peak. The mathematical model also shows the same kind of agreement with the other models at this location, wherein the signals have similar shapes but with peaks approximately 9% less than the CFD models. At this location, the peak energy flux is again ~ 4.3 times greater than the mean energy flux for all three models. At the final location, $x = 0.5\,\mathrm{m}$, the no-slip model has become noticeably smaller than the no-shear model, which is because of the additional energy dissipation effects in the boundary layer. At this location the mathematical model still shows strong agreement with the no-shear model, although there is small the phase shift and small amount of noise about the peaks of the no-shear models. At this final location, the peak energy flux is reduced to ~ 3.5 times greater than the mean energy flux, which is again consistent across all three models. The results presented in figure 3.8 are representative of all waves tested in terms of the mass and energy flux signals, including the relative ratios between peak and mean energy fluxes.

Figure 3.9 is similar to figure 3.7, but for the mean mass flux (top panels) and mean energy flux (bottom panels), and with inserts that show the mean energy flux of the

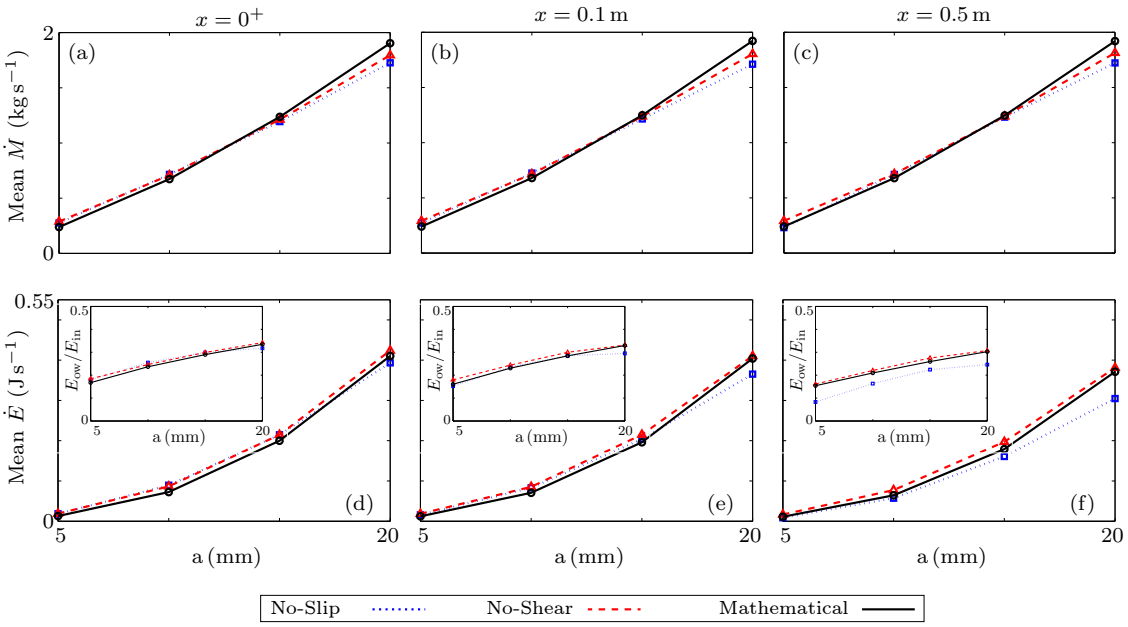

Figure 3.9: As in figure 3.7 but for mean mass mass flux (top panels) and mean energy flux (bottom) through a vertical cross section.

overwash, E_{ow}, as a portion of the mean incident wave energy, E_{in}. For these inserts the mean energy of the incident wave of the mathematical model is given by

$$E_{\mathrm{in}} = \frac{\rho_w \omega g a^2}{4k}\left(1 + \frac{2kH}{\sinh(2kH)}\right) \tag{3.15}$$

(Mei *et al.*, 1989). Although the CFD models use a fifth order stokes wave, this expression is also used for the nondimensionalisation of the CFD models, as higher order effects have a negligible impact on the mean energy flux (Whitham, 1962). The values of E_{ow} are calculated by time averaging the $\dot{E}$ variables given in equation 3.14 over 4 wave periods.

The mass fluxes (figures 3.9a–c) increase in weakly superlinear trend with respect to increasing incident wave amplitude, and the mass fluxes are independent of the measurement location, which is a consequence of the models being based on conservation of mass. The mathematical and CFD models agree closely. For mid-range amplitudes, $a = 10$ and 15 mm, the maximum absolute difference is as little as $0.05\,\mathrm{kg\,s^{-1}}$, and the relative difference is $\sim 5\%$. Agreement is weakest for the largest incident amplitude, $a = 20\,\mathrm{mm}$, wherein the mathematical model predicts a flux $0.11\,\mathrm{kg\,s^{-1}}$ greater than the no-shear CFD model, and $0.17\,\mathrm{kg\,s^{-1}}$ greater than the no-slip CFD model. For $a = 20\,\mathrm{mm}$ the relative difference between the mathematical and no-shear CFD models remains $\sim 5\%$, but the

relative difference between mathematical and no-slip model increases to $\sim 9\%$.

The energy fluxes (figures 3.9d–f) display a stronger superlinear increase with respect to increasing incident wave amplitude than the mass fluxes, and decrease with distance along the step. At the interface, $x = 0^+$, the models closely agree, with differences of $< 0.02\,\mathrm{J\,s^{-1}}$ for all a. This level of agreement is largely maintained at the point where bores have just developed, $x = 0.1\,\mathrm{m}$, except for the largest incident amplitude, wherein the no-slip CFD model predicts an energy flux $\sim 0.04\,\mathrm{J\,s^{-1}}$ less than the other models. At the farthest location along the step, $x = 0.5\,\mathrm{m}$, the differences between the mathematical and no-shear CFD models are still $< 0.02\,\mathrm{J\,s^{-1}}$, but the no-slip CFD model consistently predicts the smallest energy fluxes, with differences increasing as the incident amplitude increases, up to $0.07\,\mathrm{J\,s^{-1}}$ ($\sim 23\%$) for the largest incident amplitude.

The decreases in energy flux along the step (from $x = 0$ to $0.5\,\mathrm{m}$) are 9.5–12% for both the mathematical and no-shear CFD models. This is an energy flux reduction of approximately $0.003\ \mathrm{J\,s^{-1}\,m^{-1}}$ and $0.078\,\mathrm{J\,s^{-1}\,m^{-1}}$ over the $0.5\,\mathrm{m}$ for the lowest and highest incident amplitude, respectively. Breaking effects around the bores are the primary source of energy dissipation in the no-shear CFD model, whereas energy dissipation in the mathematical model is a consequence of the discontinuity over the bore-front. The agreement in energy fluxes indicates that the energy losses due to the highly complicated breaking effects in the CFD model are similar to those predicted by the simplified shallow-water model of the bore.

The no-slip CFD model predicts significantly larger decreases in energy flux between $x = 0^+$ and $x = 0.5\,\mathrm{m}$, due to additional viscous forces in the boundary layer (Schlichting & Gersten, 2016). The decrease is 54% for the smallest incident amplitude, and 24% for the largest amplitude. This corresponds to a much larger average energy flux decrease (compared to the other models) of $0.020\ \mathrm{J\,s^{-1}\,m^{-1}}$ and $0.177\,\mathrm{J\,s^{-1}\,m^{-1}}$ over the $0.5\,\mathrm{m}$ distance, for the lowest and highest incident amplitudes, respectively.

The insets in figures 3.9(d–f) show the models predict 15–35% of the incident wave energy enters the overwash, and that a greater portion of the incident wave energy enters the overwash as the incident amplitude increases in a weakly sublinear trend. At $x = 0^+$, the models differ by less than 3%. Farther along the step, at $x = 0.1$ and $0.5\,\mathrm{m}$, the mathematical and no-shear CFD models retain this agreement, and predict the decrease

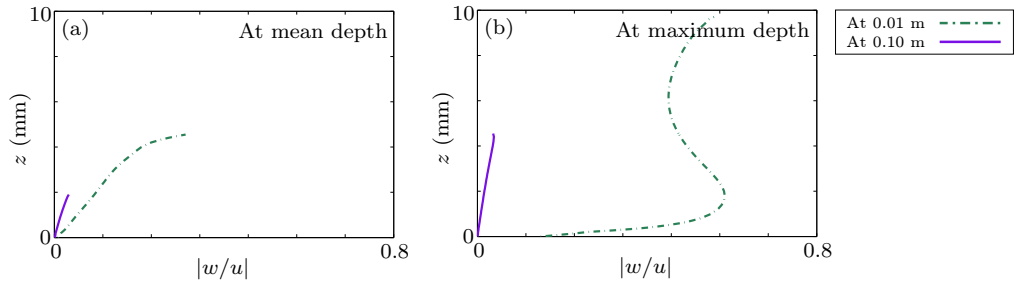

Figure 3.10: Magnitude of vertical velocity divided by horizontal velocity as functions of height, z, by no-shear CFD model. Results are sampled sampled at $x = 0.01\,\text{m}$ (solid purple curves) and $x = 0.1\,\text{m}$ (dot dashed green) and are produced by incident amplitude $a = 10\,\text{mm}$, for instants of time when overwash at the respective locations are: (a) at their mean depths, and (b) at their maximum depths.

in energy flux from $x = 0^+$ to $x = 0.5\,\text{m}$ is less than 4% of the incident energy flux for all amplitudes tested. The no-slip CFD model predicts a larger decrease in energy flux, ranging from 13% of the incident energy flux for $a = 5\,\text{mm}$, to 8% for $a = 20\,\text{mm}$.

3.4.3 Shallow-water transition

Figure 3.10 shows no-shear CFD model predictions of $|w/u|$ (i.e. the magnitude of the vertical velocity divided by the horizontal velocity), with respect to height (z), for instants when the overwash is at its mean depth (a) and maximum depth (b), at $x = 0.01\,\text{m}$ (dot-dashed green) and $0.1\,\text{m}$ (solid purple). As bores develop in the region $0.02 < x < 0.1\,\text{m}$ (in all cases tested) the $x = 0.01\,\text{m}$ location is indicative of the region before bores manifest, and the $x = 0.1\,\text{m}$ location is indicative of when bores have formed. Therefore, the location $x = 0.01\,\text{m}$ represents behaviours as the water transition onto the step, and $x = 0.1\,\text{m}$ represents locations where bores have just developed. Corresponding profiles given by the no-slip CFD model (not presented) are similar, although the velocity ratio is marginally smaller for z less than approximately $1.5\,\text{mm}$.

At $x = 0.1\,\text{m}$, the vertical velocity is always at least an order of magnitude less than the horizontal velocity in both instances, with $|w/u| < 0.033$, but generally much less than that. In contrast, at $x = 0.01\,\text{m}$, the vertical velocity is frequently the same order of magnitude as the horizontal velocity, particularly when the overwash is at its

maximum depth, where $|w/u| = 0.6$ to 0.7 for $z > 1\,\text{mm}$ (i.e. for most of the water's depth). Therefore, the no-shear CFD model predicts the overwash transitions to being shallow — in the sense of the underlying assumption of shallow-water theory that the vertical velocity is much less than the horizontal velocity (Vreugdenhil, 1994) — in the interval $0 < x \leq x_{\text{trans}} < 0.1\,\text{m}$. This indicates the shallow-water model of the overwash is valid for $x \geq x_{\text{trans}}$, partially explaining the differences between the overwash depths and velocities predicted by the mathematical model and the CFD models at the interface ($x = 0^+$), and the close agreement between the mathematical model and no-shear CFD model for $x \geq 0.1\,\text{m}$ (as shown in figures 3.5–3.6). The transition to agreement in terms of height and velocity implies underlying agreement between the models, and figure 3.9 provides evidence that it is agreement in terms of mass and energy fluxes that guides the transition, noting that both models are based on conservation of mass and momentum (closely related to energy).

Defining the water to be shallow when the vertical velocity is an order of magnitude less than the horizontal velocity for all t, in all cases tested $x_{\text{trans}} < 0.05\,\text{m}$. Therefore, the transition distance, x_{trans}, is much less than (by at least an one order of magnitude) the distance between bore-fronts ($\sim 0.5\,\text{m}$) and the incident wave's wavelength ($\lambda = 1.0\,\text{m}$), which are the principle horizontal length scales in the overwash and basin, respectively. Additionally, it was found that the value of x_{trans}, i.e. the length of the transition region, increases as the incident wave amplitude increases (not shown), partially explaining the better agreement between depths and velocities predicted by the mathematical and no-shear models at $x = 0.1\,\text{m}$ in figures 3.7(b,e) for smaller incident amplitudes. Moreover, the CFD model (with no-shear or no-slip conditions) predicts $|w/u|$ becomes smaller the farther the overwash propagates along the step, explaining the improved agreement between no-shear and mathematical model from $x = 0.1\,\text{m}$ (figures 3.7b,e) to $x = 0.5\,\text{m}$ (figures 3.7c,f).

3.5 Summary

Two dimensional overwash of a step by small steepness regular incident waves has been analysed using a CFD model based on the two-phase incompressible Navier Stokes equa-

tions. The CFD model was shown to capture overturning, vortices, and air entrainment at the step front where the overwash is generated, as well as breaking in the bores along the step; but at a heavy computational expense (120 h on 96 cores per 30 s of simulation).

A simplified mathematical model of this interaction was also developed. It was based on the modelling principles of overwash of a floating elastic plate in section 2.3, which used linear potential-flow theory to model the waves, and the nonlinear shallow-water equations to model the overwash. The mathematical model neglects the complex dynamics at the step front where the overwash is generated, but runs significantly faster than the CFD model and on a single core only (0.2 h for 15 s simulation time).

The primary findings are:

1. As expected, the overwash becomes deeper, faster, and more energetic as the incident wave amplitude increases.

2. The models predict the proportion of incident wave energy forced into the overwash ranges from 16% for the smallest incident wave amplitude tested, to 35% for the largest amplitude.

3. The no-slip boundary condition on the step's surface creates a ~ 2 mm thick boundary layer (consistent for all incident wave amplitudes tested at period $T = 0.8$ s), making the overwash deeper and slower than in simulations where a no-shear boundary condition was applied.

4. The mathematical model predicts shallower and faster overwash than the CFD models directly above the front of the step, but near identical depths and depth averaged horizontal velocities to the CFD model with no-shear boundary conditions farther along the step.

5. The mathematical and no-shear CFD models predict almost identical mean mass and energy fluxes at the step edge and along the step. This provides an explanation of why the models agree in terms of depths and velocities once the CFD model transitions to a shallow-water flow despite the significant differences where the overwash is generated. The no-slip CFD model predicts similar energy fluxes at the step's

edge, but smaller energy fluxes as the overwash propagates along the step due to the viscous boundary layer.

6. In the CFD models the transition region to shallow-water flow is small relative to the primary horizontal length of the interaction — the distance between bore-fronts and the wavelength of the incident wave.

This chapter indicates that a low-cost mathematical model, based on linear potential-flow theory to model overwash forcing, and shallow-water theory to model the overwash itself, is viable to model the overwashed water. It provides further evidence that the large overpredictions of overwash made by the mathematical model in chapter 2 are due to the collisions of bores coming from the leading and trailing edge of the plate, rather than being because the shallow water equations do not comprehensively capture the complicated edge dynamics, which are found to occur over a relatively small transition region. It also suggests that the overwash model may be improved by incorporating boundary layer effects into the shallow-water model.

Chapter 4

Wave reflection by an overwashed step

4.1 Introduction

In this chapter the waves reflected by the CFD model of an overwashed step (from chapter 3) are analysed. Four simplified theoretical models are then considered in order to produce the same wave reflection results of the CFD model. The models use the overwash predictions of the simplified model in section 3.3 to correct the wave reflection using conservation of mass, momentum, and energy principles.

This approach is distinctly different to the similar problem of a submerged rectangular shelf found in (Grue, 1992), which couples the flow into/out of the region above the shelf using a time dependent boundary condition. The problem is approached in this manner as the solution technique of Grue (1992) cannot readily be applied to the overwash problem. The principle reason for this is because that solution technique requires that the distance between the step's upper surface and the water's equilibrium free surface level at the shelf's vertex to be large relative to the water's free surface displacement. This is not the case in the overwash problem considered here as the step's upper surface is exactly level with the equilibrium free surface level of the water to the left of the step.

The objectives of the chapter are to:

1. Analyse the reflected waves created by the CFD model of an overwashed step.

2. Develop a simplified mathematical model of the waves reflected by an overwashed step.

4.2 CFD reflection analysis

CFD simulations as described in chapter 3 were run with depths probes to the left of the step. An additional benchmark test was also made with a step tall enough such that overwash did not occur. For the cases with $\lambda = 1.0\,\mathrm{m}$ (and corresponding $T = 0.8\,\mathrm{s}$ and $\omega \approx 7.85\,\mathrm{rad\,s^{-1}}$) the simulations were saved such that data could be extracted from any location to the left of the step. For cases with $\lambda = 1.5$ and $0.56\,\mathrm{m}$ time and data constraints lead to data only being stored for probes at $x = -2.00$ and -1.00 m, for which the results were found qualitatively similar to $\lambda = 1.0\,\mathrm{m}$. Unfortunately, however, the limited probe locations meant that the wave field could not be analysed adequately for $\lambda \neq 1.0\,\mathrm{m}$ because (i) for $\lambda = 0.56\,\mathrm{m}$ the probes were roughly spaced at multiples of the wavelength, and (ii) an accurate analysis of the incident and reflected wave spectra requires three probe locations (Mansard & Funke, 1980). Results are therefore presented for the $\lambda = 1.0\,\mathrm{m}$ case only.

4.2.1 Qualitative analysis

Figure 4.1(a) shows the free surface signal for the no-shear CFD model with incident waves of $\lambda = 1.00\,\mathrm{m}$ and $a = 5\,\mathrm{mm}$ at $x = -2.00\,\mathrm{m}$ (i.e. two metres to the right of the step), where the step's height was raised such that overwash did not occur. The black vertical lines in this figure indicate three of the four stages of the simulation.

For $0 < t < 12\,\mathrm{s}$ waves are being generated by the wave-maker to their specified amplitude and approaching the step. For $12 < t < 20\,\mathrm{s}$ the reflected wave field is in a transient state wherein the reflected waves are approaching a periodic state. For $20 < t < 27\,\mathrm{s}$ the wave field has reached the periodic state, without additional reflection effects from the wave maker located at $x = -8\,\mathrm{m}$. For $t > 27\,\mathrm{s}$ until the simulation stopped running at $t = 30\,\mathrm{s}$, additional reflection effects from the wave-maker would occur, although this is not shown in the figure.

Figure 4.1(b) shows the free surface signal for the same simulation but zoomed into the

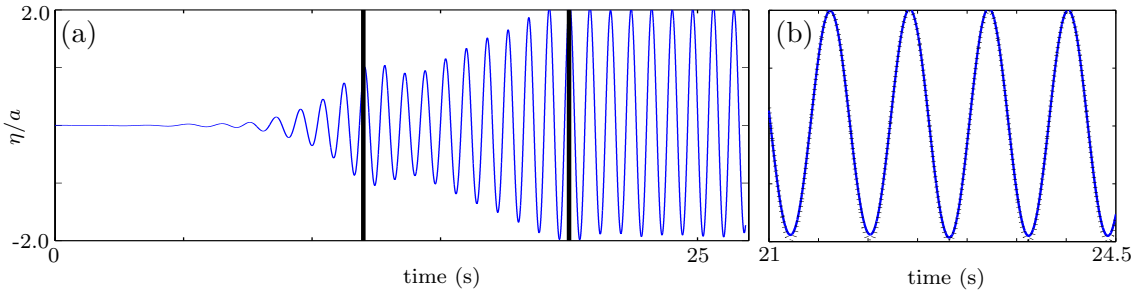

Figure 4.1: Plots of the water's free surface height versus time at $x = -2.00\,\mathrm{m}$ for $a = 5\,\mathrm{mm}$ and a raised step such that overwash could not occur. Plot (a) shows the free surface elevation with $t = 0$ corresponding to the starting time of the wave-maker. Plot (b) is a zoomed-in view for $21 < t < 24.5\,\mathrm{s}$ where the wave motion has become is periodic. The no-slip CFD model is in solid blue and the linear potential theory model (without overwash) is in dotted black (b only).

interval $21 < t < 24.5\,\mathrm{s}$. The signal is overlaid with the dotted black signal corresponding to the standing wave field that linear potential theory predicts when no overwash occurs (derived in section 3.3). The signals have been offset such that their peaks occur at the equivalent time. Both signals are in near perfect agreement here indicating that the standing wave field is a valid if no overwash occurs, as expected.

Figure 4.2 is as in figure 4.1 but for $a = 15\,\mathrm{mm}$ (such that overwash is more pronounced than for $a = 5\,\mathrm{mm}$), the step's upper surface at the equilibrium water level (i.e. with the

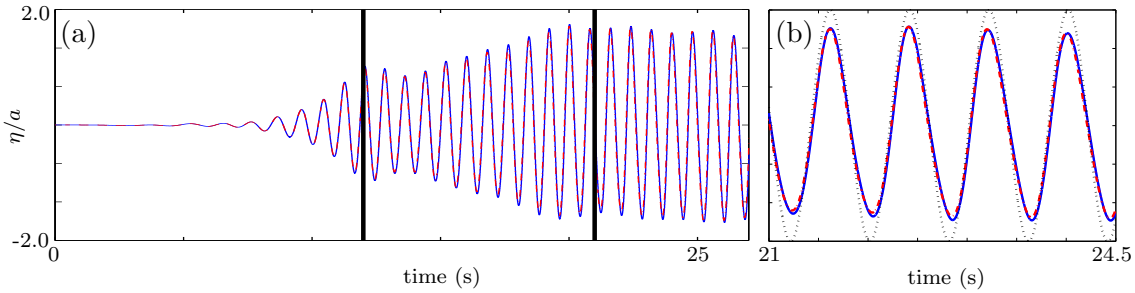

Figure 4.2: As in 4.1 but for $a = 15\,\mathrm{mm}$, a step with vertex located at $x = z = 0$, and the no-slip CFD model in dot-dashed red.

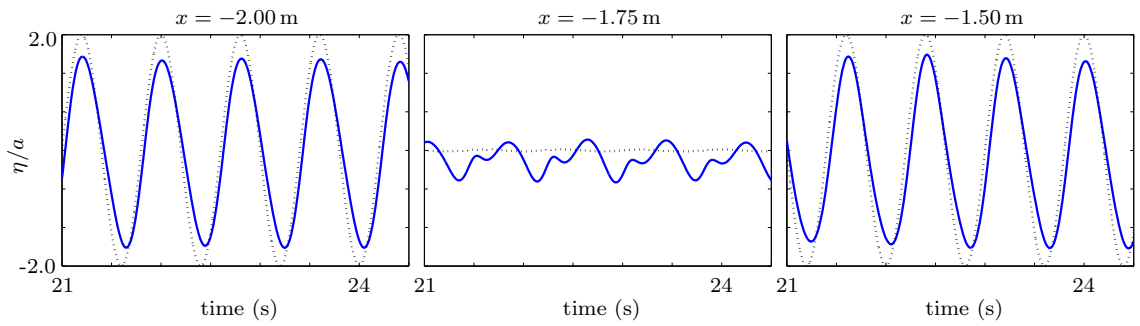

Figure 4.3: Plots of the water's free surface height versus time for $a = 15\,\mathrm{mm}$ at $x = -2.00\,\mathrm{m}$, $x = -1.75\,\mathrm{m}$ and $x = -1.50\,\mathrm{m}$. CFD model in blue and linear potential theory in dotted black.

step geometry as outlined in section 3.2.1), and with the no-slip model in dashed red. Results in this figure are representative of all waves tested with this step geometry.

In panel (a) the first two stages of the simulation are similar to those in figure 4.1(a), although the transition interval is extended by ~ 1 to $2\,\mathrm{s}$. The third stage is also similar, however, the free surface elevation is smaller due to reduced wave reflection, and the motion is less strongly periodic, likely due to the nonlinearity of the overwash. Panel (b) exemplifies this difference in the third stage of the simulation. It shows the period of oscillation between CFD and standing wave field are both $0.8\,\mathrm{s}$, however, the amplitude of the CFD signals is significantly reduced, with a difference between peaks and troughs of $\sim 82\%$ less than that of the standing wave model. In panels (a) and (b) the signals of no-slip model shows near exact agreement with the no-shear model, implying that the wave reflection from the step is invariant of the surface condition on the step. This was found for all waves tested. Hence, for simplicity, future results are discussed with reference to the no-shear CFD model only.

Figure 4.3 shows the free surface signal once periodic motion has been reached for waves of $a = 15\,\mathrm{mm}$ sampled at $x = -2.00$, -1.75, and $-1.50\,\mathrm{m}$. The signal at $x = -2.00\,\mathrm{m}$ is near identical to the signal at $x = -1.50\,\mathrm{m}$, except that it is vertically flipped about $\eta = 0$. Noting that the wavelength of the incident wave is $\lambda = 1.0\,\mathrm{m}$, this indicates that $x < -1.50\,\mathrm{m}$ is sufficiently far from the step for localised nonlinear behaviours around the step's edge to be eliminated. The signals at $x = -2.00$ and $-1.50\,\mathrm{m}$ are of similar shape

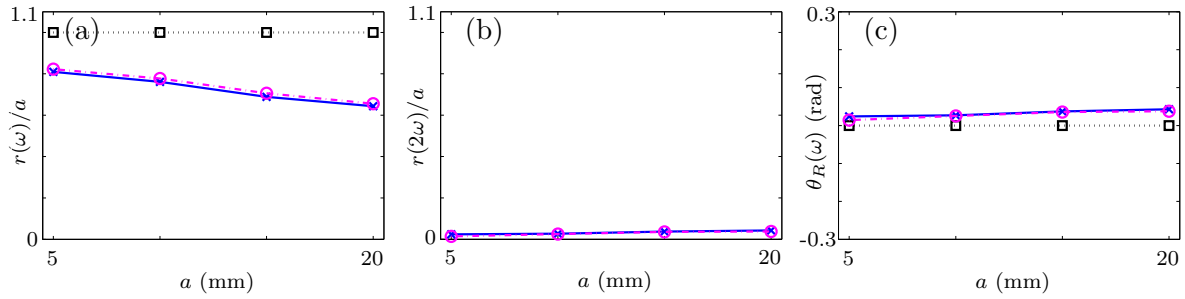

Figure 4.4: Plot of reflected wave amplitude (r) as a portion of the incident wave amplitude versus incident wave amplitude for frequency bin ω (a), and frequency bin 2ω (b); and phase difference between reflected and incident waves at frequency ω (c). CFD model near the step in dot-dashed magenta with circles, CFD model far from the step in solid blue with crosses, and linear model with no overwash in dotted black with squares.

to the standing wave model, but with a reduced amplitude of $\sim 84\%$. As in figure 4.2, this emphasises the overwash produces a reduction in wave reflection. The CFD signal at $x = -1.75\,\text{m}$ is oscillating between $-0.55 < \eta/a < 0.19$, with multiple peaks and troughs per wave period. In contrast, the standing wave model signal shows almost complete cancellation between reflected and transmitted waves because in the standing wave model $r = a$ and $-7/4\lambda = -1.75\,\text{m}$. The difference is again indicative of reduced wave reflection at the fundamental frequency (i.e. the frequency of the incident wave), and the multiple peaks per wave period in the CFD signal indicates that waves are reflected at frequencies above the incident wave's frequency.

4.2.2 Spectral analysis

The wave field was analysed to determine the incident and reflected spectra of the waves to the left of the overwashed step. The spectral analysis was performed using the three probe fast Fourier transform least square estimate method outlined in Mansard & Funke (1980). Probes were placed close to and far from the step. The probes far (far field probes) from the step were located at $x = -2.00$, -1.90, and -1.88 m as figure 4.3 demonstrates localised nonlinear effects near the step do not occur in this region. The probes near (near field probes) to the step where located at $x = -0.40$, -0.30, and -0.20 m. They were

placed there in order to compare the wave field at $x \approx -0.3\lambda$ to the wave field where the localised nonlinear effects near the step would not occur. The probes were analysed for $21.5 < t < 24.5\,\mathrm{s}$ as figure 4.2 indicated this was once periodic motion was reached at each location. As this time interval is $5T$, the reflected and transmitted spectra were therefore placed frequency bins were centred at multiples of 0.25ω with width 0.25ω. The results of the spectral analysis are presented in order to aid the development of a simplified mathematical model of the overwashed step. Therefore, results are taken using the approximation that the waves occur at the exact centre of the frequency bin, rather than accounting for the continuous spread across the frequency spectrum.

Figure 4.4(a) and (b) shows the reflected wave amplitude at the frequency bin centred at ω (a) and 2ω (b) against the incident wave amplitude, where $r(\omega)$ and $r(2\omega)$ are the reflected wave amplitudes at the ω and 2ω frequency bins, respectively. In both (a) and (b) the non-dimensionalising a is the incident wave amplitude prescribed by the wave-maker. Results are given for the wave probes near the step (dot-dashed magenta with circles), far from the step (solid blue with crosses), and the standing wave model (dotted black with squares). Results are presented for ω and 2ω only, because the reflection in other frequency bins was at least two orders of magnitude less than the incident wave.

Figure 4.4(a) shows that the reflected wave amplitude at the fundamental frequency in far-field probes ranges between 81% and 64% of the incident wave amplitude, with the largest reduction occurring for higher amplitude incident waves. As the standing wave model predicts $r = a$ at the fundamental frequency, it therefore demonstrates that overwash significantly reduces wave reflection. As a increases $r(\omega)$ decreases. Hence the plots demonstrate that the reduction in reflected wave amplitude is strongest when the overwash is deeper and more energetic (as per the results in section 3.4). The results for the near and far CFD probes follows a similar downwards trend although the near field probe has a minor vertical shift. The difference between near and far field probes ranges from 2.5% for $a = 15\,\mathrm{mm}$ to 1.5% for $a = 5\,\mathrm{mm}$, and is on average 1.7%. Therefore, the reflected waves near and far from the step are similar at the fundamental frequency, and are both significantly less than when no overwash occurs.

Figure 4.4(b) shows that $r(2\omega)/a$ slightly increases as a increases and ranges from 1.4% to 3.7% in both the near and far-field probes. The waves reflected by the step at

twice the fundamental frequency are therefore approximately an order of magnitude less than the incident wave amplitude, and are slightly more prevalent for deeper and more energetic overwash. The difference between $r(2\omega)$ between near and far field probes is always less than $0.01a$, and on average $0.005a$. The standing wave model predicts no waves at this frequency, and therefore overwash appears to be the cause of these higher frequency waves.

The ratio between $r(\omega)$ and $r(2\omega)$ is indicated by the juxtaposition of figures 4.4(a) and (b). The ratio ranges from $r(\omega)/r(2\omega) \sim 3\%$ for $a = 5\,\text{mm}$ to $r(\omega)/r(2\omega) \sim 7\%$ for $a = 20\,\text{mm}$, and is on average $\sim 5\%$. The results therefore indicate that the higher order reflection effects are small relative to the incident wave amplitude, and the amplitude of the reflected wave at the fundamental frequency. Furthermore, because wave power is proportional to the amplitude squared multiplied by its period (Holthuijsen, 2010), this also indicates that the energy contained in the higher order reflected waves is small relative to the waves at the fundamental frequency.

Figure 4.4(c) shows the phase difference between incident and reflected waves at the fundamental frequency, $\theta_R(\omega)$, for both the CFD and standing wave model. It shows that the reflected wave is slightly out of alignment with the incident wave, with a phase difference difference between 0.014 and 0.0377 rad. This phase difference is a marginal increase from the standing wave model, which predicts the incident and reflected waves are in perfect alignment. Nonetheless, CFD phase difference is negligibly small when compared to the phase difference to put the waves perfectly out of phase (π rad), implying the difference in phase is relatively negligible when compared to the results of the standing wave model.

4.3 Simplified reflected wave calculation methods

Four simplified models are developed in order to calculated the waves reflected by the overwashed step. The first model uses conservation of mass principles. The second uses conservation of momentum principles. The third and fourth use conservation of energy principles. Each model uses a number of similar assumptions and therefore, to avoid repetition, their common assumptions are as follows.

Consider the same problem geometry as in section 3.3 where the velocity of the water normal to the basin boundaries is zero (i.e. the walls are no-penetration conditions). For all x and z the water is assumed to be incompressible such that ρ_w is constant. Additionally, it is assumed that for all x and z the water is in a periodicity varying steady state such that there is not net accumulation/loss of mass, momentum, or energy in any arbitrary volume of water over a wave period, T.

Based on the findings of chapter 3, it is assumed that the overwash forecasting model (i.e. the simplified mathematical model in section 3.3) can accurately calculate the mass, momentum, and energy, fluxes for $x > 0$, once the overwash becomes periodic. This assumption is made in order to avoid having to implement a dynamic (time varying two-way) coupling condition between the overwash and deep water domain, which is an exceptionally challenging task given the inherent differences in these kinds of flows. It therefore means that the models that will be developed predict the overwash then correct the surrounding wave field. The expressions for the mass, momentum, and energy fluxes in the overwash will be derived by under the shallow-water assumptions. Recounting earlier chapters, these are: For $x > 0$, the vertical velocity, w, is negligible, the horizontal velocity is $u(x, z, t) = \hat{u}(x, t)$, and the pressure, $p = -\rho_w g z$, is hydrostatic (Vreugdenhil, 1994). When scaled by the water's density, they are $h\hat{u}$ (recall that h is the water's depth) for the mass flux, $h\hat{u}^2 + 0.5gh^2$ for the momentum flux, and $0.5h\hat{u}^3 + gh^2\hat{u}$ for the energy flux (Billingham & King, 2000). In short, the principle assumption of these models is that these terms can be calculated accurately for $x > 0$ using the model of section 3.3.

For $x \ll 0$ localised non-linear overwash effects and waves outside the fundamental frequency are assumed to be negligible based on the findings of the spectral analysis in section 4.2. Hence, for $x \ll 0$, the water is modelled using linear potential water wave theory (Mei *et al.*, 1989), such that

$$\phi(x, z, t) = \left(A \sin(\omega t - kx) + B \sin(\omega t + kx + \theta_R)\right) \frac{\cosh(k(z + H))}{\cosh(kH)}, \tag{4.1}$$

where ω is the incident wave's frequency, a is the incident wave amplitude, $A = -g\omega^{-1}a$, $B = -g\omega^{-1}r$, r is the (now unknown) reflected wave amplitude, and θ_R is the phase

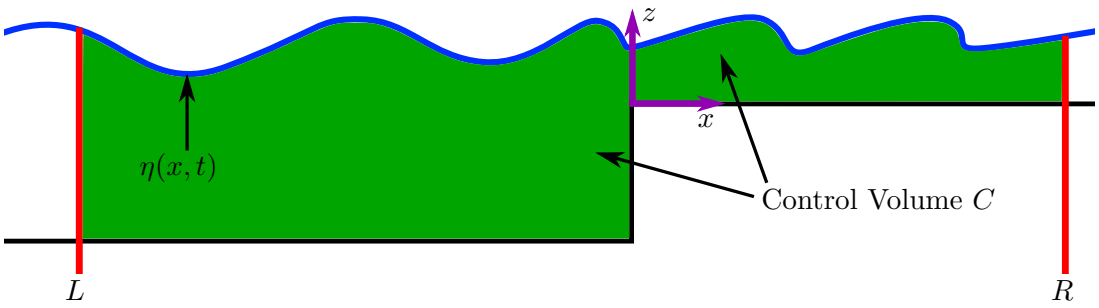

Figure 4.5: Schematic of control volumes C around the step (not to scale).

difference between incident and reflected waves[1]. It is approximated that $\theta_R = 0$ because this is the phase difference for when no overwash occurs, and because the CFD results for θ_R found the phase difference to be small. According to linear potential theory, for $x \ll 0$, $(u, w) = \nabla\phi$, the pressure is given by the unsteady Bernoulli equation

$$p = -\rho_w \partial_t \phi - \rho_w g z - \frac{1}{2}\rho_w \left(u^2 + w^2\right), \tag{4.2}$$

and the free surface displacement is obtained via the linearised free surface condition

$$\eta = -\frac{1}{g}\partial_t \phi(x, 0, t). \tag{4.3}$$

Finally, for $x < 0$ the deep water approximation, $\tanh(kH) = 1$, is taken in because it is accurate to 3 significant figures for the waves tested in the CFD model. This final approximation is not needed in the construction of the models, however, it significantly simplifies calculations as the dispersion relation becomes $k = \omega^2 g^{-1}$.

4.3.1 Conservation of mass method

Method derivation

Consider the control volume C, shown in figure 4.5, that bounds the water between the basin boundaries, the water's free surface, and some fixed $x = L \ll 0$ and $x = R > 0$. Conservation of mass dictates that the accumulation of mass inside the control volume is

[1] Note that, if the step is tall enough such that no overwash occurs, equation 4.1 has the solution $a = r$ and $\theta_R = 0$ (as implied by section 3.3), which results in the standing wave field shown in figure 4.4 (dotted black with squares).

equal to the mass entering minus the mass leaving. Mathematically, this is given as

$$\int_C \frac{\partial}{\partial t}\rho_w \,\mathrm{d}V + \int_{\partial C} \rho_w u_{\mathbf{n}} \,\mathrm{d}S = 0 \tag{4.4}$$

where ∂C is the boundary of the control volume C, and $u_{\mathbf{n}}$ is the outwards normal velocity of the flow relative to the velocity of the boundary (Gallavotti, 2002).

As the velocity of the water on the basin boundaries is zero, the velocity of the water at the free surface relative to the free surface boundary is zero, ρ_w is constant, and the internal mass changes are assumed to be periodic with period T, time averaging gives

$$-\overline{\int_{-H}^{\eta} u|_{x=L} \,\mathrm{d}z} + \overline{\int_{0}^{\eta} u|_{x=R} \,\mathrm{d}z} = 0. \tag{4.5}$$

Note that the notation $|_{x=\bullet}$ denotes function inside the integral (as well as its limits) are evaluated at $x = \bullet$, and

$$\overline{(\bullet)} = \frac{1}{T}\int_{t_0}^{t_0+T} \bullet \,\mathrm{d}t \tag{4.6}$$

is the time averaging operator over a wave period, where t_0 is an arbitrary instant in time once the system is at a periodic steady state. Physically, equation 4.5 is the statement that over a wave period the mass entering the system is equal to the mass leaving the system.

The right-hand term of 4.5 is evaluated using the shallow-water assumption $u(x, z, t) = \hat{u}(x, t)$, which gives

$$\overline{\int_{0}^{\eta} u|_{x=R} \,\mathrm{d}z} = \overline{h\hat{u}}|_{x=R}\,. \tag{4.7}$$

The left-hand term of 4.5 is evaluated by using the velocity potential given in 4.1, decomposing the limits to

$$\overline{\int_{-H}^{\eta} \partial_x\phi|_{x=L} \,\mathrm{d}z} = \overline{\int_{-H}^{0} \partial_x\phi|_{x=L} \,\mathrm{d}z} + \overline{\int_{0}^{\eta} \partial_x\phi|_{x=L} \,\mathrm{d}z}, \tag{4.8}$$

and taking the Taylor series expansion about $z = 0$. This gives

$$\begin{aligned}\overline{\int_{-H}^{\eta} \partial_x\phi|_{x=L} \,\mathrm{d}z} &= \overline{\int_{-H}^{0} \partial_x\phi|_{x=L} \,\mathrm{d}z} + \overline{(\eta\partial_x\phi\,(z=0))\,|_{x=L}} + O(k^4a^4) \\ &= 0 + \frac{kg}{2\omega}(a^2 - r^2) + O(k^4a^4).\end{aligned} \tag{4.9}$$

As the waves are low steepness the $O(k^4a^4)$ term is negligibly small (Whitham, 1962). Therefore, equation 4.5 becomes

$$\frac{kg}{2\omega}(a^2 - r^2) = \overline{h\hat{u}}|_{x=R}\,. \tag{4.10}$$

Physically, leftmost term corresponds to the water mass entering/exiting the system by the waves at $x \ll 0$ and the rightmost term corresponds to the water mass entering/exiting the overwash. The rightmost term is calculated using numerical integration from the outputs of the model in section 3.3 (note that R can be taken from any location along the step because mass is conserved along the step in the shallow-water description; as was shown in section 3.4).

Method analysis

The method was run for waves of $a = 5$, 10, 15, and 20 mm. For $a = 20$ mm the rightmost side of equation 4.10 resulted in $1.9 \times 10^{-3}\,\mathrm{m^2\,s^{-1}}$. In comparison, the maximum value of leftmost side of equation 4.4, which occurs for $r = 0$, is $16.0 \times 10^{-4}\ \mathrm{m^2\,s^{-1}}$; implying a real solution for r cannot be found. Similar results were found for all a, where the rightmost side of equation 4.4 could not be balanced by the leftmost term for any real r. This implies that under the given assumptions no reflected wave can account for the mass flux in the overwash, and therefore the mass flux balance cannot be used to calculate the reflected wave.

A result of this nature is unsurprising when considering the underlying models. The maximum instantaneous mass flux of linear water waves is an order of magnitude greater than the mass flux averaged over a wave period (Whitham, 1962). In contrast, the mass is transferred into the overwash only when $\eta(x = 0) > 0$, i.e. when the instantaneous mass flux of the water waves is largest. Thus, it is unlikely that the mean mass flux of the water waves could account for the mass entering the overwash.

However, the inability equation 4.10 to balance does not necessarily imply the linear water wave model is inconsistent with conservation of mass. Instead, it implies that for mass to be conserved, the velocity potential should be modified to

$$\phi = \left(A \sin\left(\omega t - kx\right) + B \sin\left(\omega t + kx\right)\right) \frac{\cosh(k(z + H))}{\cosh(kH)} + Dx, \tag{4.11}$$

where the D is some unknown mean flow coefficient, and the Dx corresponds to a net current of water. Note that this modification is still valid under the governing equations of linear potential theory, as demonstrated in Whitham (1962). Under this modification

of the velocity potential, the mass flux balance in equations 4.10 gets modified to

$$DH + \frac{kg}{2\omega}(a^2 - r^2) = \overline{h\hat{u}}|_{x=R}. \tag{4.12}$$

For $0 < r < a$ and $a = 5$, 10, 15, and 20 mm D was found to be of $O(k^2a^2)$ (or much lower). This implies that when considering the momentum or energy flux of the linear water waves its influence was negligibly small (this will not be shown because the proof is long, contains many awkward terms, and is un-insightful). Therefore, although this Dx term is required for the conservation of mass, the modified form of the velocity potential will not be considered when deriving the momentum and energy conservation methods.

4.3.2 Conservation of momentum method

Method derivation

Consider an arbitrary control volume of water, V. The conservation of momentum for this control volume is given by the vector equation

$$\int_V \frac{\partial}{\partial t}\left(\rho_w \mathbf{u}\right)\, \mathrm{d}V + \int_{\partial V} \rho \mathbf{u} u_{\mathbf{n}} + p\mathbf{n}\, \mathrm{d}S - \int_V \mathbf{F_{ext}}\, \mathrm{d}V = 0, \tag{4.13}$$

where $\mathbf{n}$ is the outwards pointing normal to ∂V, and $\mathbf{F_{ext}} = (0, -g)$ is the external forcing due to gravity (Gallavotti, 2002). In this equation, the first integral represents the increase in momentum in the control volume, the first term in the second integral represents the momentum entering/exiting the control volume, the second term in the second integral represents the force of pressure along the boundary, and the third integral is the external forcing due to gravity. As the system is assumed to be in a periodicity varying steady state this time averages to

$$\overline{\int_{\partial V} \mathbf{u} u_{\mathbf{n}} + \frac{p}{\rho_w}\mathbf{n}\, \mathrm{d}S} - \overline{\int_V \mathbf{F_{ext}}\, \mathrm{d}V} = 0. \tag{4.14}$$

For this equation there are two options for balancing the momentum flux of the overwash to the momentum flux of the wave field. A control volume can be drawn like that in section 4.3.1, or a control volume can be drawn such that the momentum fluxes balance across $0^- < x < 0^+$ and $z > 0$. In the former case the flow conditions around $x = 0$ must be known because of the dependence of p on w at the wall (see equation 4.2). In

the latter case the flow conditions must be known for $x = 0^-$ and $z > 0$. Therefore, although the mass method allowed the overwash to be balanced with the reflected wave without considering the flow around the step, equations 4.14 shows there is no such option when considering momentum. Thus, unlike in the mass conservation method, there are no options where the flow just to the left of the step can be ignored.

The simplest option of the two, however, is to consider the control volume taken as $0^- < x < 0^+$ and $z > 0$. For this, it is assumed that the potential given for $x \ll 0$ is valid up to $x = 0^-$ (the validity of this assumption will be tested when the method is analysed). For this control volume, equation 4.14 gives, in the x-direction,

$$\overline{\int_0^{\eta^-} u^2 + \frac{p}{\rho_w}|_{x=0^-} \, \mathrm{d}z} = \overline{\int_0^{\eta} u^2 + \frac{p}{\rho_w}|_{x=0^+} \, \mathrm{d}z}\,, \tag{4.15}$$

where $\eta^- = \max(\eta(x = 0^-), 0)$ is the height of the water's free surface just to the left of the step when $z > 0$.

Using the Taylor series expansion about the free surface and the shallow-water assumption (as in section 4.3.1) equation 4.15 gives

$$-\frac{k^2 g^2}{3\omega^2}(a-r)^2(a+r) + \frac{k^2 g^2}{6\omega^2}(a+r)^3 + \frac{g}{8}(r+a)^2 + O(k^4a^4) = \overline{h\hat{u}^2 + \frac{1}{2}gh^2|}_{x=0^+}, \tag{4.16}$$

where $O(k^4a^4)$ is set to zero as the waves are low steepness, and an accurate calculation of this term would require the Stokes expansion of the free surface condition (Whitham, 1962). The rightmost term is numerically evaluated from the output of the model in section 3.3. Hence, equation 4.16 is solved as a cubic to give r under the constraint $0 < r < a$.

Method evaluation

The method was run for $a = 5$, 10, 15, and 20 mm to compare it to the CFD model. Figure 4.6(a) show the reflected wave amplitude of the this momentum model (dot-dashed red with circles), the reflected wave amplitude of the standing wave model (dotted black with squares), and the reflected wave amplitude in the ω frequency bin of the CFD spectral analysis (solid blue with crosses), against the incident wave amplitude. Note that for the momentum method $r = r(\omega)$ because of the model's underlying assumptions. Figure 4.6(b) shows the free surface signal for $a = 15$ mm at $x = -2.00$ m for the momentum model (dot-dashed red) compared against the CFD (solid blue).

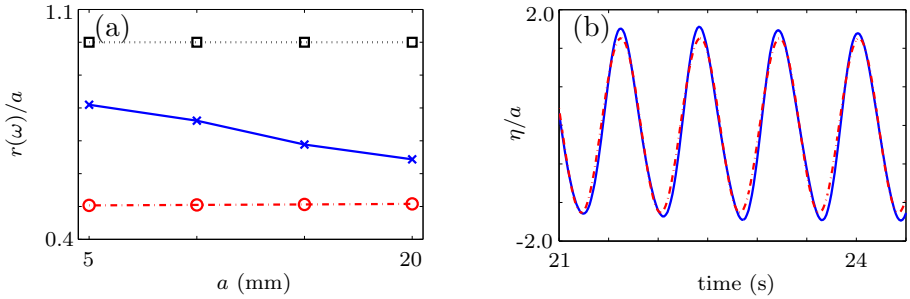

Figure 4.6: (a) Plot of reflected wave amplitude at the fundamental frequency versus incident wave amplitude. (b) Plot of free surface height versus time for $a = 15\,\text{mm}$ at $x = -2.00\,\text{m}$ once periodic motion has been reached in the CFD model. CFD model is in solid blue with crosses, the momentum method is in dot-dashed red with circles, and the standing wave field in dotted black with squares.

Panel (a) shows that, qualitatively, the momentum method is significantly different from the results of the CFD model. The momentum method predicts a reflected wave amplitude between 50 to 51% of the incident wave amplitude, which is significantly less than that of the CFD model. It also predicts a different relationship between $r(\omega)$ and a. The relative difference between the momentum method and the CFD model ranges from 38% for $a = 5\,\text{mm}$ to 22% for $a = 20\,\text{mm}$, with better agreement for larger a. In contrast, the standing wave model predicts a relative difference of 22% for $a = 5\,\text{mm}$ and 55% for $a = 20\,\text{mm}$, which is a similar level of difference to the momentum method. Panel (b) shows that although the signals are qualitatively similar, the amplitude of the momentum method's signal is considerably less than that of CFD model (as indicated by panel a). Therefore, although the momentum method gives a reflected wave amplitude less than the standing wave, it is also significantly less than that found in CFD model, no more accurate than the standing wave field in general, and the relationship between a and $r(\omega)$ is dissimilar.

Physics dictates that the momentum flux of the water below the step's edge must be equal to that of the momentum flux above the step's edge. As this method is unable to produce a valid r for the momentum fluxes to balance, it therefore indicates that the assumption that linear potential theory is holds up until $x = 0$ is invalid. This result is

important for development of the remaining two models.

4.3.3 Energy conservation method for smooth transition region

Method derivation

Consider the control volume C used in section 4.3.1 (the conservation of mass method). Assume there are no energy dissipation effects in the control volume except for the losses due to the bores for $x > 0$, and that the water smoothly transitions from deep water waves to shallow-water flow around the step edge (the validity of this assumption will be tested when the method is analysed). Conservation of energy in C gives

$$\int_C \frac{\partial}{\partial t}\left(\rho_w \frac{1}{2}(u^2+w^2)+\rho_w g z\right)\,\mathrm{d}V + \int_{\partial C}\left(\frac{1}{2}\rho_w(u^2+w^2)+\rho_w g z + p\right)u_{\mathbf{n}}\,\mathrm{d}S - L_{\text{bores}} = 0, \tag{4.17}$$

(Gallavotti, 2002) where $L_{\text{bores}}(t)$ is the energy dissipated by the bores that propagate through the shallow-water domain (Billingham & King, 2000). Physically, the first term is the accumulation of energy in the control volume, the second term is the flux of energy in/out of the control volume and the work done by pressure on the boundary, and the third term is the energy dissipated by the bores.

Under the assumption that the system is cyclical such that there is no net accumulation/loss of energy in C over a wave period, time averaging gives

$$\overline{\int_{\partial C}\left(\frac{1}{2}\rho_w(u^2+w^2)+\rho_w g z + p\right)u_{\mathbf{n}}\,\mathrm{d}S} - \overline{L_{\text{bores}}} = 0. \tag{4.18}$$

As the water's velocity normal to the boundaries are zero, and the velocity of the water relative to the free surface velocity boundary is zero, equation 4.18 gives

$$\begin{aligned}&\overline{\int_{-H}^{\eta}\left(\frac{1}{2}\rho_w(u^2+w^2)+\rho_w g z + p\right)u_{\mathbf{n}}\Big|_{x=L}\,\mathrm{d}z}\\ &+\overline{\int_{0}^{\eta}\left(\frac{1}{2}\rho_w(u^2+w^2)+\rho_w g z + p\right)u_{\mathbf{n}}\Big|_{x=R}\,\mathrm{d}z} - \overline{L_{\text{bores}}} = 0.\end{aligned} \tag{4.19}$$

This implies that, as in the mass method, the assumption that the flow transitions smoothly across the step means that the flow around the step's edge does not need to be calculated in this method.

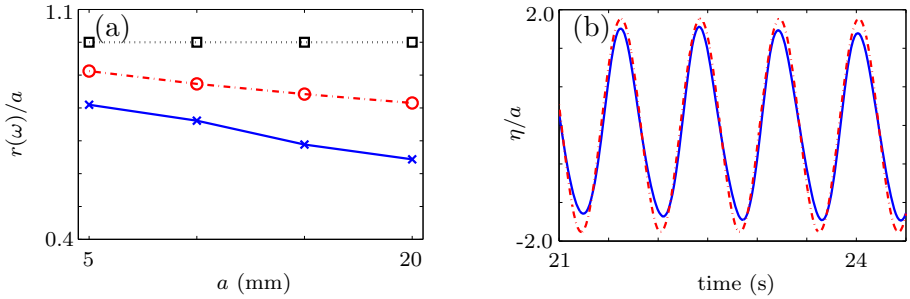

Figure 4.7: As in figure 4.6 but with the smooth transion energy method in dot-dashed red with circles.

Using the same method of evaluating the time-averaged integrals as in section 4.3.1 and 4.3.2, equation 4.19 gives

$$\frac{g^2}{4\omega}(a^2 - r^2) + O(k^4a^4) = \overline{\frac{1}{2}h\hat{u}^3 + gh^2\hat{u}|_{x=R}} - \rho_w^{-1}\overline{L_{\text{bores}}}, \tag{4.20}$$

where $O(k^4a^4)$ is negligibly small (as per earlier methods). The energy dissipated by the bores occurs over the distance they travel (Billingham & King, 2000), thus, by taking the limit as $R \to 0^+$, $\overline{L_{\text{bores}}} \to 0$. Therefore

$$r = \sqrt{a^2 - \frac{4\omega}{g^2}\left(\overline{\frac{1}{2}h\hat{u}^3 + gh^2\hat{u}|_{x=0^+}}\right)}, \tag{4.21}$$

where the rightmost term is calculated numerically from the outputs of the model in section 3.3, which allows r to be solved.

Method evaluation

The method was run for $a = 5$, 10, 15, and 20 mm to evaluate its performance. Figure 4.7 shows the results as in figure 4.6 but for this energy method in dot-dashed red (instead of the momentum method). Figure 4.7(a) shows that this energy method predicts the reflected wave is less than that predicted by the standing wave model, follows the same downwards trend, but is larger than that found in the CFD. The relative difference between this smooth transition energy method and CFD is between 11% for $a = 5$ mm and 26% for $a = 20$ mm. On average the difference is $\sim$ 17%. This is an improvement when compared to the standing wave model, for which the relative difference between CFD and

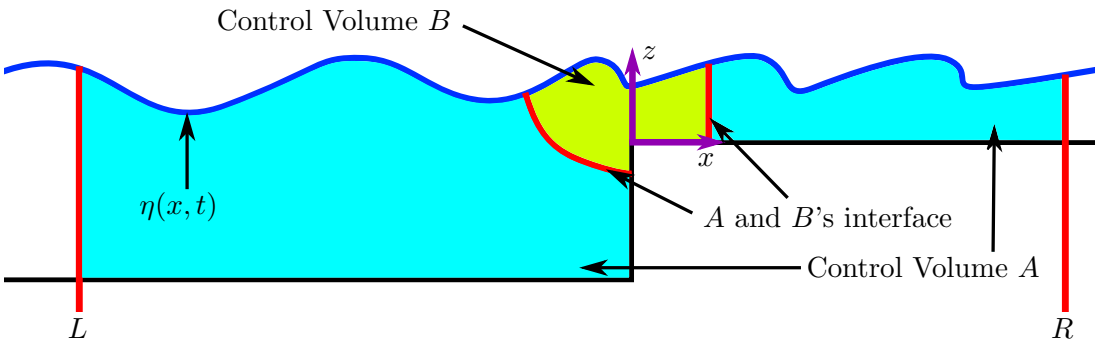

Figure 4.8: Schematic of control volumes of the step for discontinuous transition energy method (not to scale).

standing wave model is 22% for $a = 5\,\text{mm}$ and 55% for $a = 20\,\text{mm}$. Compared to the momentum method of section 4.3.2, this energy method shows better agreement for all cases except when $a = 20\,\text{mm}$ (for which there is only 4% better agreement in the momentum method). Figure 4.7(b) shows that like the momentum method, this energy method has the qualitative properties of the CFD free surface signal for $a = 15\,\text{mm}$ at $x = -2.00\,\text{m}$ in terms of frequency, phase, and shape. However, due to the overprediction of reflected wave amplitude (as indicated in panel a), this energy method produces a noticeably larger signal amplitude.

Although more promising than other models, the dilemma with this method is that it constantly overpredicts the reflected wave amplitude. The method itself is effectively a balance between the energy entering/exiting the domain due to water waves, and the energy entering/existing the domain due to overwash. As it consistently overpredicts r, which correlates to the energy leaving the left-most boundary due to the water waves, it therefore suggests that additional energy losses occur between the $x \ll 0$ and $x > 0$ boundaries. This is the important result for the development of the upcoming method.

4.3.4 Energy conservation method for discontinuous transition

Method derivation

Consider the control volumes A and B shown in figure 4.8. Volume B contains the water near-to the step's edge, volume A contains the water away from the step's edge, and merger of volumes A and B are equivalent to control volume C in figure 4.5. The previous energy

conservation model suggests that there are energy losses inside the control volumes A and B. The results from sections 3.4 and 4.2 suggest that if B is sufficiently large, shallow-water theory and linear potential theory are valid in A. As both these theories are energy conserving (aside from small losses of energy in the shallow-water bores), the additional energy dissipation cannot occur inside A. The momentum conservation model suggests that the water's motion departs from linear potential theory around the vertical wall of the step. This implies that linear potential theory becomes invalid B. The additional energy losses must therefore occur inside B (i.e. near the step's edge), and are because the flow departs from linear potential theory in this region.

It is undesirable to model the transition from deep water waves to shallow-water flow inside volume B in full, because it would add significant complications and take this work outside the scope of linear water wave theory. Instead, recall that the results of sections 3.4 and 4.2 suggest that this region where the models become invalid is relatively small compared to the primary horizontal length scales (i.e. λ and the characteristic length of the bores). As the transition region is small relative to these scales, assume that the region B is sufficiently small such that the volume of B, V_b, can be taken as $V_b \to 0$, but still bounds $0^- < x < 0^+$ and $z > 0$. Under this assumption linear potential flow theory applies for $x < 0$ and shallow-water theory applies for $x > 0$ — implying there is a discontinuity in $\mathbf{u}$, η, and p over $z > 0$ and $x = 0$. Such a description is analogous to hydraulic jumps in shallow-water flow, which are known to dissipate energy (Chanson, 2004), but where the hydraulic jump is the transition from deep water waves to shallow-water flow.

To model the energy of the system with the discontinuity, the first law of thermodynamics for an open system of fluid (or any continuous media) with a jump condition in the domain is employed. The derivation of this form of the first law of thermodynamics can be found in Casey (2011) (particularly useful in this context), or Liu (2013). It is typically derived in such a manner that a condition for energy to be conserved can be obtained by using a modified form of the Reynold's transport theorem. For this problem, however, it is used to measure the energy that is used in the transition from deep water waves to shallow-water flow. In its general form, when applied to an arbitrary control

volume V, with an internal discontinuity over the surface Ω, it is

$$\int_V \frac{\partial}{\partial t} E_t \mathrm{d}V + \int_{\partial V \setminus \Omega} ((E_t + p)\,\mathbf{u} - \mathbf{q}) \cdot \mathbf{n} \mathrm{d}S + \left[\int_\Omega ((E_t + p)\,\mathbf{u} - \mathbf{q}) \cdot \mathbf{n}\, \mathrm{d}S \right]_{\Omega=\Omega^-}^{\Omega=\Omega^+} = 0, \quad (4.22)$$

where E_t is the sum of the kinetic, potential, and internal (i.e. heat related) energy of the system, $\mathbf{q} \cdot \mathbf{n}$ is the heat flux into the system at a point in space, and $\partial V \setminus \Omega$ is the surface of the volume V but excluding Ω. The notation is such that

$$\begin{aligned} \left[\int_\Omega ((E_t + p)\,\mathbf{u} - \mathbf{q}) \cdot \mathbf{n}\, \mathrm{d}S \right]_{\Omega=\Omega^-}^{\Omega=\Omega^+} = &+ \int_{\Omega^+} ((E_t + p)\,\mathbf{u} - \mathbf{q})_{\Omega^+} \cdot \mathbf{n}\, \mathrm{d}S \\ &- \int_{\Omega^-} ((E_t + p)\,\mathbf{u} - \mathbf{q})_{\Omega^-} \cdot \mathbf{n}\, \mathrm{d}S, \end{aligned} \quad (4.23)$$

where Ω^+ denotes the values above the discontinuity and Ω^- denotes the values below the discontinuity. In both $\Omega^\pm$ the normal vector to the surface, $\mathbf{n}$, is taken in the positive x and z direction. Note that, without the third term in equation 4.22 it is the usual form of conservation of energy (Moran *et al.*, 2010), hence the third term is the result of the discontinuity, and is itself a measure of the energy required for the discontinuity to exist.

In C it is assumed that heat transfer effects are negligible, such that $\mathbf{q} = 0$, and changes to the internal energy of the water are negligible, i.e. heating effects are neglected. This latter conditions gives

$$E_t = \frac{1}{2}\rho_w(u^2 + w^2) + \rho_w g z \quad (4.24)$$

as the energy of the water in C (which is now purely the mechanical energy as thermal effects are being neglected). It is also assumed that $x = R$ is sufficiently close to $x = 0$ such that the energy dissipation of the bores can be neglected. This final assumption is not strictly necessary for the derivation, but saves having to model another discontinuity in the water.

Applying equation 4.22 to C gives

$$\int_C \frac{\partial}{\partial t} E_t \, \mathrm{d}V + \int_{\partial C \setminus \Omega} (E_t + p) u_{\mathbf{n}} \, \mathrm{d}S + \int_\Omega [(E_t + p) u_{\mathbf{n}}]_{0^-}^{0^+} \, \mathrm{d}S = 0, \quad (4.25)$$

where Ω is the surface along $x = 0$ and $z > 0$ (i.e. the surface of the discontinuity) with a unit normal in the positive x-direction, $\partial C \setminus \Omega$ is the surface of C excluding Ω with outwards pointing normal, and the square brackets define the operation $[\bullet(x)]_{0^-}^{0^+} = \bullet(x = 0^+) - \bullet(x = 0^-)$ over the discontinuity.

By evaluating this for the boundaries ∂C and $\partial\Omega$, and noting the relative velocity of the fluid at the free surface and basin boundaries are zero, it becomes

$$\begin{aligned}\int_C \frac{\partial}{\partial t} E_t \,\mathrm{d}V = &+ \int_{-H}^{\eta} (E_t + p)u|_{x=L}\,\mathrm{d}z - \int_0^{\eta} (E_t + p)u|_{x=R}\,\mathrm{d}z \\ &+ \int_0^{\eta^-} (E_t + p)u|_{x=0^-}\,\mathrm{d}z - \int_0^{\eta} (E_t + p)u|_{x=0^+}\,\mathrm{d}z\end{aligned} \tag{4.26}$$

where, as in section 4.3.2, $\eta^- = \max(\eta(x = 0^-, t), 0)$. Without the discontinuity over $\partial\Omega$ this would lead to the usual result that the change of energy inside the volume is equal to the energy entering minus the energy existing minus the work done by pressure along the boundary, as presented in Gallavotti (2002) and Moran *et al.* (2010). Therefore, the discontinuity produces the additional two bottom terms, and otherwise is in-fact identical to the smooth transition energy conservation equation (equation 4.17).

As the change of energy inside the system is assumed to be periodic with period T, time averaging equation 4.26 gives

$$\begin{aligned}0 = &+ \overline{\int_{-H}^{\eta} (E_t + p)u|_{x=L}\,\mathrm{d}z} - \overline{\int_0^{\eta} (E_t + p)u|_{x=R}\,\mathrm{d}z} \\ &+ \overline{\int_0^{\eta^-} (E_t + p)u|_{x=0^-}\,\mathrm{d}z} - \overline{\int_0^{\eta} (E_t + p)u|_{x=0^+}\,\mathrm{d}z}.\end{aligned} \tag{4.27}$$

By dividing by the water's density, and using the same integral evaluation process as in section 4.3.1 and 4.3.2, this evaluates to

$$(a^2-r^2)\frac{g^2}{4\omega}+(a-r)(a+r)^2\frac{4g^2k}{6\pi\omega}+O(k^4a^4) = \overline{\left(\frac{1}{2}h\hat{u}^3 + gh^2\hat{u}\right)}_{x=0^+} + \overline{\left(\frac{1}{2}h\hat{u}^3 + gh^2\hat{u}\right)}_{x=R}. \tag{4.28}$$

where, as in previous sections, $O(k^4a^4)$ is negligibly small. As in section 4.3.3, to circumvent the consideration of the energy dissipated by the bore, take $R \to 0^+$, giving

$$(a^2 - r^2)\frac{g^2}{4\omega} + (a - r)(a + r)^2\frac{4g^2k}{6\pi\omega} = 2\overline{\left(\frac{1}{2}h\hat{u}^3 + gh^2\hat{u}\right)}_{x=0^+}. \tag{4.29}$$

As per the other models, the rightmost term in this equation can be calculated using numerical integration from the outputs of the overwash model in section 3.3. This implies equation 4.29 can be solved as a cubic for r where $0 < r < a$.

To aid in physical interpretation, contrast equation 4.29 with equation 4.20, which does not include the effects of the discontinuity. The difference between the two equations is

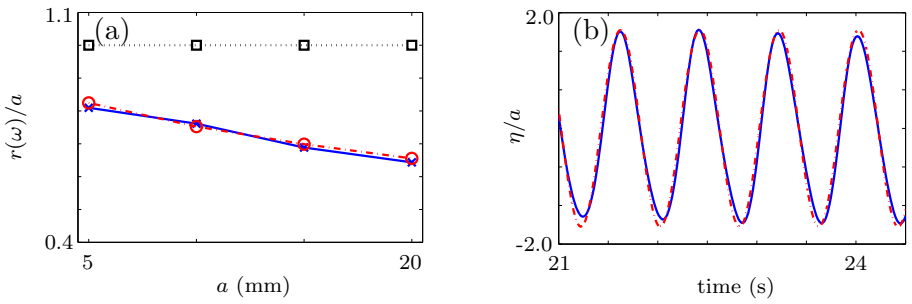

Figure 4.9: As in figure 4.6 but with the discontinuous transition energy method in dot-dashed red with circles.

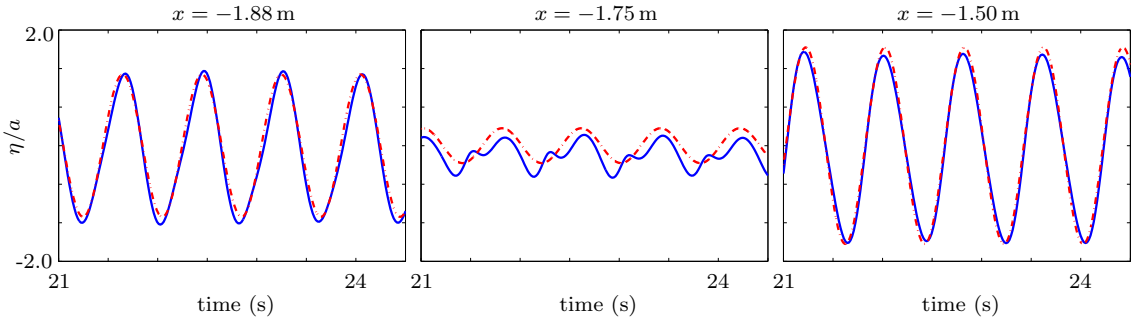

Figure 4.10: Plots of the water's free surface height versus time at $x = -1.88\,\mathrm{m}$, $x = -1.75\,\mathrm{m}$ and $x = -1.50\,\mathrm{m}$ for waves of amplitude 15 mm. CFD model in blue and energy method dot-dashed red.

the centre term and one count of the rightmost term in equation 4.29. Physically, this implies the energy required for the flow to rapidly (i.e. instantaneously) transition from linear water waves to shallow-water flow can be quantified by these two terms. This means that in this model the energy dissipated by the transition is given by

$$E_{\text{transition}} = -(a-r)(a+r)^2\frac{4g^2k}{6\pi\omega} + \overline{\left(\frac{1}{2}h\hat{u}^3 + gh^2\hat{u}\right)}_{x=0^+}. \tag{4.30}$$

Method evaluation

Figure 4.9 is as in figure 4.6 but with the results of this dissipative energy method in dot-dashed red. Panel (a) shows that this method predicts a weakly convex negative relationship between $r(\omega)/a$ and a, which is qualitatively similar to the CFD model. The

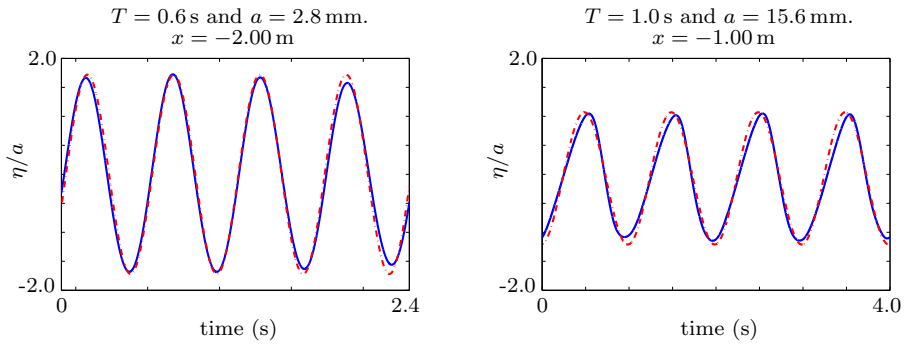

Figure 4.11: Plots of the water's free surface height versus time. Left: For incident waves with $T = 0.6\,\mathrm{s}$ and $a = 2.8\,\mathrm{mm}$ at $x = -2.00\,\mathrm{m}$. Right: For incident waves with $T = 1.0\,\mathrm{s}$ and $a = 15.6\,\mathrm{mm}$ at $x = -1.00\,\mathrm{m}$. CFD model in blue and energy method dot-dashed red.

relative difference between this model and CFD model ranges from 1.9% for $a = 20\,\mathrm{mm}$ to 1.2% for $a = 10\,\mathrm{mm}$. On average the relative difference is 1.6% and the relative difference is always less than 2%. The absolute difference ranges from $0.015r(\omega)/a$ to $0.009r(\omega)/a$. In dimensional terms, this absolute error ranges from 0.08 mm for $a = 5\,\mathrm{mm}$ to 0.38 mm for $a = 20\,\mathrm{mm}$. Hence, for all waves tested, the model is able to accurately predict the reflected wave amplitude at the fundamental frequency.

Figure 4.6(b) as well as figure 4.10 show the free surface signals at $x = -2.00$, -1.88, -1.75, and -1.50 m of the CFD model (solid blue) and this energy model (dot-dashed red), for $a = 15\,\mathrm{mm}$ and $T = 0.8\,\mathrm{s}$. Times are offset such that peaks align at $x - 2.00\,\mathrm{m}$.

At the locations of multiples of 0.5λ (i.e. $x = -2.00$ and -1.50 mm) the models compare well in terms of amplitude, period, and shape. In both these locations the peak to trough difference between CFD and this method is $\sim 3\%$. It is $\sim 1\%$ larger than the relative difference in amplitude for $r(\omega)$, which is due to the small phase difference between reflected and incident waves in the CFD, or the higher frequency waves. At $x = -1.88\,\mathrm{m}$ the signals are again similar, but with a slightly larger difference in amplitude of $\sim 4\%$. Noting that $\lambda = 1.0\,\mathrm{m}$, and the incident and reflected waves are relatively in phase, the larger relative difference is due to greater cancellation between the incident and reflected waves at this location, which makes the higher frequency waves more pronounced. At $x = -1.75\,\mathrm{m}$ the cancellation between incident and reflected wave is strongest. This implies

effect of waves outside the fundamental frequency are most pronounced at $x = -1.75\,\mathrm{m}$, and is why the signals are have a difference between peak to trough distance of 18% and dissimilar shapes there.

While the CFD waves of $T = 0.6$ and $1.00\,\mathrm{s}$ were not analysed in section 4.2 because of the lack of probe locations, their signals are still useful for comparisons here. Figure 4.11 shows the free signals of this energy method (dot-dashed red) compared to the CFD model (solid blue) for (left) waves of $T = 0.6\,\mathrm{s}$ and $a = 2.8\,\mathrm{mm}$ at $x = -2.00\,\mathrm{m}$, and (right) $T = 1.0\,\mathrm{s}$ and $a = 15.6\,\mathrm{mm}$ at $x = -1.00\,\mathrm{m}$. The plots have been aligned such that peaks occur at the same time interval, and $t = 0$ is an arbitrary time when either model is in periodic motion. The difference in probe location between plots is correlated to the wavelength of the respective waves.

The leftmost panel again shows strong agreement between the CFD model and this energy method. At this location $x \approx -3.5\lambda$, and hence the reflected and transmitted wave are relatively in phase. The signals share the same shape and period, although the CFD signal appears to show reduced amplitude for the final wave period. For the first three wave periods the difference in amplitude of the signals $< 2\%$. For the final wave period the difference becomes $\sim 10\%$. The cause of this difference is unknown, but is likely related to additional overwash related nonlinearities. The rightmost panel also shows good, but less strong agreement. The CFD signals are both periodic with period T and have a relative difference in amplitude of $< 6\%$. However, the CFD model's signal is slightly skewed. This is likely due to the location being $x = -0.64\lambda$, which results in more pronounced incident and reflected wave cancellation, and therefore more pronounced higher frequency wave effects. Both panels show the same qualitative properties as for $T = 0.8\,\mathrm{s}$ and therefore indicate that this method's accuracy is not just limited to the $T = 0.8\,\mathrm{s}$ cases, which could be analysed more extensively. As per the $T = 0.8\,\mathrm{s}$ results, they imply this energy method is predicting the reflected wave well, but inaccuracies occur because it does not account for higher frequency effects.

4.4 Summary

The water waves to the left of the step in the CFD model of step were analysed. When overwash did not occur the waves were found to be akin to those predicted by linear potential theory, which produces a standing wave field. When overwash did occur it was found that

1. The waves to the left of the step were found to be invariant of whether a no-shear or no-slip boundary condition was used on the upper surface of the step.

2. The waves were found to be similar when probed at locations $\sim 4\lambda$ and $\sim 0.3\lambda$ to the left of the step, suggesting the non-wavelike effects created by overwash are highly localised.

3. The waves consisted primarily of an incident and reflected wave at the incident wave's frequency, but with a reflected wave amplitude much less than for when overwash did not occur.

4. The phase difference between incident and reflected waves was similar to when no overwash occured.

Four simplified methods for calculating the reflected wave based on conservation principles were considered. The methods were an attempt to correct the wave field used to predict overwash in section 3.3 (which did not include the effect overwash had on the waves to the left of the step) by applying mass, momentum, and energy conservation laws.

The method using conservation of mass was found to be incapable of predicting the reflected wave. This was because linear potential theory predicts that over a wave period the flux of mass is small relative to instantaneous mass fluxes. The method using conservation of momentum was found to be incapable of predicting the reflected wave, and implied that the water behaves differently from linear potential theory around the step's vertical wall. The method that balanced the energy leaving the overwash with the energy entering from the wave field significantly overpredicted the reflected wave amplitude, which indicated that additional energy losses occurred around the step's edge.

The insights gained from these methods were used to develop a conservation of energy model that included energy losses around the step's edge. The energy losses around the step were modelled by assuming the transition from deep water waves to shallow-water flow was sufficiently small such that it could be modelled as occurring instantaneously.

This model was found to show good agreement with the waves produced by the CFD model. The relative difference of $r(\omega)/a$ between the simplified model and CFD model was found to be less than 2% for all incident waves that could be analysed spectrally. The simplified model was also able to accurately reproduce the free surface signals of the water to the left of the step at locations of x outside $\sim -(n/2 + 1/4)\lambda$, where n is an integer. The inability for the model to predict the free surface signals at these locations can be attributed to the cancellation between the incident and reflected wave at these locations, which makes the effect of waves outside the fundamental frequency (not calculated in the energy method) more pronounced.

The chapter demonstrates that the overwash significantly reduces the amplitude, and therefore energy, of waves reflected by a step. It shows that the reduction in energy of this wave field is a combination of the energy of the water washing into the overwash, and the losses associated with the water's transition from deep water waves to shallow-water flow. The reflected waves could be predicted accurately, and simply, by predicting the overwash using the model of section 3.3, and then applying the conservation of energy principles to correct the reflected wave amplitude. This demonstrates that waves reflected by an overwashed step can be modelled without the need for complicated and time expensive CFD software, or more complicated coupling conditions between linear potential and shallow-water theories.

Chapter 5

Wave transmission by an overwashed floating elastic plate

5.1 Introduction

In this chapter a simplified mathematical model of the wave transmission by a moored floating elastic plate is developed. The model uses a method similar to the simplified model in chapter 2 to predict the overwash, and corrects the wave transmission using an energy conservation method like that in chapter 4.

The model is validated using wave tank experiments that were conducted at the University of Melbourne's wave-tank facility. The experiments were conducted similar to those in chapter 2, except plate's width was extended to be near equal to that wave tank; making the experiments essentially two dimensional (one length and one depth). A summary of the experiments and results is contained in the collaboration Nelli *et al.* (2017). Hence, only the salient points for the development of a theoretical model for wave transmission of a floating plate are recounted.

The objectives of this chapter are to:

1. Analyse the experimental findings of the wave transmission by a floating elastic plate in the University of Melbourne experiments.

2. Develop a model for the wave transmission by a moored overwashed floating elastic plate.

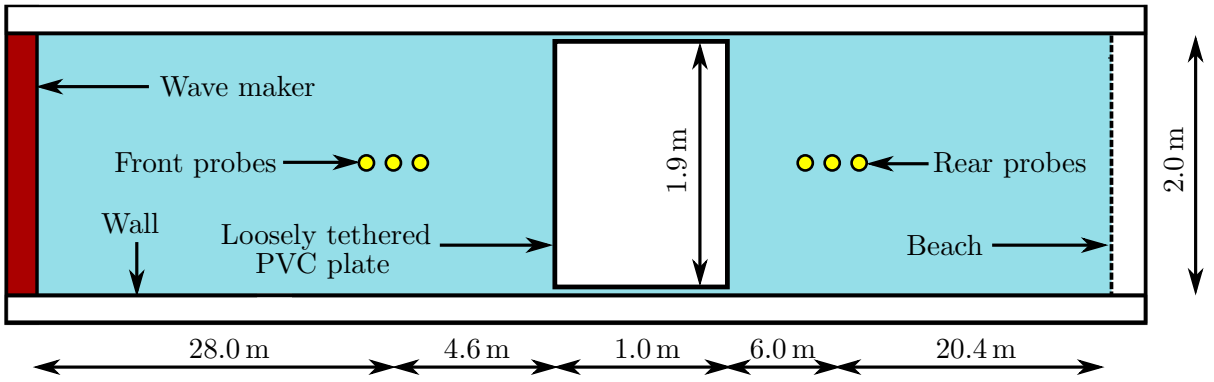

Figure 5.1: Plan view of Melbourne experimental set-up (not to scale).

5.2 Melbourne floating plate experiments

5.2.1 Experimental set-up

The wave-tank was rectangular with a length of 60 m, a width of 2 m, and a flat bed. In-between the wave-maker and beach the basin was filled to a uniform depth of $H = 0.9$ m with water of a density $\rho_w \approx 1000\,\mathrm{kg\,m^{-3}}$. A representative schematic of the experiment is shown in figure 5.1.

Only one kind of plate was used in this round of experiments in order to investigate more incident wave steepnesses, give more repetitions, and because other experimental configurations (not presented here) where used in this experimental campaign. The plate was made of PVC. It had a Young's modulus of $E_p = 500$ MPa, a density of $\rho_p = 570$ $\mathrm{kg\,m^{-3}}$, and Poisson's ratio of $\nu = 0.4$. The plate was placed 28 m downstream from the wave-maker and was loosely tethered, as in the experiments of chapter 2, using long elastic bands to allow it to surge, heave, and pitch naturally, but without drifting down the wave-tank. Its length was $2L = 1$ m, its width was 1.9 m (similar to that of the wave-tank but small enough to prevent friction/collisions between the walls), and its thickness was $d = 10$ mm (to ensure that overwash occurred for most waves tested).

Three depth probes were placed 4.6 m in-front of the plate's upstream edge in order to measure the incident wave and waves reflected by the plate. Three depth probes were placed 6.0 m downstream from the plate's trailing edge in order to measure the transmitted waves. The probes were placed along the centreline of the wave tank and sampled the

water's surface elevation at a frequency of 1000 Hz. The signals were smoothed by filtering frequency components outside of the frequency band 0.5 less than and 4.5 greater than the incident wave period. This was done to remove artificial noise found in post-processing. Both sets of probes were placed sufficiently far from the plate such that they did not detect the localised non-linear effects around the plate's edges that were created by the complicated interaction between overwash and water waves. Therefore, they detected only the wave fields far from the plate.

Depth probes were also located on the plate in order to measure overwash. The probes found the overwash depth to be both qualitatively and quantitatively similar to those found in the experiments of chapter 2. Therefore, the depth readings of these probes will not be presented in this thesis.

The plates were subjected to regular monochromatic incident waves with a wide range of frequencies and steepnesses. In order to simplify discussion the results presented in this chapter will only be for waves of a wavelength $\lambda = 1.0$, 1.3 and 1.5 m (and therefore with $T = 0.8$, 0.9, 1.0 s) with steepnesses $ka = 0.06$, 0.08, 0.10, 0.12, and 0.15. As in previous chapters a is the incident wave amplitude, and k is the positive real root to the dispersion relation $k\tanh(kH) = \omega^2 g^{-1}$, $\lambda = 2\pi/k$, and $g = 9.81\,\mathrm{m\,s^{-2}}$. As with the experiments outlined in chapter 2, these waves are representative of wavelengths similar to the plate's length and steepnesses ranging from gently sloping to more storm like ocean waves. These tests were found to be representative of all steepnesses and periods used in the experiments.

Post-processing of the data found that the wave-maker could more reliably produce regular monochromatic waves of a specified amplitude for higher amplitudes and wavelengths. The choice to analyse the aforementioned periods, as opposed to others, was also influenced by this finding. Post-processing also found that the the wave-maker produced incident waves with steepness approximately ~ 0.002 greater than was intended. Results from experiments will therefore be shown for $ka = 0.062$, 0.082, 0.102, 0.122, and 0.152, but will be discussed without this 0.002 term, for simplicity.

As part of this experimental campaign, plates were also tested with barriers along their edges to prevent the formation of overwash, and without using the tether. The results for these tests will not be discussed here because they do not pertain to the mathematical

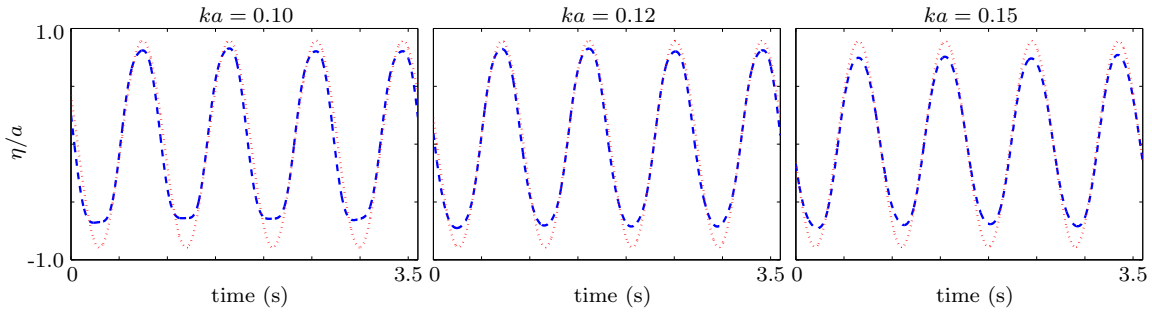

Figure 5.2: Free surface signals scaled by incident wave amplitude for incident waves of $T = 0.9\,\mathrm{s}$ and $ka = 0.10$, 0.12, and 0.15. Signals are taken $\sim 6\,\mathrm{m}$ downstream from the plate's trailing edge. Experimental results in dashed blue, linear potential theory in dotted red.

model that will be developed. Nonetheless, it should be noted that, (i) the analysis of these tests is contained in Nelli *et al.* (2017), and (ii) it was shown that the results for plate's with edge barriers, which prevented overwash from occurring, had good agreement with the predictions of the linear potential theory model presented in section 2.3.1.

5.2.2 Experimental results

Figure 5.2 shows the free surface elevation scaled by the incident wave amplitude of the wave field 6 m downstream from the plate's trailing edge. The time is offset such that $t = 0$ corresponds to an arbitrary point once periodic motion has been reached in the signals. The signals are for incident waves with $T = 0.9\,\mathrm{s}$ and $ka = 0.10$, 0.12, and 0.15, i.e. the three highest steepnesses tested. These steepnesses are presented because it is when the overwash is most pronounced. The results are shown for the experiments (dashed blue), and for the linear potential theory model (that does not include the effects of overwash) of section 2.3.1 (dotted red). The results from linear potential theory are aligned such that the its first peak occurs at the same time as in the experiments.

The peak to trough difference of the experimental signals is $1.47a$, $1.53a$, and $1.45a$ for $ka = 0.10$, 0.12, and 0.15, respectively. The peak to trough difference of the linear potential theory model is $\sim 1.84a$, and is constant for all waves due to the linearity of the model. The relative difference between model and experiment is therefore between

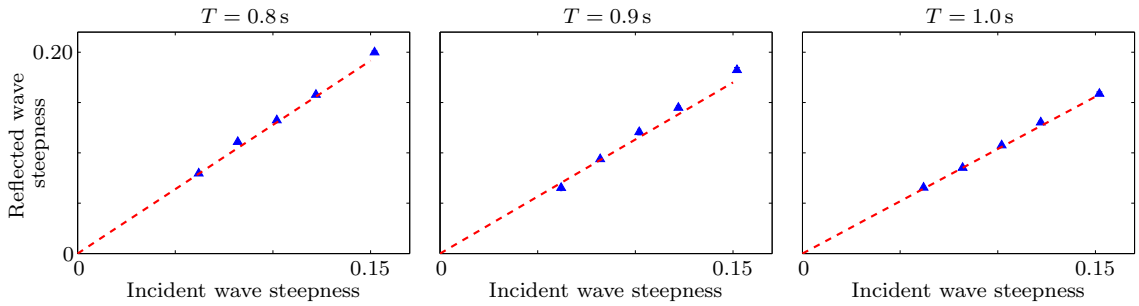

Figure 5.3: Wave steepness upstream from the plate versus incident wave steepness for 10 mm thick PVC floating plate experiments. Experimental results in blue triangles and linear potential theory in dashed red.

20% and 27%. This is a symptom of the reduced transmission due to overwash. The shape of the experimental signals are generally similar to that of linear theory, with both models having one peak and one trough per wave period. The shape of the experimental signals around their peaks and troughs, however, are distorted from that of linear theory. This is particularly prevalent in the troughs of the signal for $ka = 0.10$. The distortion in the signal is because the transmitted waves are more widely distributed across the frequency spectrum (demonstrated in greater detail in Nelli *et al.*, 2017) than in the linear model, which assumes wave transmission is only at the incident wave's (fundamental) frequency. These results are representative of all incident wave periods and steepnesses tested, however, certain rouge cases found more distortions of the signal than in $ka = 0.10$, thereby emphasising the nonlinear effects of the overwash.

Wave steepness was calculated using the zero order crossing method. This method is the standard procedure for spectral analysis of water waves (see e.g. Thomson & Emery, 2014), and further details can be found in Nelli *et al.* (2017). The analysis method produces uncertainties due to the discretisation of the fast Fourier transform of the signals. In all cases the relative uncertainty in the experimental results is less than 2%. As the uncertainty is small, and for simplicity, results will be discussed without consideration of it.

Figure 5.3 shows the steepness of the wave field upstream from the plate against the incident wave steepness. Experimental results are shown in blue triangles (note that the blue triangles contain error bars for the uncertainty in the steepness calculation and are

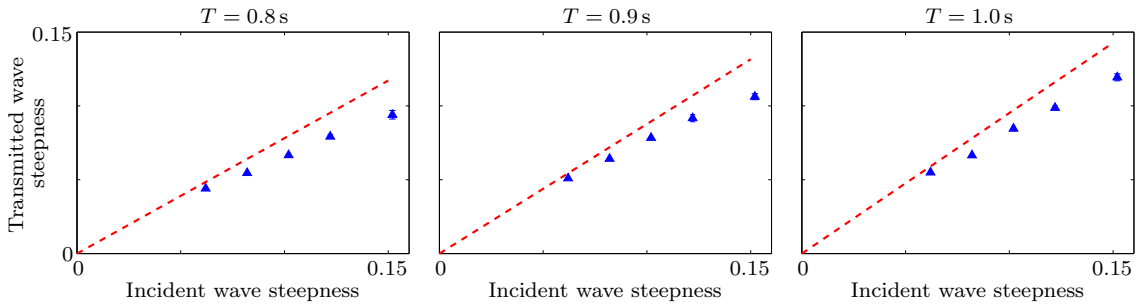

Figure 5.4: As in 5.3 but for the steepness of waves downstream from the plate.

presented to emphasise the relative uncertainty is negligibly small), and linear potential theory in dashed red.

For all T, the steepness of the incident and reflected waves is roughly linear with respect to ka. Excluding the outlier for $T = 0.9\,\mathrm{s}$ and $ka = 0.15$, the agreement between linear potential theory and experiments is always remains within $\sim 6\%$, and is generally much better than that. For the single outlier, it remains within $\sim 8\%$. This indicates that linear potential theory provides a good approximation of the wave field upstream from the plate. This result is likely due to the fact the amplitude of the wave reflected by the plate is small relative to the incident wave amplitude (which can be shown using the model in section 2.3.1). It also implies that the waves reflected by the plate are relatively unperturbed by overwash.

Figure 5.4 is as in 5.3 but for the wave field downstream from the plate. For $ka = 0.08$, where a relatively small amount of overwash occurs, the difference between experiments and linear model is as little as $\sim 6\%$. In contrast, for $ka = 0.15$, where the deepest and most energetic overwash occurs, the linear model overpredicts wave transmission by $\sim 25\%$. The trend in experimental results is sub-linear, and is therefore markedly different to the linear trend predicted by linear potential theory. The figure therefore demonstrates that overwash does significantly reduce wave transmission, and in a non-linear manner (note that in Nelli *et al.*, 2017, the transmission was found to be linear with respect wave amplitude when barriers were installed around the plate's edges). Further, by considering the findings of chapter 2, the reduction in transmission is correlated to cases of deeper and more energetic overwash.

5.3 Dissipative energy method for wave transmission

An energy method similar to that of chapter 4 is developed in order to predict the wave transmission past the overwashed plate. Following the methodology of the model in section 4.3.4, the model consists of two stages. Stage one predicts the energy transferred into the overwash at the plate's edges, and stage two corrects the wave transmission given by linear potential theory using energy conservation principles.

5.3.1 Stage 1 - Overwash prediction

Consider the two dimensional floating plate geometry outlined in section 2.3. Assume that the water on the plate is shallow such that it obeys the shallow-water equations for $-L < x < L$ and $z > z_b$. Assume that linear potential theory (i.e. the model of section 2.3.1) can calculate the motion of the upper surface of the plate (z_b), the water's free surface (η), and the water velocity ($\mathbf{u}$) accurately enough to force the overwash at the plate's edges ($x = \pm L$). The validity of these assumptions was demonstrated in chapter 2, if bore collisions did not occur on the plate, for linear potential theory with and without evanescent waves. In this section the model without evanescent waves is used the provide the boundary conditions for the overwash, as it is the simpler description.

Two, additional, key assumptions to the overwash model of chapter 2 are made in order to apply the wave correction methodology of section 4.3.4 to the floating elastic plate problem. Firstly, assume (i) that the energy transferred into the overwash does not return to the surrounding system. Secondly, assume (ii) that the water overwashed onto the plate's edges is unaffected by the water already present on the plate. The first assumption is made because the overwash is nonlinear and therefore unlikely to feedback into the surrounding system smoothly and coherently enough to produce waves at the fundamental frequency. The second assumption, which is made to overcome the errors created by bore collisions, is motivated by visualisations of the experiments in chapter 2. These visualisations are presented in Appendix D. They show that even if bore collisions occur on the plate, the water breaks onto the edges similar to if no water is on the plate's edges, because the water around the plate's edges is relatively shallow before the overwash forms.

With these key assumptions the overwash at one plate edge is forced independently of the overwash at the other edge. Thus, the overwash at each edge is simulated separately. Each set of simulations uses the shallow-water equations to model the water on the plate, which is solved using the numerical method in Appendix B. To obtain the energy fluxes at the plate's upstream edge, the first round of edge predictions are run using the edge boundary conditions

$$h(-L^-,t) = \max\left(\eta(-L^-,t) - z_b(-L,t), 0\right), \quad \text{and} \tag{5.1}$$

$$\hat{u}(-L^-,t) = \begin{cases} \partial_x\phi(-L^-,0,t) & \text{if } z_b(-L^-,t) > 0, \text{ or} \\ 0 & \text{otherwise,} \end{cases} \tag{5.2}$$

(like those in section 2.3.2) in order to model the overwash forcing by the water waves at the plate's upstream edge. To model the water washing freely outwards, radiation conditions are set such that

$$h(x = F,t) = \hat{u}(x = F,t) = 0, \tag{5.3}$$

where $F \gg -L$. Numerical testing found that by using $F \geq L$ (or potentially much smaller) the energy flux into the overwash at $x = -L^+$ was invariant of this condition. Therefore, the model presented here uses $F = L$.

From this simulation the results for energy entering the overwash at $x = -L^+$ are obtained. That is, they determine $\rho_w(\frac{1}{2}h\hat{u}^3 + gh^2\hat{u})|_{x=-L^+}$ once periodic motion occurs in the overwash at $x = -L^+$. Numerical testing found that periodic motion always occurred after ~ 5 incident wave periods.

The second round of edge predictions are run using similar edge boundary conditions, but at the downstream edge of the plate. These are

$$h(L^+,t) = \max\left(\eta(L^+,t) - z_b(L,t), 0\right), \quad \text{and} \tag{5.4}$$

$$\hat{u}(L^+,t) = \begin{cases} \partial_x\phi(L^+,0,t) & \text{if } z_b(L^+,t) > 0, \text{ or} \\ 0 & \text{otherwise.} \end{cases} \tag{5.5}$$

As well as

$$h(-L,t) = \hat{u}(-L,t) = 0 \tag{5.6}$$

as the radiation condition. From this simulation the results for energy entering the overwash at $x = L^-$ are obtained, i.e. $\rho_w(\frac{1}{2}h\hat{u}^3 + gh^2\hat{u})|_{x=L^-}$ once periodic motion is reached. Again, this was found to occur after ~ 5 incident wave periods.

5.3.2 Stage 2 - Wave transmission correction

Assume the plate's vertical displacement and accelerations are small such that the energy fluxes calculated at the plate's edges, $(\frac{1}{2}h\hat{u}^3 + gh^2\hat{u})|_{x=-L^+}$ and $(\frac{1}{2}h\hat{u}^3 + gh^2\hat{u})|_{x=L^-}$, in the previous section are accurate when the overwash is periodic at the boundaries. This assumption is motivated by the findings of the simplified model of overwash of a step in chapter 3. Further, under assumption (i), assume that the energy leaving these boundaries can be modelled as being removed entirely from the surrounding wave fields.

Assume the overwash and surrounding water's motion are periodic at the incident wave's period, T. Motivated by the findings of figures 5.3 and 5.4, assume that for $x \ll -L$ and $x \gg L$ the water obeys linear potential water wave theory, but with some unknown transmitted wave amplitude, and assume that the affects outside the fundamental frequency are negligible. Further, as motivated by the findings of figure 5.3, assume that overwash does not change the wave reflection from the plate predicted by linear potential theory. Hence, when taking only the real components of the velocity potentials in section 2.3.1, the wave field to the left of the right of the plate is given by

$$\phi(x,z,t) = (|A|\sin(\omega t - kx) + |R_0|\sin(\omega t + kx + \theta_R))\frac{\cosh(k(z+H))}{\cosh(kH)} \tag{5.7}$$

for $x \ll -L$ and $-H < z < \eta$, and

$$\phi(x,z,t) = |T|\sin(\omega t - kx + \theta_T)\frac{\cosh(k(z+H))}{\cosh(kH)} \tag{5.8}$$

for $x \gg L$ and $-H < z < \eta$.

For equation 5.7, $A = -g\omega^{-1}a$, θ_R is the phase difference between the incident and reflected wave, and R_0 is given by linear potential theory (calculation shown in section 2.3.1), which relates to the reflected wave amplitude, r, via $|R_0| = -g\omega^{-1}r$. For equation 5.8, $T = -g\omega^{-1}\tau$, τ is the, now unknown, transmitted wave amplitude, and θ_T is the phase difference between the incident and transmitted wave.

Assume θ_R is that given by potential theory, i.e. $\theta_R = \arg(R_0) + \pi/2$, because the Melbourne experiments showed wave reflection was invariant of overwash. Assume θ_T is equal to that from linear theory, i.e. $\theta_T = \arg(T_0) + \pi/2$, because the phase of the wave reflected by a step was similar to that without overwash (note, however, that neither of these phase assumptions are used in the preceding derivation, and their validity is therefore untested).

As the water is assumed to obey linear potential theory, this also implies that its pressure is given by the unsteady Bernoulli equation,

$$p = -\rho_w \partial_t \phi - \rho_w g z - \frac{1}{2}\rho_w \left(u^2 + w^2\right), \tag{5.9}$$

for $|x| \gg L$ and all z, and the free surface is obtained via the linearised free surface condition,

$$\eta = \frac{-1}{g}\partial_t \phi, \tag{5.10}$$

for $|x| \gg L$ and all z. Further, for simplicity, as the experiments had water deep enough such that $\tanh(kH) = 1.00$ (i.e. accurate to three significant figures), take the deep water approximation $\tanh(kH) = 1$. This gives the dispersion relation as $k = \omega^2 g^{-1}$.

Motivated by the findings of chapter 4, assume the transition between linear water waves to shallow-water flow is small relative to the characteristic bore lengths and incident wave's wavelength. Hence, the flow parameters $\mathbf{u}$, η, and p, are modelled as being discontinuous over $x = -L$ and $x = L$ for $z_b(x = \pm L) < z < \eta(x = \pm L)$, respectively, as the water transitions from deep water waves to shallow-water flow. This assumption also implies that equations 5.7 and 5.8 are considered to be valid up to, but not including, $x = -L$ and $x = L$, respectively.

Under these assumptions the same process as used in section 4.3.4 is applied to balance the energy leaving the system and the energy dissipated as the water transitions from deep water waves to shallow-water flow. This balance is derived in Appendix E, and results in

$$\begin{aligned} 0 = &+ \overline{\int_{-H}^{\eta} Eu|_{x=x_L}\,\mathrm{d}z} - \overline{\int_{-H}^{\eta} Eu|_{x=x_R}\,\mathrm{d}z} \\ &+ \overline{\int_{z_b}^{\eta^-} Eu|_{x=-L^-}\,\mathrm{d}z} - \overline{\int_{z_b}^{\eta} Eu|_{x=-L^+}\,\mathrm{d}z} + \overline{\int_{z_b}^{\eta} Eu|_{x=L^-}\,\mathrm{d}z} - \overline{\int_{z_b}^{\eta^+} Eu|_{x=L^+}\,\mathrm{d}z} \\ &- \overline{\int_{z_b}^{\eta} Eu|_{-L^+}\,\mathrm{d}z} + \overline{\int_{z_b}^{\eta} Eu|_{L^-}\,\mathrm{d}z}, \end{aligned} \tag{5.11}$$

where $x_L \ll -L$, $x_R \gg L$, $\eta^{\pm} = \max(\eta(x = \pm L^{\pm}) - z_b(x = \pm L), 0)$, (slightly modified from chapter 4 to include plate motion), and $E(x, z, t)$ is the density and velocity scaled energy flux at a point. It is given as

$$E = \frac{1}{2}(u^2 + w^2) + gz + \frac{p}{\rho_w}. \tag{5.12}$$

Following the interpretation of the waves reflected by of an overwashed step, the physical interpretation of equation 5.11 is as follows. The first line is the balance between energy entering and leaving the domain via the linear water waves. The second line corresponds to the energy lost due to the transition between linear water waves to shallow-water flow. The bottom line is the energy flowing onto the plate at the overwashed edges, which is assumed to be removed from the system as a whole, under key assumption (i).

In actual practice the water in the floating plate system cannot penetrate side surfaces of the plate. This implies that for $z_b - d < z < z_b$, $u(\pm L^{\pm}) = 0$. This boundary condition was not included in the linear model, for simplicity, and because $d \ll H$, i.e. it constitutes a relatively small part of the domain. However, in this model, having $u(\pm L^{\pm}) \neq 0$ produces the first and last terms in the second line of equation 5.11. These terms are cumbersome to calculate because of the complicated relationship between z_b, $\mathbf{u}$, p, and η at the plate's edges. To remove the need to implement these complicated calculations, and to better reflect actual practice where $u(\pm L^{\pm}) = 0$ for $z = z_b^-$, in equation 5.11 the approximation $u(\pm L^{\pm}) = 0$ for $z_b < z < \eta$ is made. This gives

$$-\overline{\int_{-H}^{\eta} Eu|_{x=x_L}\,\mathrm{d}z} + \overline{\int_{-H}^{\eta} Eu|_{x=x_R}\,\mathrm{d}z} = -2\overline{\int_{z_b}^{\eta} Eu|_{x=-L^+}\,\mathrm{d}z} + 2\overline{\int_{z_b}^{\eta} Eu|_{x=L^-}\,\mathrm{d}z}. \tag{5.13}$$

Using the velocity potentials for $x \ll -L$, $x \gg L$ (equations 5.7 and 5.8, respectively) equation 5.13 evaluates to

$$\frac{g^2}{4\omega}(-a^2 + r^2 + \tau^2) = -2\overline{\left(\frac{1}{2}h\hat{u}^3 + gh^2\hat{u}\right)\Big|_{x=-L^+}} + 2\overline{\left(\frac{1}{2}h\hat{u}^3 + gh^2\hat{u}\right)\Big|_{x=L^-}}, \tag{5.14}$$

plus higher order terms proportional to k^4a^4, which are not included because their calculation requires the Stokes expansion of the linear free surface condition. Upon rearrangement, the transmitted wave amplitude is therefore calculated as

$$\tau = \sqrt{a^2 - r^2 + \frac{8g^2}{\omega}\left[\overline{\left(\frac{1}{2}h\hat{u}^3 + gh^2\hat{u}\right)}\right]_{x=-L^+}^{x=L^-}}, \tag{5.15}$$

where the overlined term is evaluated numerically from the output of the overwash prediction stage.

Supplementing this, considering that in the linear model energy is conserved, $\tau_{\mathrm{LPT}}^2 = a^2 - r^2$, where τ_{LPT} is the transmitted wave amplitude given by linear potential theory without overwash. This implies that equation 5.15 relates the transmitted wave amplitude with overwash, to the transmitted wave amplitude without overwash, as

$$\tau = \sqrt{\tau_{\mathrm{LPT}}^2 + \frac{8g^2}{\omega}\left[\overline{\left(\frac{1}{2}h\hat{u}^3 + gh^2\hat{u}\right)}\right]_{x=-L^+}^{x=L^-}}. \tag{5.16}$$

5.3.3 Summary of wave transmission model

To better exemplify the ease in which this model can be applied as an extension of existing linear potential theory (one of the primary goals of this research), from a general perspective the sages of the model are outlined as follows.

1. Run the linear potential theory model of a floating elastic plate to calculate the values of r, θ_R, τ_{LPT}, θ_T, η, u, and z_b.

2. Run the shallow-water equation solver using the values of u, η and z_b from linear potential theory at the upstream edge, and $\hat{u} = h = 0$ sufficiently far downstream. This gives the mean energy flux into the overwash over a wave period at the upstream edge, $\overline{(\frac{1}{2}h\hat{u}^3 + gh^2\hat{u})}|_{x=-L^+}$.

3. Run the shallow-water equation solver using the values of u, η, and z_b from linear potential theory at the downstream edge and $\hat{u} = h = 0$ sufficiently far upstream. This gives the mean energy flux into the overwash over a wave period at the downstream edge, $\overline{(\frac{1}{2}h\hat{u}^3 + gh^2\hat{u})}|_{x=L^-}$.

4. Calculate the modified transmitted wave amplitude due to overwash as

$$\tau = \sqrt{\tau_{\mathrm{LPT}}^2 + \frac{8g^2}{\omega}\left[\overline{\left(\frac{1}{2}h\hat{u}^3 + gh^2\hat{u}\right)}\right]_{x=-L^+}^{x=L^-}}. \tag{5.17}$$

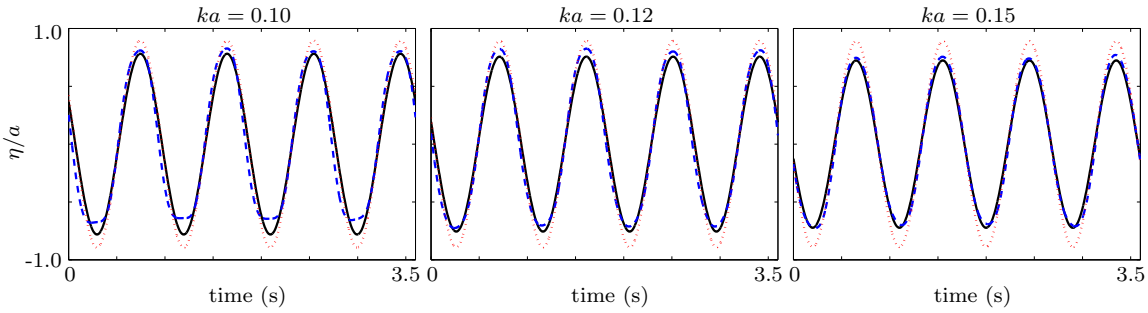

Figure 5.5: As in figure 5.2 but with mathematical model results overlaid in solid black.

5.4 Experiment and model comparisons

The wave transmission model was run using the same plate properties and incident waves as in the experiments of section 5.2 in order to compare it to these experiments. The model ran in less than $300T$ real-world seconds. The majority of this time was spent ensuring periodic motion occurred in the overwash at the plate's edges. It is likely that the time performance could be improved by optimising the mesh sizes in the shallow-water solver, or by better optimising the location of the $h = \hat{u} = 0$ radiation condition; although this was not investigated further.

Figure 5.5 is as in figure 5.2, but with the results of the mathematical model for the transmitted wave 6 m downstream from the the plate's downstream edge overlaid in solid black. For $ka = 0.12$ and 0.15 the peak to trough distance of the mathematical model is $1.51a$ and $1.45a$, respectively, and the peak to trough distance of the experiments is $1.53a$ and $1.45a$, respectively. The relative difference in peak to trough distance is therefore $\sim$ 1.5% for $ka = 0.12$, and $\sim$ 0.0% for $ka = 0.15$. For $ka = 0.12$ and 0.15, the shape of the signals is almost identical, with the only substantial difference between experiments and mathematical model being a vertical shift of $\sim 0.11a$, potentially due to small errors in probe calibration or the depth of the water in the wave-tank. For $ka = 0.10$ the peak to trough distance of the experimental model is $1.56a$, and the experimental signal's peak to trough distance is $1.48a$. The relative difference is therefore $\sim$ 5.4%. The larger difference for $ka = 0.10$ is because the mathematical model does not contain the distortions about the troughs found in the experiment. As discussed in section 5.2.2, these distortions are due the spread of the transmitted waves across the frequency spectrum, which are not

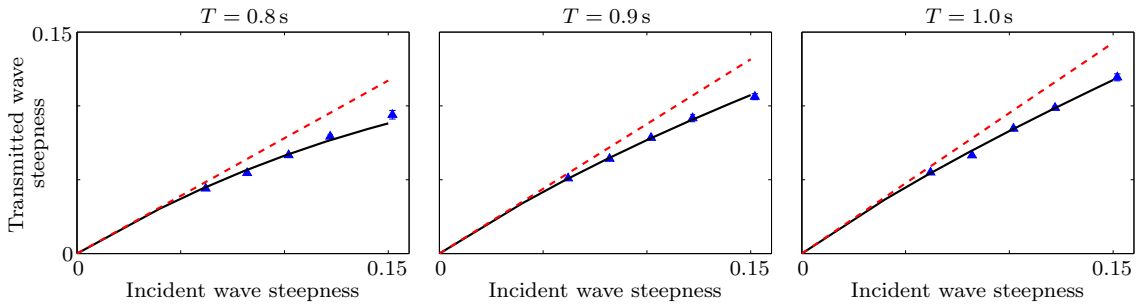

Figure 5.6: As in 5.4 but with the mathematical model overlaid in solid black.

included in the simplified model.

Figure 5.6 is as in figure 5.4 but with the steepness of the transmitted waves in the mathematical model (calculated as τk) in solid black. For $ka < 0.04$, when overwash was not found to occur, it shows that the mathematical model agrees with linear potential theory, as expected. For $ka > 0.04$, it shows the same trend as found in experiments, where higher incident wave steepnesses result in lower transmitted wave steepness.

For $T = 1.0\,\mathrm{s}$, the model and experiment show strong agreement, with a maximum relative difference of 3.8% (for $ka = 0.06$), a minimum relative difference of 1.6% (for $ka = 0.15$), and an average relative difference of 2.3%. For $T = 0.9\,\mathrm{s}$, the agreement is similar, with a maximum relative difference of 3.3% (for $ka = 0.06$), a minimum relative difference of 1.1% (for $ka = 0.15$), and an average relative difference of 2.0%. For $T = 0.8\,\mathrm{s}$, the agreement is weaker, but still strong. For $T = 0.8\,\mathrm{s}$ the maximum relative difference is 6.2% (for $ka = 0.15$), the minimum relative difference is 0.5% (for $ka = 0.10$), and the average difference is 2.8%. Post-processing found that for the two repetitions of the $T = 0.8\,\mathrm{s}$ and $ka = 0.15$ experiment the incident wave steepness was $\sim 8\%$ larger than specified. The $T = 0.8\,\mathrm{s}$ and $ka = 0.15$ test therefore appears as an outlier because of this. Across all tests the the average relative difference was 2.4% and, excluding the point where $T = 0.8$ and $ka = 0.15$, the relative difference between experiment and model was always within 4.1%. The model therefore agrees well with the experiments in terms of transmitted wave steepness, although agreement is generally better for higher incident wave steepnesses or periods.

As the transmitted wave field is periodic with the same period as the incident waves, the energy flux of the transmitted wave field, E_{trans}, is calculated as a portion of the

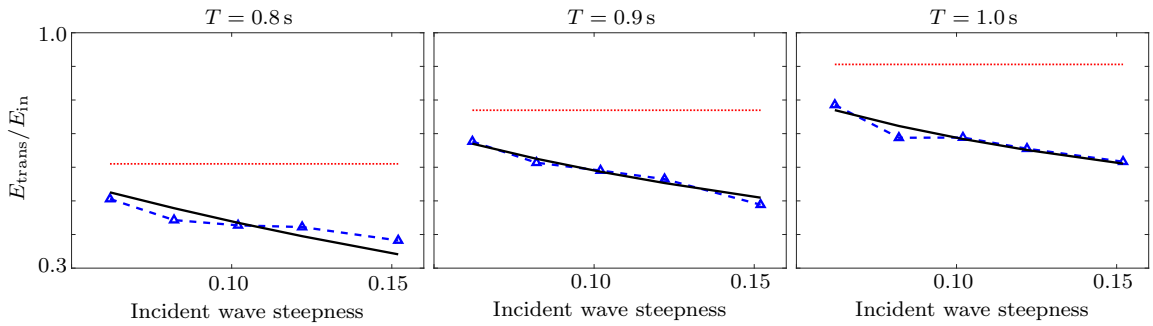

Figure 5.7: Energy of wave transmitted past the floating elastic plate as a portion of incident wave energy. Experimental results in blue triangles, linear potential theory in dotted red, and mathematical model in solid black.

incident wave energy flux, E_{in}, as $E_{\mathrm{trans}}/E_{\mathrm{in}} = (\text{Transmitted wave steepness})^2/(ka)^2$, for linear potential theory, mathematical model, and experiments (Holthuijsen, 2010). Figure 5.7 shows this energy flux ratio against the incident wave steepness for $T = 0.8$, 0.9, and 1.0 s, for experimental results (blue triangles with dashes), linear potential theory in (dotted red), and mathematical model (solid black).

Across all cases it demonstrates that linear potential theory significantly overpredicts the energy in the transmitted waves found in experiment. The errors between linear potential theory and experiments range from $\sim 16\%$ to 47%, and the largest errors are found for the highest steepness incident waves. In contrast, for all T and ka, the mathematical model predicts a smooth downwards trend that is similar to experiments, but without as much scatter.

For $T = 1.0\,\mathrm{s}$ the experiments closely follow the mathematical model's curve, but with weakest agreement for $ka \leq 0.08$. For $ka \leq 0.08$ the average relative difference is 3.5%, and for $ka \geq 0.10$ the relative difference is always within 1.0%. For all ka and $T = 1.0\,\mathrm{s}$, the average relative difference is 1.9%. For $T = 0.9\,\mathrm{s}$ the experiments follow the mathematical model's curve, but with more pronounced scatter around this curve. For this period the worst agreement is for $ka = 0.15$, where the relative difference is 4.3%, and for all other cases the relative difference is within 2.1%. Across all cases the average relative difference for $T = 0.9\,\mathrm{s}$ remains $< 2.0\%$. For $T = 0.8\,\mathrm{s}$, the agreement is not as strong. The experimental results tend to follow the mathematical model's curve, but with

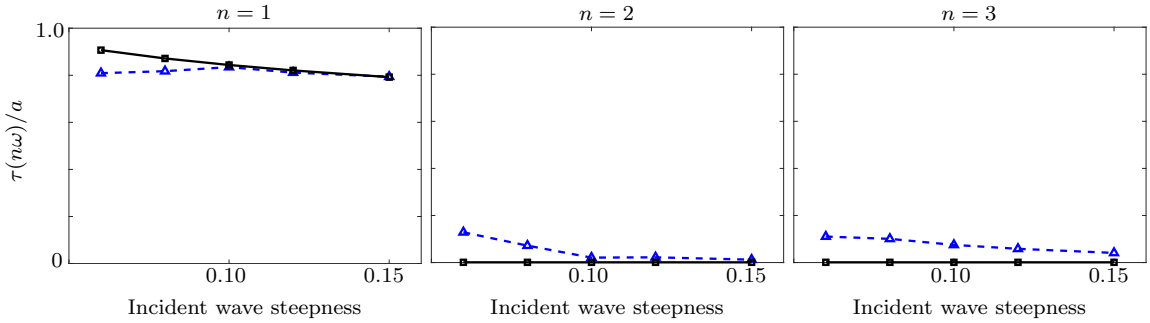

Figure 5.8: Amplitude of transmitted wave signal at frequency bins centred at ω, 2ω and 3ω as a portion of incident wave amplitude. Mathematical model in solid black with squares and experiments in dashed blue with triangles.

the most prevalent scatter around the curve. For $ka = 0.08$ and $ka = 0.15$ the agreement is at its weakest, with a relative difference of 11% and 8.0%, respectively. For other the other incident steepnesses the relative differences is within 6.5%. For $T = 0.8\,\mathrm{s}$ and all ka the average relative difference is $\sim 6.2\%$. The model, therefore, predicts the energy fluxes of the transmitted waves well, however, agreement is generally worse for lower ka or T.

To better understand the less strong agreement for certain T and ka, the free surface signals of the probe 6 m downstream from the plate were analysed in the frequency domain using the the fast Fourier transform. The signals were analysed over five wave periods once periodic motion had been attained. Hence, the amplitude of the signal was placed in frequency bins with width 0.25ω centred at $n\omega$, where $n = 0.25$, 0.50, 0.75, etc.

Figure 5.8 shows these spectral amplitudes, $\tau(n\omega)$, of the experiments (dashed blue) and simplified model (solid red), at the frequency bins centred at $n\omega$ for $n = 1$, 3, and 3, as a function of incident wave steepness, for waves with $T = 1.0\,\mathrm{s}$. Results are presented for the first three multiples of the fundamental frequency because outside of these frequency bins, $\tau(n\omega)$ was always an order of magnitude or less than a.

The plots show that the cases where higher order effects are more pronounced are directly correlated to worse agreement in figure 5.7. For $n = 1$, and $ka = 0.06$ and 0.08, the relative difference between model and experiment is 12% and 6%, respectively. In comparison, for $n = 1$ and $ka \geq 0.10$ the relative difference is always within 1.1%. For $n = 2$, the $ka \leq 0.08$ experimental cases have a $\tau(n\omega)/a$ of 0.13 and 0.07, whereas

for $ka \geq 0.10$ $\tau(n\omega)/a$ is less than 0.02. For $n = 3$ the same trend is noticed where $ka \leq 0.08$ has a larger $\tau(n\omega)/a$ than for $ka \geq 0.10$. This implies that for $ka = 0.06$ and 0.08 the transmitted waves outside the fundamental frequency, which are not included in the simplified model, are more pronounced. In comparison with figure 5.7, these cases are also when the largest difference between the simplified model and experiments are observed. For $T = 0.8\,\mathrm{s}$ and $T = 0.9\,\mathrm{s}$ it was also found that the agreement between model and experiment in figure 5.7 was weakest when $\tau(n\omega)/a$ for $n = 2$ and 3 was largest. Furthermore, higher frequency effects were generally, although not necessarily, more likely to occur for smaller a and T — the cause of the worse agreement for $T = 0.8\,\mathrm{s}$. This implies that when there is weaker agreement between the mathematical model and experiments, it is because the mathematical model does not include the higher frequency transmitted waves.

5.5 Summary

The waves transmitted by an overwashed floating plate subjected to regular monochromatic waves was investigated using experiments at the Univeristy of Melbourne's wave-tank facility. The experiments found that the wave transmission past the floating elastic plate was significantly less than that predicted by linear potential theory. They also showed that the wave field upstream from the plate was predicted well by linear potential theory.

A model for wave transmission was developed using the methodology for wave reflected by an overwash of step (section 4.3.4). Its key assumptions were that the energy entering the overwash does not return to the surrounding waves, and that the overwash formed at the edges of the plate can be predicted without considering the overwash already on the plate. The method was used to correct the transmitted wave amplitude predicted by linear potential theory by taking into account the energy entering the overwash, and the energy required for the water to transition from deep water waves to shallow-water flow. The method results in a procedure that can be applied as an extension of linear potential theory, and was able to run in $\sim 300T$ real world seconds.

The model compared well with experiments. It was able to accurately reproduce the depth signals downstream from the plate, the steepness of the transmitted wave field, and

the energy of the transmitted waves. However, the accuracy of model was reduced when the overwash produced more pronounced higher frequency waves. Generally, this implied the model was less accurate for lower T or ka.

The results demonstrate that although overwash itself is a non-linear process, and the relation between incident and transmitted wave field of an overwashed plate is non-linear, the wave field surrounding the plate can still be modelled well by linear water waves. They also demonstrate that this can be done validly, and simply, by using the mathematical model presented.

Chapter 6

Conclusions

In the first phase of this investigation (chapters 2 and 3) a simplified mathematical model was developed to predict the overwash onto a floating elastic plate and the overwash onto a step. In both instances the overwash was forced by monochromatic water waves. The models used linear potential flow theory to model the surrounding water and body motion and the nonlinear shallow-water equations to model the overwash. The key assumption in these models was that overwash could be forced without consideration of how it perturbs the surrounding waves. The model of the floating elastic plate was compared to the overwash found in wave-tank experiments of a floating elastic plate. The model of the step was compared to the overwash predicted by a CFD model. By comparing the mathematical model of the floating elastic plate to the experiments it was found that:

1. Linear potential theory predicts the onset of overwash well.

2. The models and experiments predict the distinct property of overwash is the formation of bores as the plates edges dip into the water.

3. When a bore is developed at the upstream edge of the plate only, the model gives favourable qualitative and quantitative agreement with experiments. This regime of agreement corresponds to incident waves of relatively low steepnesses or wavelengths.

4. When a bore is developed at the upstream and downstream edges of the plate, the simplified model significantly overpredicts the amount of overwash on the plate. This

regime of disagreement corresponds to incident waves of relatively large steepnesses or wavelengths.

5. The breakdown of the overwash prediction model can be attributed to the invalidity of the shallow-water assumption when the bore formed from the upstream edge collides with the bore formed on the downstream edge.

The ability of the floating elastic plate model to give favourable agreement with experiments was better understood when comparing the simplified overwash of a step model to the CFD simulation. These comparisons found that:

1. The depth and depth averaged velocity of the overwash in the mathematical model agrees favourably with the CFD model that does not include the effects of a boundary layer at distances $\geq 0.1\,\mathrm{m}$ along the step.

2. At the edge of the step the mathematical model predicts markedly different overwash depths and depth averaged velocities because it does not include wave breaking around the edge.

3. The mathematical model predicts similar mass and energy fluxes in the overwash at the very edge of the step when compared to the CFD models with and without boundary layer effects.

4. The mass and energy fluxes of the overwash in the mathematical model would also agree well with the CFD model without a boundary layer as bores propagated farther along the step. The CFD model with a boundary layer would have a much greater reduction in energy flux due to viscous effects in the boundary layer.

5. In the CFD models with and without boundary layer effects, the transition to a shallow-water flow was small relative to the length of the incident waves and the characteristic length of the bores. Once the flow transitioned to shallow-water flow bores would form. In conjunction with the agreement of mass and energy fluxes at the edge of the step, this was the reason the mathematical model agreed with the no-boundary layer CFD model in terms of depth and depth averaged velocities along the step, but not near to the step's edge. This also indicates why favourable

agreement was found in the floating elastic plate model, despite it neglecting wave breaking around the plate's edges.

The waves reflected/transmitted by the overwashed body were then analysed in the second phase of this investigation (chapters 4 and 5). The CFD model's reflected waves were found to be invariant of whether the boundary layer in the overwash was or was not modelled. It was also found that the overwash would significantly reduce the amplitude of the waves reflected by the step when compared to the theoretical model that did not incorporate the effect overwash had on the waves. In contrast, the floating elastic plate experiments found that the waves reflected by the plate were relatively invariant of overwash. However, when overwash occurred, the waves transmitted past the plate were of significantly lower steepness than that predicted by linear potential flow theory.

Four theoretical models for calculating the modification of the wave fields due to overwash were considered. These models were based on conservation of mass, momentum, and energy principles. The unifying assumption of all of these models was that the mass, momentum, and energy flux into the overwash could be predicted accurately using the models outlined in the first phase of investigation. This assumption was made to circumvent the need for a complicated dynamic coupling condition between overwash and the surrounding waves, and because the first phase of this investigation indicated this assumption was fair. It was found that the model based on mass conservation could not predict the wave field because the time averaged mass flux of linear water waves is small relative to its instantaneous mass flux. It was found that the model based on momentum conservation was unable to predict the wave field because the water around the very edge of step does not follow linear potential theory. It was also found that the model that used energy conservation, but assumed that no energy was dissipated as overwash formed, significantly overpredicted the the size of the surrounding wave field — implying that wave energy is dissipated by the formation of overwash.

These insights were used to develop an energy conservation model that included the energy dissipated by the formation of overwash. This energy dissipation was approximated by assuming the transition from deep water waves to shallow-water flow was sufficiently small such that the transition could be modelled as an instantaneous and discontinuous change in flow parameters. This model was found to give favourable agreement with the

CFD model of an overwashed step in terms of the amplitude of the waves reflected by the overwashed step. It was also found to give favourable agreement to experiments of a floating elastic plate in terms of transmitted wave free surface signals, transmitted wave steepness, and transmitted wave energy. Its main limitation was that it could not account for the irregularity in the waves transmitted by the plate or reflected by the step.

The models presented throughout this thesis have met the objective of this investigation — they can predict overwash and the modification it makes to the surrounding waves within the framework of linear water wave theory. Nonetheless, further improvements to the models presented throughout this investigation can be made. The biggest improvement for the overwash on a floating plate model could be made by better modelling of bores collisions. These collisions are not modelled well under the shallow-water assumption and would likely require a different set of equations to model the overwashed water. The CFD model also indicated that the model for the overwash could be improved by modelling the effects of viscosity and wave breaking, which would better predict the overwash at the step's edge and boundary layer effects. The waves reflected by the step and transmitted by the plate could be predicted more accurately if the spread of these waves across the frequency spectrum was investigated further. This could potentially be done by using the same energy conservation equations, but without time averaging over the incident wave's period. In all these models, it is also likely that the prediction of overwash and surrounding waves would be improved by using a more sophisticated, dynamic, coupling condition between linear potential theory and shallow-water equations. Such a coupling condition was not investigated in this research because of the inherent differences in deep water and shallow-water flow. It would almost certainly require a different approach to the overwash problem.

The models presented can be readily applied to the wave-tank scale. They have been shown to be valid when the overwash is $< 10\,\text{mm}$, the Reynolds number ranges from zero to ~ 3000, the wave steepness is less than 0.15, and, in the context of the floating elastic plate problem, when the incident wave's wavelength is of the same order of magnitude as the plate's length. While the parameters of these models can be changed to model floes in ocean waves (the broader context of this work), extra considerations will need to be taken before this is done. The primary issue is scaling. The experiments in this thesis

have used plates with a characteristic length of 1 m. In contrast, the characteristic length of sea ice can range from tens of metres to kilometres depending on the season and location within the MIZ (Squire & Moore, 1980). The wavelength to plate length ratio and incident wave steepness scales naturally with the characteristic length. However, as the characteristic scale increases so too does the overwash depth and velocity. Hence, if the length of the plate increases tenfold, a first order approximation for an equivalent incident wavelength and steepness would also increase the velocity and depth of the overwash by tenfold. This would increase the Reynolds number by a multiple of ~ 100; resulting in more pronounced turbulence effects that are not included in the shallow-water model. In turn, this implies that additional energy losses will be found in the overwash than those found in this investigation, potentially resulting in greater disagreement between the bores in the theoretical model and full scale experiments. This may also cause stronger disagreement between the theoretical models and experiments with respect to the waves reflected/transmitted by the overwashed body (although this may not be the case given the theoretical model assumes that all energy entering the overwash is lost from the surrounding reflected/transmitted waves). A better understanding of how an increased Reynolds number affects this interaction requires experimentation at larger characteristic length scale than those used in this investigation. Scaling also has the potential to change wave breaking behaviour around the edge of the plate (or step). These effects are particularly likely to change for waves above the steepness range of this investigation ($0 < ka < 0.15$). They could potentially alter the good predictions the theoretical models make regarding the energy of the water entering the overwash as steeper waves increase the wave breaking and separation effects at the body's edges. A better understanding of the models applicability to steeper waves will require additional validation data at larger incident wave steepnesses. A useful step moving forwards would therefore be to conduct wave-tank experiments with much longer floating elastic plates and compare the model to those results. The other natural progressions of this work would be to consider the fully three dimensional problem, irregular wave conditions, experiments on actual ice, and varied plate geometries; all of which are more appropriate for real-world sea ice conditions.

Appendix A

Green's function method for a floating elastic plate

The method presented here follows Newman (1994). The velocity potential of the water is decomposed into a diffracted, ϕ_d and radiated, ϕ_r^n components. The diffracted potential corresponds to the solution when the floating plate is held at rest. The radiated components are set to match the solution corresponding to each mode of vibration of the plate when multiplied by the modal coefficients (i.e. the eigenvalues). The potential is therefore given by $\tilde{\phi} = \phi_d + \sum_{n=0}^{\infty} \zeta_n \phi_r^n$. These components satisfy equations 2.2 with the additional boundary conditions

$$\partial_z \phi_d - \alpha \phi_d = 0 \quad \text{and} \quad \partial_z \phi_r^n = \mathrm{i}\omega \xi_n \tag{A.1}$$

on $z = 0$ and $|x| \leq L$ for all n. They are also required to satisfy the Sommerfeld radiation condition, equation 2.6, for $\bullet = \phi_d - \phi_I$ as $x \to \pm\infty$ and for $\bullet = \phi_r^n$ as $x \to \pm\infty$.

This method requires the use of the free surface Green's function, $G(x, z)$. This function satisfies equations 2.2a and 2.2b, for $\phi = G$, equation 2.6 for $\bullet = G$ as $x \pm \infty$, and the free surface condition with a singularity at $x = x_0$,

$$\partial_z G - \alpha G = \delta(x - x_0) \quad \text{on} \quad z = 0, \tag{A.2}$$

where δ is the Dirac delta function (i.e. $\delta(n) = 1$ if $n = 0$ and 0 otherwise). It can be shown (via separation of variables or complex integration) that free surface Green's

function is therefore given as

$$G = \sum_{n=0}^{\infty} \frac{-\mathrm{i}\mathrm{e}^{-\mathrm{i}|x-x_0|k_n}}{\tanh(k_n h) + k_n h \mathrm{sech}^2(k_n h)} \psi_n(z). \tag{A.3}$$

The potentials are solved by invoking Green's second identity

$$\int_{\partial\Upsilon} I\partial_n G - G\partial_n I \,\mathrm{d}S = \int_{\Upsilon} I\nabla^2 G - G\nabla^2 I \,\mathrm{d}V \tag{A.4}$$

where Υ is an arbitrary domain, $\partial\Upsilon$ is the boundary of this domain, and $\partial_n\bullet$ is the directional derivative operator on the boundary of the domain in the outward normal direction.

Invoking equation A.4 by setting $I = \phi_d - \phi_I$ and Υ to the domain $-H < z < 0$ and $|x| < \infty$ gives

$$\phi_d(x,0) = \phi_I(x,0) - \int_{-L}^{L} \alpha G(x_0,0)\phi_d(x_0,0)\,\mathrm{d}x_0, \tag{A.5}$$

and using $I = \phi_r^n$ for the same Υ

$$\phi_r^n(x,0) = -\int_{-L}^{L} G(x_0,0)\left(\alpha\phi_R^n(x,0) - \mathrm{i}\omega\xi_n\right)\,\mathrm{d}x_0 \tag{A.6}$$

By taking the inner product of equation 2.19, with respect to ξ_n, and using the diffracted and radiated potentials, this gives

$$\left(D\mu_n^4 - \gamma\omega^2 + g\rho_w\right)\zeta_n + \mathrm{i}\omega\sum_{m=0}^{\infty}\zeta_m\rho_w\int_{-L}^{L}\phi_r^m(x,0)\xi_n\,\mathrm{d}x = -\mathrm{i}\omega\rho_w\int_{-L}^{L}\phi_d(x,0)\xi_n\,\mathrm{d}x, \tag{A.7}$$

which is solved as a matrix system (using Simpson's rule to approximate the integral terms) to give all ζ_n for $n = 0, 1, \ldots, m$, up to a sufficiently large m.

The reflected potentials amplitudes are calculating by invoking equation A.4 for Υ given by $-H < z < 0$ and $|x| > L$, $I = \phi$, and $G = \mathrm{e}^{-\mathrm{i}k_n x}$, which gives

$$R_n = \frac{\mathrm{i}}{\tanh(Hk_n) + Hk_n\mathrm{sech}^2(Hk_n)}\int_{-L}^{L}\mathrm{e}^{-\mathrm{i}k_n x}\left(\alpha\phi\left(x,0\right) - \mathrm{i}\omega\xi\right)\,\mathrm{d}x, \tag{A.8}$$

for $n = 0, 1, \ldots, m$, up to a sufficiently large m. The transmitted potential amplitudes are calculated under the same conditions but using $G = \mathrm{e}^{\mathrm{i}k_n x}$, which gives

$$T_n = A\delta(n) + \frac{\mathrm{i}}{\tanh(Hk_n) + Hk_n\mathrm{sech}^2(Hk_n)}\int_{-L}^{L}\mathrm{e}^{\mathrm{i}k_n x}\left(\alpha\phi\left(x,0\right) - \mathrm{i}\omega\xi\right)\,\mathrm{d}x \tag{A.9}$$

for $n = 0, 1, \ldots, m$, up to a sufficiently large m.

Appendix B

Shallow water equations finite volume numerical method

This scheme is the direct application of the finite volume method of Kurganov & Tadmor (2000) as applied to the nonlinear shallow-water equations, and, hence, physical insights into the various steps are not discussed. For this scheme it is convenient to rewrite the nonlinear shallow-water equations in the conservative matrix form

$$\partial_t \mathbf{q} + \partial_x \mathbf{q} = 0, \qquad \text{where} \tag{B.1}$$

$$\mathbf{q} = [h, h\hat{u}]^T, \qquad \text{and} \qquad \mathbf{f}(\mathbf{q}) = \left[h\hat{u}, \frac{1}{2}gh^2 + h\hat{u}^2\right]^T. \tag{B.2}$$

The water on the surface of the plate is discretised into M uniformly spaced volumes of width Δx from along the domain. Using the notation $\mathbf{q}_j(t) = \mathbf{q}(x_j, t)$, where x_j is the centre point of the jth volume along the discretisation, the flux between volumes is given as

$$\partial_x \mathbf{f}(\mathbf{q}_j(t)) \approx -\mathcal{L}\left(\mathbf{q}_j(t)\right) = \frac{\mathbf{B}_{j+\frac{1}{2}}(t) - \mathbf{B}_{j-\frac{1}{2}}(t)}{\Delta x}, \tag{B.3}$$

where $\mathbf{B}_{j-\frac{1}{2}}$ and $\mathbf{B}_{j-\frac{1}{2}}$ are the fluxes to the left and right of the jth volume, respectively. These fluxes are given via the scheme as

$$\mathbf{B}_{j+\frac{1}{2}}(t) = \frac{a^+_{j+\frac{1}{2}} f(\mathbf{q}^-_{j+\frac{1}{2}}) - a^-_{j+\frac{1}{2}} f(\mathbf{q}^+_{j+\frac{1}{2}}) + a^+_{j+\frac{1}{2}} a^-_{j+\frac{1}{2}} \left(\mathbf{q}^+_{j+\frac{1}{2}} - \mathbf{q}^-_{j+\frac{1}{2}}\right)}{a^+_{j+\frac{1}{2}} - a^-_{j+\frac{1}{2}}}, \tag{B.4}$$

$$\text{where} \quad a^{\pm}_{j+\frac{1}{2}} = \pm \max\left\{\pm\kappa_{\pm}(\mathbf{q}^{-}_{j+\frac{1}{2}}), \pm\kappa_{\pm}(\mathbf{q}^{+}_{j+\frac{1}{2}}), 0\right\}, \quad \kappa_{\pm}(\mathbf{q}) = \overline{u} \pm \sqrt{gd}, \quad \text{and} \quad \text{(B.5)}$$

κ_+ and κ_- are the largest and smallest eigenvalues of the Jacobian of $\mathbf{f}(\mathbf{q})$, respectively.

The minmod flux limiter is used to prevent unphysical oscillations caused by the discretisation of the derivative between volumes over a shock. In particular, it prevents unphysical unbounded oscillations forming over time steps. It is defined as

$$\text{minmod}\left\{\bullet_1, \bullet_2, \dots\right\} = \begin{cases} \min_j\{\bullet_j\} & \text{if } \bullet_j > 0 \quad \text{for all } j, \\ \max_j\{\bullet_j\} & \text{if } \bullet_j < 0 \quad \text{for all } j, \end{cases} \tag{B.6}$$

and zero otherwise. The derivative between volumes is discretised as

$$\mathbf{q}_{x,j+\frac{1}{2}} = \text{minmod}\left\{\theta\frac{\mathbf{q}_{j+1} - \mathbf{q}_j}{\Delta x}, \frac{\mathbf{q}_{j+1} - \mathbf{q}_{j-1}}{2\Delta x}, \theta\frac{\mathbf{q}_j - \mathbf{q}_{j-1}}{\Delta x}\right\} \tag{B.7}$$

for $1 \leq \theta \leq 2$ depending on how much dampening around discontinuities is required. In this thesis $\theta = 1$ was used in all applications in order to maximize the dampening of the unnatural oscillations.

The value of $\mathbf{q}^{\pm}$ at the jth volume's right edges is given as

$$\mathbf{q}^{+}_{j+\frac{1}{2}} = \mathbf{q}_{j+1} - \frac{1}{2}\mathbf{q}_{x,j+\frac{1}{2}} \qquad \text{and} \qquad \mathbf{q}^{-}_{j+\frac{1}{2}} = \mathbf{q}_j + \frac{1}{2}\mathbf{q}_{x,j+\frac{1}{2}} \tag{B.8}$$

the value at the left edge is given by subtracting 1 from the j subscripts in B.8. Note there are two values at each volume edge as the finite volume method considers the volumes to be discontinuous over their boundaries.

The above equations allows the full discretisation of the spacial derivative in equation (B.1) around each x_j to be calculated in the domain. The time derivative is discretised using the total variation diminishing second-order Runge-Kutta scheme, given as

$$\mathbf{q}_j\left(t + \Delta t\right) = \mathbf{q}_j(t) + \frac{\Delta t}{2}\mathcal{L}(\mathbf{q}_j(t)) + \frac{\Delta t}{2}\mathcal{L}\big(\mathbf{q}_j(t) + \Delta t\mathcal{L}(\mathbf{q}_j(t))\big) \tag{B.9}$$

where $\Delta t > 0$ is a time step satisfying the CFL condition (Gottlieb & Shu, 1998). These discretisations allow a state in the shallow-water equations to be stepped forwards in time.

Appendix C

Plots of mean overwash depth at the plates' centre for PVC plates

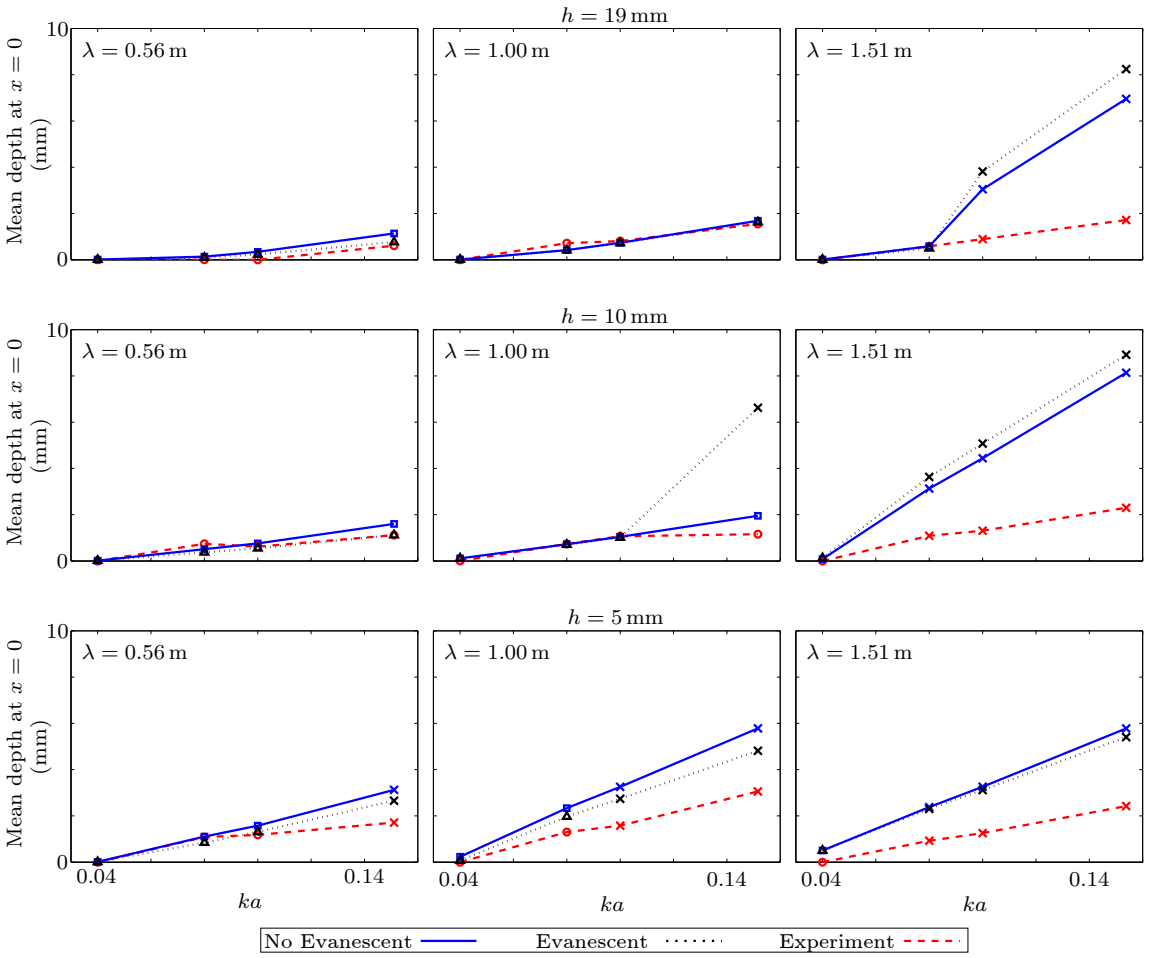

Figure C.1: As in figure 2.7 but for the PVC plates.

Appendix D

Plate edges when bore collision occur

Figure D.1 shows snapshots of the Plymouth experiments for PVC plates of thickness 5 mm and incident waves of period 0.8 s and steepness 0.15. Panel (a) shows the plate at the moment the the front edge dips into the surroding water. When this occurs the water around the edge is shallow, and a bore is travelling towards that edge. Panel (b) shows the moment the water is overturning over the edge, creating a bore there. Although the bore is immediately met with a bore travelling in the opposite direction, it still develops smoothly onto the plate like that shown in figure 2.2 (where bore collisions are not found to occur on the plate). Panels (c) and (d) show the same interaction where the development of the bore on the other edge does not appear to be influenced by the water already on the plate.

Figure D.2 is as in figure D.1 but for a plate of thickness 19 mm and incident waves of period 1.0 s and steepness 0.10. It shows the same qualitative properties as figure D.2 and is presented to demonstrate that this behaviour was found for all plates and waves tested.

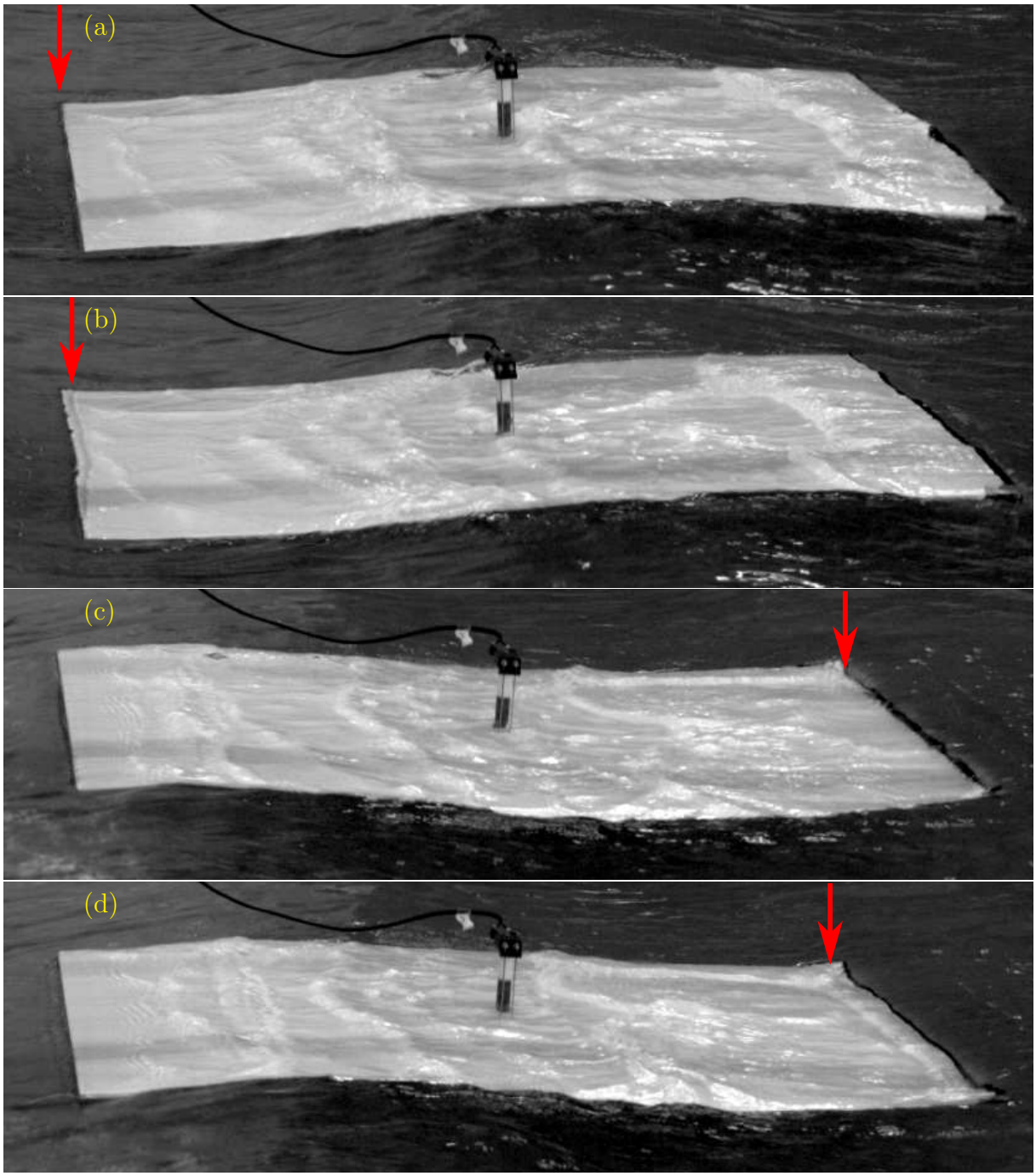

Figure D.1: Snapshots of Plymouth experiments for PVC of thickness 5 mm and incident waves of period 0.8 s and steepness 0.15. (a) shows when the front edge dips into the surrounding water, (b) shows the bore that forms there, (c) shows when the rear edge dips into the surrounding water, and (d) shows the bore that forms there.

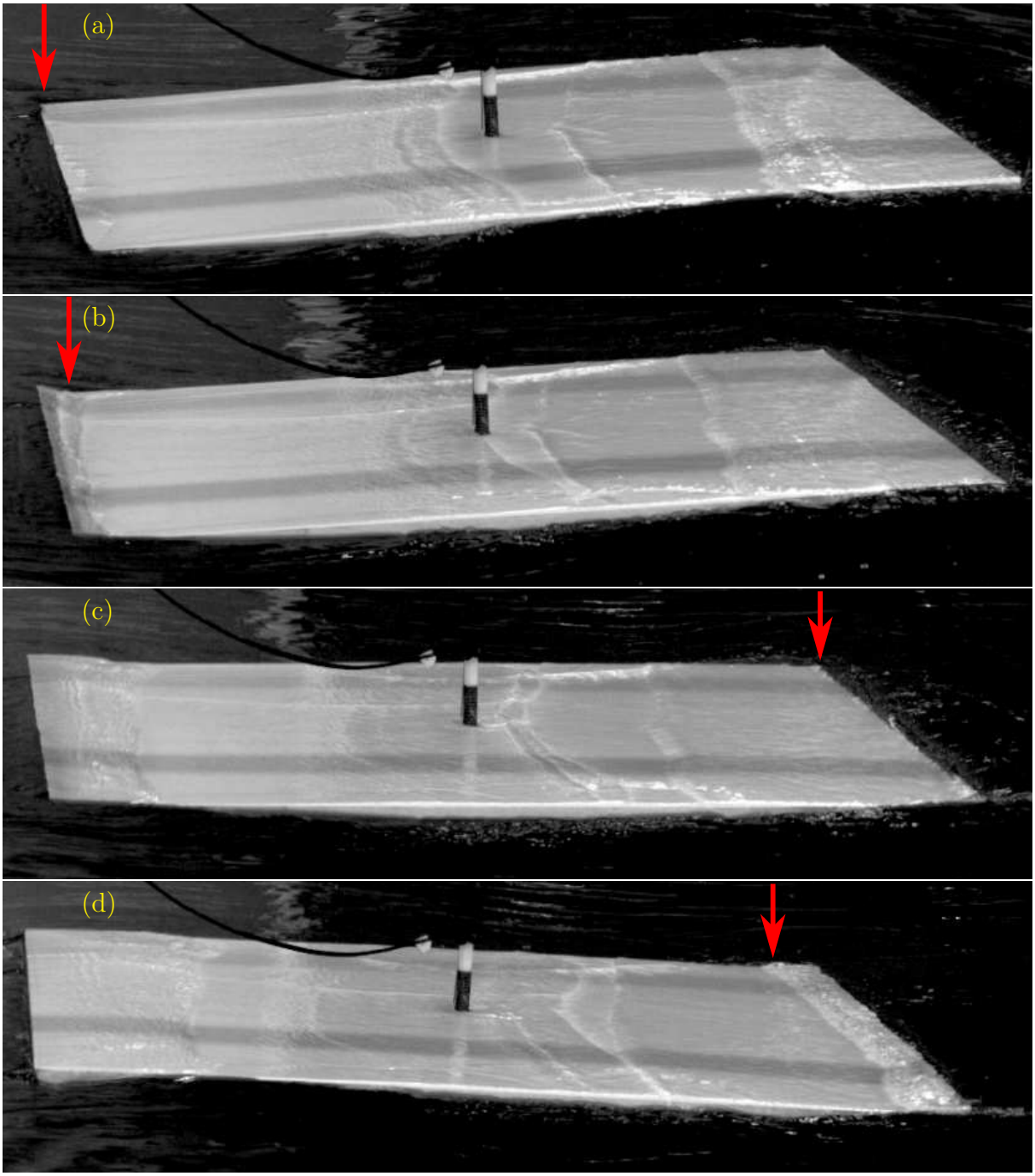

Figure D.2: As in D.1 but for thickness 19 mm, and incident waves with period 1.0 s and steepness 0.10.

Appendix E

Floating elastic plate energy method derivation

Consider the same problem geometry as in figure 2.4 and the control volume C shown in figure E.1. The control volume bounds the water between $x = x_L \ll -L$, $x = x_R \gg L$, the free surface, plate boundaries, and basin bed, but excluding the water between the upper surafce of the plate and $l < x < u$, where $-L < u < L$ and $u < l < L$. In this volume the discontinuities that occur over the interface between deep water waves and shallow-water flow are located at $x = \pm L$ and $z_b(x = \pm L) < z < \eta(x = \pm L)$, respectively. Let Ω_l be the surface aligned with the discontinuity at $x = -L$ and Ω_u be the surface aligned with the discontinuity at $x = L$.

As in section 4.3.4 the heat transfer and internal energy changes are assumed to

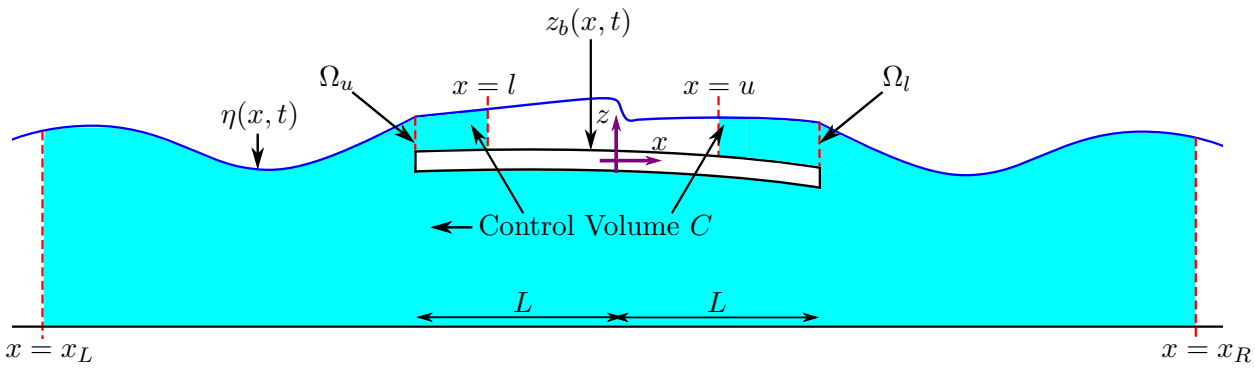

Figure E.1: Schematic of control volumes C (not to scale).

negligible. Therefore, using the notation as in section 4.3.4, $\mathbf{q} = 0$, and

$$E_t = \frac{1}{2}\rho_w(u^2 + w^2) + \rho_w g z, \tag{E.1}$$

which is the energy of the water. Similarly, as in section 4.3.4, assume l and u are sufficiently close to the edges of the plate to neglect the energy losses of the bores, and such that there is a negligible amount of surface area between z_b and the overwash for the plate to educe work via pressure.

Applying of equation 4.22 to C, and including the two discontinuities, instead of the one used in section 4.3.4, gives

$$\begin{aligned}\int_C \frac{\partial}{\partial t} E_t \,\mathrm{d}V + \int_{\partial C \setminus (\Omega_l \cup \Omega_u)} (E_t + p) u_{\mathbf{n}} \,\mathrm{d}S \\ + \int_{\partial \Omega_l} [(E_t + p) u_{\mathbf{n}}]_{-L^-}^{-L^+} \,\mathrm{d}S + \int_{\partial \Omega_u} [(E_t + p) u_{\mathbf{n}}]_{L^-}^{L^+} \,\mathrm{d}S = 0\end{aligned} \tag{E.2}$$

where $\partial C \setminus (\Omega_l \cup \Omega_u)$ is the boundary of C excluding the surfaces Ω_l and Ω_u, and the outwards normal to both Ω_l and Ω_u is in the positive x-direction.

As the energy inside the system is assumed to oscillate periodically with period T, this averages to

$$\overline{\int_{\partial C \setminus (\Omega_l \cup \Omega_u)} (E_t + p) u_{\mathbf{n}} \,\mathrm{d}S} + \overline{\int_{\partial \Omega_l} [E_t + p u_{\mathbf{n}}]_{-L^-}^{-L^+} \,\mathrm{d}S} + \overline{\int_{\partial \Omega_u} [E_t + p u_{\mathbf{n}}]_{L^-}^{L^+} \,\mathrm{d}S} = 0. \tag{E.3}$$

Dividing this equation by ρ_w, multiplying by minus one, and taking $l \to -L^+$ and $u \to L^-$ to ensure that the work done by the pressure at the upper surface of the plate and by the bores reduces to zero, gives

$$\begin{aligned}0 = &+ \overline{\int_{-H}^{\eta} Eu|_{x=x_L} \,\mathrm{d}z} - \overline{\int_{-H}^{\eta} Eu|_{x=x_R} \,\mathrm{d}z} \\ &+ \overline{\int_{z_b}^{\eta^-} Eu|_{x=-L^-} \,\mathrm{d}z} - \overline{\int_{z_b}^{\eta} Eu|_{x=-L^+} \,\mathrm{d}z} + \overline{\int_{z_b}^{\eta} Eu|_{x=L^-} \,\mathrm{d}z} - \overline{\int_{z_b}^{\eta^+} Eu|_{x=L^+} \,\mathrm{d}z} \\ &- \overline{\int_{z_b}^{\eta} Eu|_{-L^+} \,\mathrm{d}z} + \overline{\int_{z_b}^{\eta} Eu|_{L^-} \,\mathrm{d}z},\end{aligned} \tag{E.4}$$

where $\eta^{\pm} = \max\left(\eta(x = \pm L^{\pm}) - z_b(x = \pm L), 0\right)$, and $E\rho_w = E_t - p$.

Finally, to aid interpretation, consider the same problem but without the discontinuities. The same derivation leads to

$$0 = \overline{\int_{-H}^{\eta} Eu|_{x=x_L} \,\mathrm{d}z} - \overline{\int_{-H}^{\eta} Eu|_{x=x_R} \,\mathrm{d}z} - \overline{\int_{z_b}^{\eta} Eu|_{-L^+} \,\mathrm{d}z} + \overline{\int_{z_b}^{\eta} Eu|_{L^-} \,\mathrm{d}z}. \tag{E.5}$$

This implies that the mechanical energy dissipated over the discontinuities (i.e. transition from deep water waves to shallow-water flow) can be quantised as

$$E_{\text{transition}} = -\overline{\int_{z_b}^{\eta^-} Eu|_{x=-L^-}\,\mathrm{d}z} + \overline{\int_{z_b}^{\eta} Eu|_{x=-L^+}\,\mathrm{d}z} - \overline{\int_{z_b}^{\eta} Eu|_{x=L^-}\,\mathrm{d}z} + \overline{\int_{z_b}^{\eta^+} Eu|_{x=L^+}\,\mathrm{d}z}. \tag{E.6}$$

Bibliography

Akan, A. O. 2011 *Open channel hydraulics*. Butterworth-Heinemann.

Babanin, A., Chalikov, D., Young, I. & Savelyev, I. 2007 Predicting the breaking onset of surface water waves. *Geophys. Res. Lett.* **34** (7).

Bai, W., Zhang, T. & McGovern, D. J. 2017 Response of sea ice floes in regular waves: a comparison of numerical and experimental results. *Ocean Eng.* **129** (August 2015), 495–506.

Batchelor, G. K. 2000 *An Introduction to Fluid Dynamics (2nd Ed.)*. Cambridge University Press.

Bennetts, L. G., Alberello, A., Meylan, M. H., Cavaliere, C., Babanin, A. V. & Toffoli, A. 2015 An idealised experimental model of ocean surface wave transmission by an ice floe. *Ocean Model.* **96**, 85–92.

Bennetts, L. G., Peter, M. A., Squire, V. A. & Meylan, M. H. 2010 A three-dimensional model of wave attenuation in the marginal ice zone. *J. Geophys. Res. - Oceans* **115** (C12).

Bennetts, L. G. & Squire, V. A. 2009 Wave scattering by multiple rows of circular ice floes. *J. Fluid Mech.* **639**, 213–238.

Bennetts, L. G. & Squire, V. A. 2012 On the calculation of an attenuation coefficient for transects of ice-covered ocean. *Proc. R. Soc. A* **468**, 136–162.

Bennetts, L. G. & Williams, T. D. 2015 Water wave transmission by an array of floating disks. *Proc. R. Soc. Lond. A* **471** (2014069), http://dx.doi.org/10.1098/rspa.2014.0698.

Berberović, E., van Hinsberg, N. P., Jakirlić, S., Roisman, I. V. & Tropea, C. 2009 Drop impact onto a liquid layer of finite thickness: Dynamics of the cavity evolution. *Phys. Rev. E.* **79** (3), 036306.

Billingham, J. & King, A. C. 2000 *Wave Motion*. Cambridge University Press.

Buchner, B. 1995 The impact of green water on FPSO design. In *Offshore Technology Conference — Houston*, pp. 45–57. http://www.marin.nl/web/Publications/Publication-items/The-Impact-of-Green-Water-on-FPSO-Design.htm.

Buchner, B. 1996 The influence of the bow shape of FPSOs on drift forces and green water. In *Offshore Technology Conference — Houston*, pp. 389–400. http://www.marin.nl/web/Publications/Publication-items/The-Influence-of-the-Bow-Shape-of-FPSOs-on-Drift-Forces-and-Green-Water.htm.

Buchner, B. 2002 Green water on ship-type offshore structures. PhD thesis, Delft University of Technology.

Buchner, B. & Cozijn, J. L. 1997 An investigation into the numerical simulation of green water. In *Proc. Int. Conference on the Behaviour of Offshore Structures — Delft*, pp. 113–125. http://www.marin.nl/web/Publications/Publication-items/An-Investigation-into-the-Numerical-Simulation-of-Green-Water.htm.

Casey, J. 2011 On the derivation of jump conditions in continuum mechanics. *The International Journal of Structural Changes in Solids* **3** (2), 61–84.

Chanson, H. 2004 *Hydraulics of open channel flow*. Butterworth-Heinemann.

Chow, T. V. 1959 *Open channel hydraulics*. McGraw-Hill.

Chung, H. & Fox, C. 2005 Transition conditions at the interface between floating plates. *20th International Workshop on Water Waves and Floating Bodies — Norway* http://www.iwwwfb.org/Abstracts/iwwwfb20/iwwwfb20_07.pdf.

Doble, M. J. & Bidlot, J.-R. 2013 Wavebuoy measurements at the Antarctic sea ice edge compared with an enhanced ECMWF WAM: progress towards global waves-in-ice modeling. *Ocean Model.* **70**, 166–173.

Dumont, D., Kohout, A. L. & Bertino, L. 2011 A wave-based model for the marginal ice zone including a floe breaking parameterization. *J. Geophys. Res.* **116** (C04001).

Evans, D. V. 2004 Mathematical techniques for linear wave-structure intercations. In *19th International Workshop on Water Waves and Floating Bodies — Italy*. `http://www.iwwwfb.org/%5C/Abstracts/iwwwfb19/iwwwfb19_51.pdf`.

Evans, D. V. & Porter, R. 2003 Scattering of flexural-gravity waves by multiple cracks in ice sheets floating on water of finite depth. In *18th International Workshop on Water Waves and Floating Bodies — France*. `http://www.iwwwfb.org/Abstracts/iwwwfb18/iwwwfb18_15.pdf`.

Fox, C. & Squire, V. A. 1994 On the oblique reflexion and transmission of ocean waves at shore fast sea ice. *Phil. Trans. R. Soc. Lond. A.* **347** (1682), 185–218.

Gallavotti, G. 2002 *Foundations of fluid mechanics*. Springer.

Gottlieb, S. & Shu, C. W. 1998 Total variation diminishing Runge-Kutta schemes. *Math. Comp.* **67** (221), 73–85.

Graham, N. E. 1995 Simulation of recent global temperature trends. *Science* **267** (5198), 666.

Greco, M. 2001 A two-dimensional study of green-water loading. PhD thesis, Norwegian University of Science and Technology.

Greco, M, Colicchio, G. & Faltinsen, O. M. 2007 Shipping of water on a two-dimensional structure. Part 2. *J. Fluid Mech.* **581**, 371–399.

Greco, M, Faltinsen, O. M. & Landrini, M. 2005 Shipping of water on a two-dimensional structure. *J. Fluid Mech.* **525**, 309–332.

Grue, J. 1992 Nonlinear water waves at a submerged obstacle or bottom topography. *J. Fluid Mech.* **244**, 455–476.

Hall, M. & Wouters, M. 1994 Managing nature tourism in the Sub-Antarctic. *Ann. Tourism Res.* **21** (2), 355–374.

Hansen, J., Ruedy, R., Sato, M. & Lo, K. 2010 Global surface temperature change. *Rev. Geophys.* **48** (4).

Hirt, C. W. & Nichols, B. D. 1981 Volume of fluid method for the dynamic of free boundaries. *J. Comp. Phys* **39**, 323–345.

Holthuijsen, L. H. 2010 *Waves in oceanic and coastal waters*. Cambridge university press.

Jacobsen, N. G., Fuhrman, D. R. & Fredsøe, J. 2012 A Wave Generation Toolbox for the Open-Source CFD Library: OpenFoam® . *Int. J. Numer. Meth. Fl.* **70** (9), 1073–1088.

Kohout, A. L. & Meylan, M. H. 2006 A model for wave scattering in the marginal ice zone based on a two-dimensional floating-elastic-plate solution. *Ann. Glaciol.* **44** (1), 101–107.

Kohout, A. L., Williams, M. J. M., Dean, S. M. & Meylan, M. H. 2014 Storm-induced sea-ice breakup and the implications for ice extent. *Nature* **509** (7502), 604–607.

Kurganov, A. & Tadmor, E. 2000 New high-resolution central schemes for nonlinear conservation laws and convection–diffusion equations. *J. Comput. Phys.* **160** (1), 241–282.

Lange, M. A., Ackley, S. F., Wadhams, P. & Dieckmann, G. S. 1989 Development of sea ice in the weddell sea. *Ann. Glacio.* **12** (1), 92–96.

Langhorne, P. J., Squire, V. A., Fox, C. & Haskell, T. G. 1998 Break-up of sea ice by ocean waves. *Ann. Glaciol.* **27** (1), 438–442.

Langhorne, P. J., Squire, V. A., Fox, C. & Haskell, T. G. 2001 Lifetime estimation for a land-fast ice sheet subjected to ocean swell. *Ann. Glaciol.* **33** (1), 333–338.

Linton, C. M. & McIver, P. 2001 *Handbook of mathematical techniques for wave/structure interactions*. CRC Press.

Liu, I. S. 2013 *Continuum mechanics*. Springer.

Losada, I. J., Patterson, M. D. & Losada, M. A. 1997 Harmonic generation past a submerged porous step. *Coast Eng.* **31** (1-4), 281–304.

Mansard, E. P. D. & Funke, E. R. 1980 The measurement of incident and reflected spectra using a least squares method. In *17th Int. Conf. on Coast. Eng.*, , vol. 1, pp. 154–172.

Massom, R. A. & Stammerjohn, S. E. 2010 Antarctic sea ice change and variability–physical and ecological implications. *Polar Sci.* **4** (2), 149–186.

McGovern, D. J. & Bai, W. 2014 Experimental study on kinematics of sea ice floes in regular waves. *Cold Reg. Sci. Technol.* **103**, 15–30.

McKenna, R. F. & Crocker, G. B. 1991 *Wave energy and floe collisions in marginal ice zones*. University of Newfoundland.

Mei, C. C., Stiassnie, M. & Dick, K, Y. 1989 *Theory and Applications of Ocean Surface Waves: Part 1: Linear Aspects*. World Scientific.

Meylan, M. & Squire, V. A. 1994 The response of ice floes to ocean waves. *J. Geophys. Res. - Oceans.* **99** (C1), 891–900.

Meylan, M. H. 2003 Wave scattering in the marginal ice zone. In *18th International Workshop on Water Waves and Floating Bodies — France*. `http://www.iwwwfb.org/%5C/Abstracts/iwwwfb18/iwwwfb18_35.pdf`.

Meylan, M. H., Bennetts, L. G., Cavaliere, C., Alberello, A. & Toffoli, A. 2015 Experimental and theoretical models of wave-induced flexure of a sea ice floe. *Phys. Fluids* **27** (4), 041704.

Meylan, M. H., Bennetts, L. G. & Kohout, A. L. 2014 In situ measurements and analysis of ocean waves in the antarctic marginal ice zone. *Geophys. Res. Lett.* **41** (14), 5046–5051.

Meylan, M. H., Squire, V. A. & Fox, C. 1997 Toward realism in modeling ocean wave behavior in marginal ice zones. *J. Geophys. Res. - Oceans* **102** (C10), 22981–22991.

Mills, A. F. 1999 *Heat Transfer (2nd Ed.)*. Prentice Hall.

Mizoguchi, S. 1988 Analysis of shipping water with the experiments and the numerical calculations. *J. Soc. Nat. Nav. Archit. Jpn.* **27**, 83–91.

Montiel, F., Bennetts, L. G., Squire, V. A., Bonnefoy, F. & Ferrant, P. 2013*a* Hydroelastic response of floating elastic discs to regular waves. Part 2. Modal analysis. *J. Fluid Mech.* **723**, 629–652.

Montiel, F., Bonnefoy, F., Ferrant, P., Bennetts, L. G., Squire, V. A. & Marsault, P. 2013*b* Hydroelastic response of floating elastic discs to regular waves. Part 1. Wave basin experiments. *J. Fluid Mech.* **723**, 604–628.

Montiel, F., Squire, V. A. & Bennetts, L. G. 2016 Attenuation and directional spreading of ocean wave spectra in the marginal ice zone. *J. Fluid Mech.* **790**, 492–522.

Moran, M. J., Shapiro, Howard N., Boettner, D. D. & Bailey, M. B. 2010 *Fundamentals of engineering thermodynamics*. Wiley.

Nelli, F., Bennetts, L. G., Skene, D. M., Monty, J. P., Lee, J. H., Meylan, M. H. & Toffoli, A. 2017 Reflection and transmission of regular water waves by a thin, floating plate. *Wave Motion* **70**, 209–221.

Newman, J. N. 1994 Wave effects on deformable bodies. *Appl. Ocean Res.* **16** (1), 47–59.

Nielsen, K. B. & Mayer, S. 2004 Numerical prediction of green water incidents. *Ocean Eng.* **31** (3), 363–399.

Orszaghova, J., Borthwick, A. G. L. & Taylor, P. H. 2012 From the paddle to the beach–a boussinesq shallow water numerical wave tank based on madsen and sørensens equations. *J. Comp. Phys.* **231** (2), 328–344.

Parkinson, C. L. & DiGirolamo, N. E. 2016 New visualizations highlight new information on the contrasting Arctic and Antarctic sea-ice trends since the late 1970s. *Remote Sens. Environ.* **183**, 198–204.

Paulsen, Bo. T., Bredmose, H., Bingham, H. B. & Jacobsen, N. G. 2014 Forcing of a bottom-mounted circular cylinder by steep regular water waves at finite depth. *J. Fluid. Mech.* **755**, 1–34.

Schlichting, H. & Gersten, K. 2016 *Boundary-Layer Theory (9th Ed.)*. Springer.

Shen, H. H. & Squire, V. A. 1998 Wave damping in compact pancake ice fields due to interactions between pancakes. In *Antarctic Sea Ice: Physical Processes, Interactions and Variability*. Wiley.

Skene, D. M., Bennetts, L. G., Meylan, M. H. & Toffoli, A. 2015 Modelling water wave overwash of a thin floating plate. *J. Fluid Mech.* **777**, R3.

Skene, D. M., Bennetts, L. G., Wright, M., Meylan, M. H. & Maki, K. J. 2018 Water wave overwash of a step. *J. Fluid Mech.* **839**, 293–312.

Squire, V. A. 2007 Of ocean waves and sea-ice revisited. *Cold Reg. Sci. Technol.* **49** (2), 110–133.

Squire, V. A., Dugan, J. P., Wadhams, P., Rottier, P. J. & Liu, A. K. 1995 Of ocean waves and sea ice. *Annu. Rev. Fluid Mech.* **27** (1), 115–168.

Squire, V. A. & Moore, S. C. 1980 Direct measurement of the attenuation of ocean waves by pack ice. *Nature* **283** (5745), 365–368.

Tan, Wei-Yan 1992 *Shallow water hydrodynamics: Mathematical theory and numerical solution for a two-dimensional system of shallow-water equations*. Elsevier.

Thomson, R. E. & Emery, W. J. 2014 *Data analysis methods in physical oceanography*. Newnes.

Timco, G. W. & Weeks, W. F. 2010 A review of the engineering properties of sea ice. *Cold Reg. Sci. Technol.* **60** (2), 107–129.

Timoshenko, S. P. & Woinowsky-Krieger, S. 1959 *Theory of plates and shells*. McGraw-hill.

Tin, T., Liggett, D., M., Patrick T. & Lamers, M. 2013 *Antarctic futures: human engagement with the Antarctic environment*. Springer.

Vreugdenhil, C. B. 1994 *Numerical Methods for Shallow-Water Flow*. Kluwer Academic.

Wadhams, P. 1973*a* Attenuation of swell by sea ice. *J. Geophys. Res.* **78** (18), 3552–3563.

Wadhams, P. 1973*b* The effect of a sea ice cover on ocean surface waves. PhD thesis, Scott Polar Research Institute, University of Cambridge.

Wadhams, P. 1986 The seasonal ice zone. In *The Geophysics of Sea Ice*, pp. 825–991. Springer.

Wadhams, P., Lange, M. A. & Ackley, S. F. 1987 The ice thickness distribution across the atlantic sector of the antarctic ocean in midwinter. *J. Geophys. Res. - Oceans.* **92** (C13), 14535–14552.

Wadhams, P., Squire, V. A., Ewing, J. A. & Pascal, R. W. 1986 The effect of the marginal ice zone on the directional wave spectrum of the ocean. *J. Phys. Oceanogr.* **16** (2), 358–376.

Wadhams, P., Squire, V. A., Goodman, D. J., Cowan, A. M. & Moore, S. C. 1988 The attenuation rates of ocean waves in the marginal ice zone. *J. Geophys. Res.* **93** (C6), 6799–6818.

Weller, H. G., Tabor, G., Jasak, H. & Fureby, C. 1998 A tensorial approach to computational continuum mechanics using object-oriented techniques. *Comput. Phys.* **12** (6), 620–631.

Whitham, G. B. 1962 Mass, momentum and energy flux in water waves. *J. Fluid Mech.* **12** (1), 135–147.

Williams, T. D. 2006 The scattering by a sea ice/ice shelf transition. In *21th International Workshop on Water Waves and Floating Bodies — UK*. `http://www.iwwwfb.org/Abstracts/iwwwfb21/iwwwfb21_49.pdf`.

Williams, T. D., Bennetts, L. G., Squire, V. A., Dumont, D. & Bertino, L. 2013*a* Wave–ice interactions in the marginal ice zone. Part 1: Theoretical foundations. *Ocean Model.* **71**, 81–91.

Williams, T. D., Bennetts, L. G., Squire, V. A., Dumont, D. & Bertino, L. 2013*b* Wave–ice interactions in the marginal ice zone. Part 2: Numerical implementation and sensitivity studies along 1D transects of the ocean surface. *Ocean Model.* **71**, 92–101.

Williams, T. D. & Porter, R. 2009 The effect of submergence on the scattering by the interface between two semi-infinite sheets. *J. Fluid Struct.* **25** (5), 777–793.

Yiew, L. J., Bennetts, L. G., Meylan, M. H., French, B. J. & Thomas, G. A. 2016 Hydrodynamic responses of a thin floating disk to regular waves. *Ocean Model.* **97**, 52–64.

Young, I. R., Zieger, S. & Babanin, A. V. 2011 Global trends in wind speed and wave height. *Science* **332** (6028), 451–455.